Model Order Reduction of Rarefied Gases using Neural Networks

Bachelorarbeit

zur Erlangung des akademischen Grades
Bachelor of Science (B. Sc.)
im Fach Physikalische Ingenieurswissenschaften

Technische Universität Berlin
Fakultät Verkehrs- und Maschinensysteme V
Institut für Numerische Fluiddynamik

eingereicht von: *Zachary Schellin*
geboren am: *11.02.1991, Berlin*

Gutachter: *Prof. Dr. Julius Reiss*
Dr. Mathias Lemke

eingereicht am: *01. Juli 2021*

Abstract

Neural networks, in particular autoencoders, in the context of model order reduction (MOR) of rarefied gases are evaluated against state-of-the-art proper orthogonal decomposition (POD). Both methods are examined on the solution of the BGK model in Sod's shock tube for a continuum- and a slightly rarefied gas. Therefore, a convolutional neural network (CNN) as well as a fully connected neural network (FCNN) are designed and the finding of appropriate hyperparameters is discussed. The FCNN surpasses POD only in the number of parameters used to achieve reconstruction losses of 8×10^{-4} and 9×10^{-4} for the two flows by a factor of 5.6 and 6.7 respectively. The CNN fails to reproduce usable results, giving rise to further the exploration chosen hyperparameters. Moreover, the similarity between macroscopic quantities and intrinsic variables extracted from the FCNN demonstrate physical interpretabillity. Beyond that, the generation of new snapshots of solutions of the flow succeeded using the decoder of the FCNN through a temporal interpolation in the intrinsic variables.

Zusammenfassung

Neuronale netzte im speziellen Autoencoder und proper orthogonal decomposition (POD), dem Stand der Technik, werden im Kontext von Modellreduktion einander gegenübergestellt. Beide Methoden werden an Lösungen der BGK-Gleichung in Sods Stoßrohr für eine kontinuierliche- und eine leicht verdünnte Gasströmung untersucht. Hierfür ist ein Convolutional Neural Network (CNN) und ein Fully Connected Neural Network (FCNN) designt und das Auffinden von Hyperparametern diskutiert. Es wird gezeigt, dass das FCNN die POD lediglich in der Anzahl an verwendeten Parametern für Rekonstruktionsfehler von 8×10^{-4} und 9×10^{-4} übertrifft. Das CNN schafft es nicht, brauchbare Ergebnisse zu erzielen. Dies wirft jedoch die Frage nach geeigneteren Hyperparametern auf und motiviert für eine weitere Untersuchung dieser. Auch kann die physikalische Interpretierbarkeit der intrinsischen Variablen anhand der Ähnlichkeit zu Makroskopischen Größen gezeigt werden. Darüber hinaus können mithilfe des Decoders neue Zeitschritte der Lösung durch eine zeitliche Interpolation in den intrinsischen Variablen erzeugt werden.

Contents

1 Introduction

The Bhatnagar-Gross-Krook equation (BGK) is a kinetic collision model for ionized and neutral gases valid in rarefied as well as other pressure regimes [1]. Generating data of such a flow field is essential for various industry and scientific applications[2]. With the intention to reduce time and cost during the data generating process, experiments were substituted with computational fluid dynamics (CFD) simulations. Consequently, reduced-order models (ROMs) coupled to the aforementioned simulations were introduced to further the reduction of time and cost. The thriving field of artificial intelligence successfully operates on natural language processing and object recognition and has now surfaced in fluid mechanics for model order reduction as seen in [3] and [4]. This thesis will attempt to estimate the capability of artificial intelligence for model order reduction for the BGK model in Sod's shock tube. Specifically, the performance of autoencoders in a fully connected and convolutional version is revised using proper orthogonal decomposition (POD) as a benchmark.

Using neural networks i.e. deep learning in the form of autoencoders for reduced-order modeling in CFD is a novel approach. Though, "the idea of autoencoders has been part of the historical landscape of neural networks for decades"[5][p.493]. Autoencoders, or more precisely learning internal representations by the delta rule (backpropagation) and the use of hidden units in a feed-forward neural network architecture, premiered by Rumelhart et al in [6] in 1986. Through, so-called, hierarchical training, Ballard et al. introduce in [7] in 1987 a strategy to train auto auto-associative networks, nowadays referred to as autoencoders, in a reasonable time promoting further development despite computational limitations. The so-called bottleneck of autoencoders often yields a non-smooth and entangled representation thus being uninterpretable by practitioners leading to developments in this field is stated in [8] by Rifai et al. in 2011. They introduce the contractive autoencoder (CAE) for classification tasks intending to extract robust features which are insensitive to input variations orthogonal to the low-dimensional non-linear manifold by adding a penalty on the Frobenius norm of the intrinsic variables with respect to the input, surpassing other classification algorithms. In 2014, Titled "Auto-Encoding Variational Bayes" in [9], Kingma et. al introduce the variational autoencoder with which an intractable posterior density distribution can be approximated. Disentangled latent variables are obtained from which sampling is possible. A similar approach formulated in 2019 in [10] by Tolstikhin et. al enforces as well entangled latent variables during autoencoding. Timeseries forecasting using neural networks experiences a boost when in 1997 Hochreiter et. al introduce the long short-term memory (LSTM) cell that uses an "efficient truncated backprop version"[p.22] in [11] pivotal decreasing training time for recurrent networks. Further developments in 2017 by Vaswani et. al in [12] concerning natural language translation introduce the transformer which eschews convolutions and recurrence, solely relying on global attention mechanisms that are used to completely replace convolutions for image recognition in [13] and through their computational efficacy constitute a small revolution.

Proper orthogonal decomposition (POD) coupled with Galerkin projection methods can be found in numerous tracks towards model order reduction for dynamical systems like shifted POD (sPOD) introduced by Reiss et. al in 2018 in [14] tailored for transport problems and wavelet POD (wPOD) by Krah et. al in [15] tailored for three-dimensional high-resolution data, which limits the applicability of POD, to name only a few of them. Bernard et al. use POD-Galerkin in [16] with an additional population of their snapshot database via optimal transport for the proposed BGK equation and test case, reducing computational runtime by 94% in conjunction with an approximation error of $\sim 1\%$. Artificial intelligence in the form of convolutional autoencoders, replacing POD within a Galerkin framework, is evaluated against the POD performance by Kookjin et al. in [3] for advection-dominated problems resulting in sub-0.1% errors for two experiments using approximately, what they call, the intrinsic solution manifold dimension. An additional temporal interpolation requires to train the autoencoders with fewer samples which are found to be insensitive above 100 examples, for their experiments, along with degradation of accuracy of 20% only after that. Eivazi et. al advance in [17] a step further not only replacing POD by autoencoders but also using an LSTM for the Galerkin projection method to evolve the intrinsic variables in time, which culminates as well in sub-.1% errors. Both contributions mention the computational cost needed for training the neural networks questioning their fit in model order reduction.

The thesis is divided into five sections. Firstly, the BGk model in Sod's sock tube is introduced in chapter 2. Furthermore, dimensionality reduction algorithms used in this thesis, namely proper orthogonal decomposition (POD) and autoencoders, are introduced in chapter 3. Additionally, model order reduction and the integration of POD and autoencoders with emphasis on the so-called offline phase is described in chapter 4. The comparison of both methods by evaluating their reconstruction loss and the interpretability of the so-called reduced variables can be found in chapter 5. In addition, the autoencoders ability to generalize is also tested in this section. A description covering the selection of design features for the convolutional and fully connected autoencoder is available in appendix A and appendix B. The code for this thesis is written in `Python` version 3.8. Both autoencoders are implemented using the open-source machine learning library `pyTorch` version 1.8.1 developed by Facebook's AI Research lab (FAIR) which is available from `www.pytorch.org`. Furthermore, `NumPy`, for any additional computations aside the machine learning aspect, and `pandas`, for data manipulation available through the open-source scientific computing library `SciPy` version 1.6.3 available through `www.scipy.org`, are used.

2 The BGK Model

This chapter discusses the BGK model, a kinetic gas model, in Sod's shock tube. Sod's shock tube serves as a test case for which solutions of the BGK model were made available for this thesis.
The BGK model is valid for a broad range of rarefaction levels. From continuum flows where the Navier-Stokes equations can be utilized, to highly rarefied regimes. Rarefaction levels are labeled with the so-called Knudsen number Kn, first introduced by danish physicist Martin Knudsen [16]. The Knudsen number is given by

$$Kn = \frac{\lambda}{l}, \tag{2.1}$$

where λ is the mean free path of a particle and l some domain specific length. For example the diameter of a tube. The mean free path of a particle is defined as the distance between subsequent collisions. When the mean free path is much smaller than, e.g., the diameter of a tube, then the fluid can be described as a continuum and the Navier-Stokes equations can be used to approximate it's answer to initial conditions. Evidently, in rarefied gases, a particle's chance to collide is much smaller and therefore it travels further between collisions. In those cases, the assumption that the fluid can be viewed as a continuum fails. Figure 2.1, which is taken from [18], shows a possible partitioning of Kn into specific regimes. Though no clear cut can be applied to different values of Kn. The boundaries are particularly blurry [19].

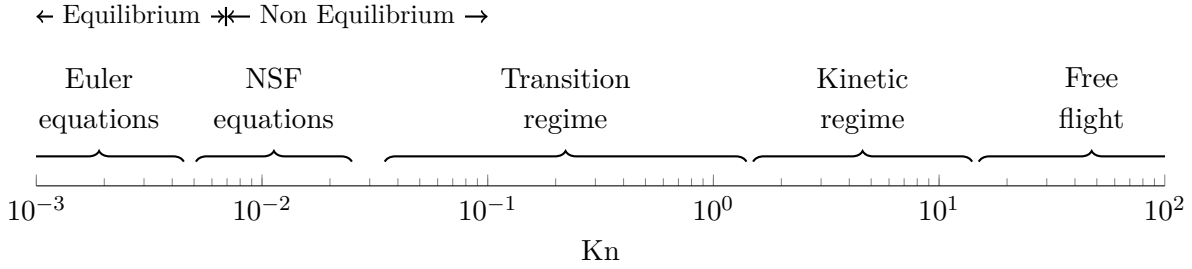

Figure 2.1: Partitioning of Kn, the Knudsen number, into levels of rarefaction. Up to approximately $Kn < 0.01$, the Euler equations can be used and describe a continuum flow. A slip flow can be defined in the interval $0.01 < Kn < 0.1$, termed as slightly rarefied in [19]. Here the Navier-stokes-Fourier equations yield accurate results as stated in [18]. From $Kn > 0.1$ onward (transition regime, kinetic regime, and free flight), the rarefaction increases steadily and only kinetic gas models deliver reasonable results. The BGK model can be applied to all rarefaction levels.

2.1 Space and Velocity Discretization, Moments and Conservation

The BGK model was introduced by, and named after, physicists Prabhu L. Bhatnagar, Eugene P. Gross and Max Krook in 1954 [1]. It is an approximation of the standard Boltzmann transport

equation. More precisely, the right-hand side of the Boltzmann equation is approximated by the BGK operator

$$\partial_t f + v\partial_x f = \frac{1}{\tau}(M_f - f), \tag{2.2}$$

which can be found in [20]. It features the relaxation time $\tau(x,t)$, the Maxwellian distribution M_f and $f(t,v,x)$ the probability of a gas particle having a microscopic velocity v in phase space (t,v,x). It is a source term describing the distance between the current probability density function f and it's equilibrium solution M_f. Evidently, when $f = M_f$ the right-hand side becomes zero and equilibrium is reached. A time scale for which f transitions into equilibrium is given by τ and can be defined with

$$\tau^{-1} = \frac{\rho(x,t)T^{1-\nu}(x,t)}{Kn}, \tag{2.3}$$

which is taken from [16]. Through τ, the viscosity exponent ν, density $\rho(x,t)$, temperature $T(x,t)$ and Knudsen number Kn additionally establish a scaling factor for the right-hand side of the BGK model. The Maxwellian distribution M_f is defined by

$$M_f = \frac{\rho(x,t)}{(2\pi RT(x,t))^{\frac{3}{2}}} \exp(-\frac{(v-u(x,t))^2}{2RT(x,t)}), \tag{2.4}$$

with $u(x,t)$ the macroscopic velocity and R the universal gas constant. The left-hand side of the BGK model is the Boltzmann transport equation for $f(t,v,x)$. In one dimension, the BGK model needs to be evaluated for the three independent variables x, v and t as seen above. Furthermore, in three dimensions, one needs to include the evaluation at (x,y,z) in space and (v_x,v_y,v_z) in velocity space. Note that in this thesis, the BGK model is discussed in one dimension only.
The fruitfullness of performing a model order reduction on the BGK model becomes clearer when looking at it's space and velocity discretization

$$\partial_t f_{j,k} = -(v_k)_1 D_x f|_{j,k}(t) + \frac{1}{\tau}(M_{f\,j,k}(t) - f_{j,k}(t)), \tag{2.5}$$

as seen in [20]. Here a uniform grid is considered with $x_j = j\Delta x$, $j \in \mathbb{Z}$, $v_k = k\Delta v$, $k \in \mathbb{Z}$ and $t^i = i\Delta t$, $i \in \mathbb{N}$ on which $f_{j,k} = f(t,v_k,x_j)$ and $M_{f\,j,k} = M_f(x_j,v_k,t)$ are evaluated at point (x_j,v_k) in a time instance t. For brevity $D_x f|_{j,k}$ is the discrete space derivative at (x_j,v_k). Now the partial differential equation (PDE) in eq. (2.2) is broken down into a system of ordinary differential equations (ODE's) in time, for which every ODE is a linear advection equation with constant scalar speed v_k and a source term.

When considering K to be the number of gridpoints in velocity, and J to be the number of grid points in space, then a total of KJ first-order differential equations need to be evaluated in 1D. Evidently, in three dimensions, the system of ODEs inflates up to K^3J^3 first-order differential equations. This in turn drives the evaluation of the BGK model at the edge of intractability for dense meshes in 3D and all together motivate for a reduced order model.
The discretization in velocity space yields the necessity to compute the moments of f and provides a system of conservative equations. Moments or expected values of f are the density ρ, the momentum ρu and the energy E, which can be obtained with

$$\rho(x,t) = \int f \,\mathrm{d}v\,, \tag{2.6}$$
$$\rho(x,t)u(x,t) = \int vf \,\mathrm{d}v \tag{2.7}$$
and
$$E(x,t) = \int \frac{1}{2}v^2 f \,\mathrm{d}v\,, \tag{2.8}$$

as shown in [20]. Additionally, the temperature T and the pressure p can be obtained with

$$T = \frac{2E}{3\rho} - \frac{||u||^2}{3} \qquad (2.9) \qquad \text{and} \quad p = \rho T\,. \qquad (2.10)$$

Thus multiplying $\Phi(v) = [1, v, \frac{1}{2}v^2]$, called the collision invariants, with f and integrating in velocity space, one obtains the moments of f, which are needed to compute the maxwellian in eq. (2.5). Again, the system in eq. (2.2) is in equilibrium when $f = M_f$. Multiplying the equilibrium solution (left-hand side of eq. (2.2), substituting $f = M_f$) with $\Phi(v)$ and integrating in velocity space, one finds the Euler system of classical gas dynamics. Required is the equation of state of the gas as in [20]. These are

$$\partial_t \rho + \partial_x(\rho u) = 0\,, \qquad (2.11)$$

$$\partial_t(\rho u) + \partial_x(\rho u^2 + p) = 0\,, \qquad (2.12)$$

$$\partial_t E + \partial_x(u(E + p)) = 0\,, \qquad (2.13)$$

and provide conservation laws for the BGK model. Note that the evaluation of the maxwellianM_f is not straight forward and requires three additional non-linear equations for every K-th grid point in velocity space. This is due to the fact, that for M_f the moments in eq. (2.6), eq. (2.7) and eq. (2.8) are required. The quadrature rule used to compute the moments requires to be exact because even small errors magnify when $\tau \to 0$ and in turn one fails to obtain the Euler equations. Therefore M_f must satisfy

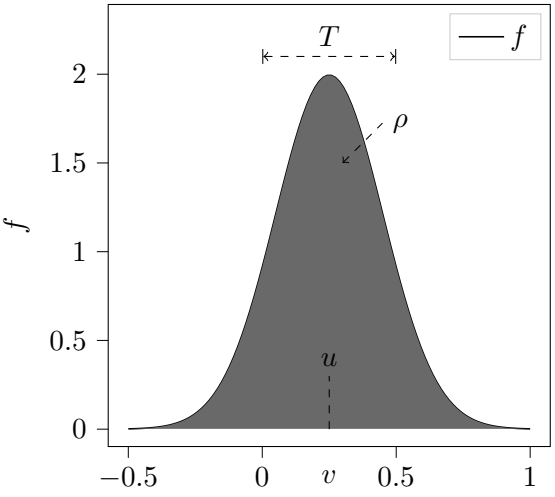

Figure 2.2: Illustration of the linkage between the macroscopic quantities of the gas flow and the distribution function f.

$$< \Phi(v) f > - < \Phi(v) M_f >= 0\,, \qquad (2.14)$$

which is accomplished by the computation of a discrete Maxwellian $\mathcal{M}_f$ by solving

$$\sum_k w_k \Phi(v_k)[f(t, v_k, x) - \exp(\alpha(x, t)\Phi(v_k))] = 0\,. \qquad (2.15)$$

Here w_k are weights and $\alpha(x, t)$ is a vector of three elements from which a unique solution can be found for $\mathcal{M}_f$. Further insights on $\mathcal{M}_f$ and the temporal discretization are provided in [20].

Displayed in fig. 2.2 is a demonstrative example of how the distribution function $f(v)$ gives the values for the macroscopic quantities. The distribution is centered around the macroscopic velocity u, the mean velocity of the distribution f is the temperature T, integrating $f(v)$ over velocity space one obtains the density ρ.

The BGK model inherits global conservation of mass, momentum and energy from the Boltzmann equation, as seen in eq. (2.11), eq. (2.12) and eq. (2.13) found in [20].

2.2 Sod's shock tube as a test case for the BGK model

Using a shock tube as a test case for numerical schemes solving non-linear hyperbolic conservation laws in gas dynamics was studied by Sod (1978) [21]. Sod evaluated the performance of capturing the rarefaction wave, the contact discontinuity, and the shock wave, which develop in the shock tube for different numerical schemes. Since then it serves as a commonly used benchmark problem in numerical gas dynamics.
Non-linear conservation laws in a simple shock tube can be solved analytically and thereafter be compared to the numerical approximation. The analytical solution is obtained using the method of characteristics and the Rankine Hugoniot jump conditions to connect the states before and after the shock. Details about both methods can be found in [22].

The problem setup for a shock tube at $t = 0$ is shown in fig. 2.3 and fig. 2.4a, which is split into two regions (region 1 and region 5) via a diaphragm. Here the initial conditions for two fluids at rest are $\rho_0 = 1$ and $\rho_5 = 0.125$ for the density, $p_0 = 1$ and $p_5 = 0.1$ for the pressure and $u_0 = u_5 = 0$ for the macroscopic velocity [21].

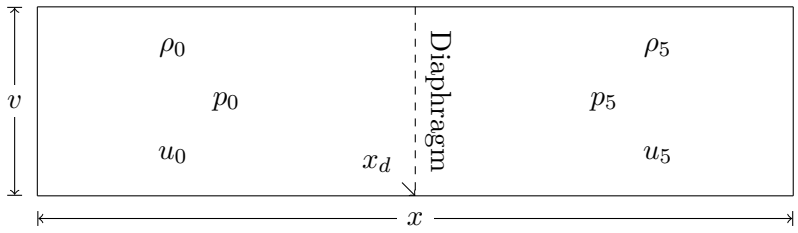

Figure 2.3: Problem setup for Sod's shock tube in 1D translated for the BGK model in velocity v and space x. A diaphragm is positioned at x_d, seperating the whole domain in two regions (region 1 and region 5). Initial conditions for density ρ, pressure p and macroscopic velocity u are indicated.

At $t > 0$ the diaphragm is broken, which leads to the formation of five regions that are depicted in fig. 2.4b. Between x_1 and x_2, the head and tail of the rarefaction wave are traveling left. The solution for ρ, p and u is continuous in this area. The rarefaction wave is clearly discernible for a dilution of $Kn = 0.01$ and $Kn = 0.00001$ depicted in fig. 2.4d. The contact discontinuity at x_3 marks the location to which a particle has traveled from its initial location at x_d in a time Δt. Sod (1978) mentions, that across the contact discontinuity x_3, the macroscopic velocity u and the pressure p are continuous in contrast to the density ρ and the energy E that are shown in fig. 2.4b. Though for a rarefied gas with $Kn = 0.01$ this is not expected as seen in fig. 2.4d. A pronounced contact discontinuity in the density ρ and the energy E is not observed. Labeled as x_4 is the position of the shock wave, at which in general none of the microscopic quantities will be continuous for gases with $Kn = 0.00001$. Again, this does not hold for rarefied regimes shown in fig. 2.4d.
Note, that fig. 2.4a and fig. 2.4b is taken from [21] in order to elaborate the general evolution in time of a gas of $Kn < 0.01$ in Sod's shock tube. Figure 2.4c shows solutions $f(t_i, v, x)$ of the BGK model at $t_0 = 0s$,$t_1 = 0.06$ and $t_3 = 0.12s$ for two levels of rarefaction: $Kn = 0.00001$ and $Kn = 0.01$. Therein the difference when increasing the dilution of a gas in Sod's shock tube is visible: An increased dilution leads to a smooth transition from region 1 to region 5 with the abundance of a pronounced shock front.

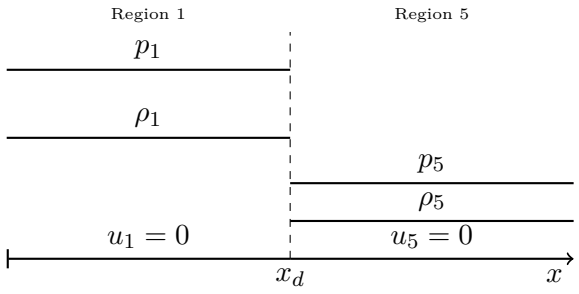

(a) Sod's shock tube at $t = 0$. The whole domain is split into two regions with corresponding initial conditions for pressure p, density ρ, and macroscopic velocity u. The position of the diaphragm is labeled as x_d.

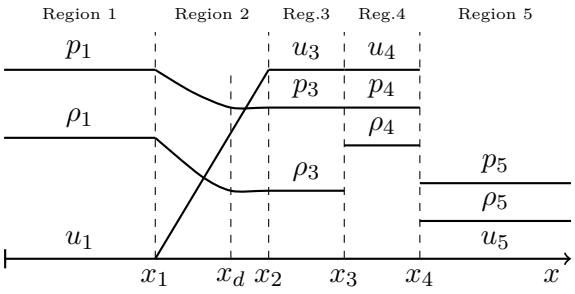

(b) Sod's shock tube at $t > 0$. Shown are pressure p, density ρ and macroscopic velocity u. Five regions can be identified marked out with x_1 and x_2 as head and tail of the rarefaction wave, x_3 as the contact discontinuity and x_4 as the position of the shock wave. The position of the initial diaphragm is labeled x_d. A particle that traveled from x_d during Δt will be located at x_3.

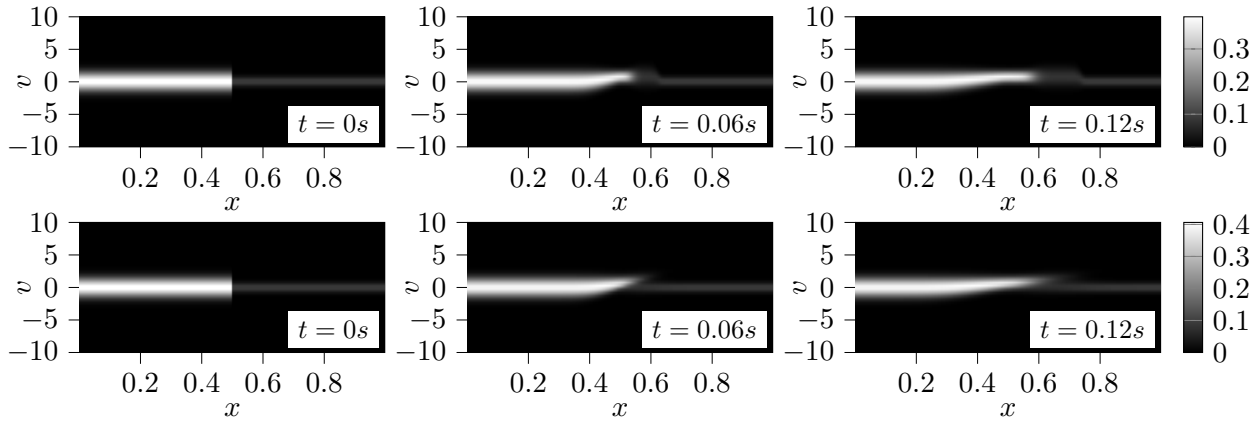

(c) Two solutions of the BGK model $f(t_i, v, x)$ in Sod's shock tube with $Kn = 0.00001$ (top row) and $Kn = 0.01$ (bottom row) for a fixed time t_i. Solutions are presented for $t_0 = 0s$, $t_1 = 0.06s$ and $t_2 = 0.12s$.

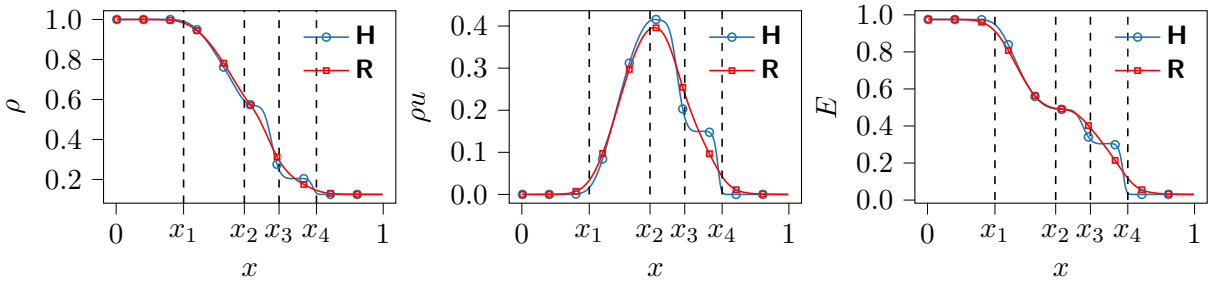

(d) Macroscopic quantities $\rho(x, t_i)$, $\rho u(x, t_i)$ and $E(x, t_i)$ in Sod's shock tube at $t_i = 0.12s$. Displayed are the quantities for $Kn = 0.00001$ and for $Kn = 0.01$, where the former is abbreviated with **H** and the latter with **R**. The locations of head and tail of rarefaction wave x_1 and x_2, contact discontinuity x_3 and shockwave x_4 are labeled.

Figure 2.4: BGK model in Sod's shock tube: Initial conditions and their evolution after Δt are shown in (a) and (b). Two solutions of differing rarefaction levels are presented in (c). Macroscopic quantities of (c) at $t = 0.12s$ are shown in (d).

3 Dimensionality reduction algorithms

This chapter introduces the dimensionality reduction algorithms, which will be applied to solutions of the BGK model in Sod's shock tube: Proper orthogonal decomposition (POD) and Autoencoders (AEs). Firstly, a short introduction of POD is given. Secondly, autoencoders and significant aspects of deep learning are described. The main focus of this thesis lies in the application of autoencoders for which POD serves as a comparative method.

Dimensionality reduction algorithms lie at the heart of any reduced order model (ROM) which is described in the following chapter. As input serve datasets such as solutions of a full order model (FOM) or experimental data. These datasets may contain the dynamics of a spatio-temporal problem. The output is an approximation of the input. It is reconstructed from a low-dimensional representation that captures the underlying dynamics of the input problem.

3.1 Proper orthogonal decomposition (POD)

The solution of PDEs, precisely $f(x, v, t)$, can be approximated either through a discretization into a system of ODEs as described in chapter 2, or alternatively through a separation of variables ansatz

$$f(t, v, x) = \sum_{i=1}^{n} a_i(t)\Phi_i(x, v), \tag{3.1}$$

as descried in [23]. Temporal dependence rendered through $a_i(t)$ is independent from the spatial information carried in $\Phi_i(x, v)$. Here $\Phi_i(x, v)$ is called the i-th basis mode. With increasing i, the accuracy of the solution consequently increases as well, which is similar to increasing the spatial resolution in finite difference methods outlined in chapter 2. The essence of dimensionality reduction algorithms is to find optimal basis modes $\Phi_i(x, v)$. Optimality specifically implies capturing the dynamic answer to a given geometry and initial conditions, thus permitting to exploit a minimal number p of basis modes to reconstruct the dynamics.
An optimal basis can be provided by POD. It leverages a "physically interpretable spatio-temporal decomposition"[23][p.375] of the input data. At first, this data needs to be preprocessed in a fashion, that separates the temporal and spatial axis. Each temporal state is called snapshot and is stacked in a matrix P such that

$$\mathrm{P} = [\mathbf{u}_1, \mathbf{u}_2, \ldots, \mathbf{u}_n] \qquad \text{with} \qquad \mathbf{u}_i = [f(v_1, x_1), \ldots, f(v_k, x_1), f(v_1, x_2), \ldots, f(v_k, x_j)]^T, \tag{3.2}$$

where n is the number of available snapshots and $\mathbf{u}_i$ the i-th snapshot with $\mathbf{u}_i \in \mathbb{R}^{j \times k}$. Afterward, P is decomposed using the singular value decomposition (SVD) which solves the left and right

singular value problem leveraging

$$\mathrm{P} = U\Sigma V^*, \tag{3.3}$$

where U is a unitary matrix containing the left singular vectors of P in its columns and V, also a unitary matrix, containing the right singular vectors in its columns. Here, a superscript asterisk denotes the complex conjugate transpose. Furthermore, Σ is a sparse matrix with the singular values in descending order on its diagonal [23]. Note that the SVD always produces as many singular values and thus singular vectors as existing elements on the shortest axis of the input matrix. Hence, preprocessing the input data as described above delivers as many singular values -and vectors, as there are snapshots, given that the resolution in time is smaller than the spatial resolution.
Next, by applying the Eckard-Young theorem, which can be looked up in [23], it is possible to harness the first leading singular values and corresponding vectors to approximate P to a desired accuracy. The theorem states that the optimal rank-r approximation to P, in a least-squares sense, is given by the rank-r SVD truncation $\tilde{\mathrm{P}}$:

$$\underset{\tilde{\mathrm{P}}, s.t. rank(\tilde{\mathrm{P}})=r}{\operatorname{argmin}} \| \mathrm{P} - \tilde{\mathrm{P}} \|_F = \tilde{U}\tilde{\Sigma}\tilde{V}^*. \tag{3.4}$$

Here $\tilde{U}$ and $\tilde{V}$ denote the first r leading columns of $\mathbf{U}$ and $\mathbf{V}$, and $\tilde{\Sigma}$ contains the leading $r \times r$ sub-block of Σ. $\| \cdot \|_F$ is the Frobenius norm [23].
When decomposing a matrix that contains snapshots of a dynamical system, the columns of $\tilde{U}$ and $\tilde{V}$ encompass dominant patterns that describe the dynamical system. Moreover, they provide "a hierarchical set of modes, that characterize the observed attractor on which we may project a low-dimensional dynamical system to obtain reduced order models"[23][p.8]. That being said, we use the left singular values of $\tilde{U}$ as optimal basis modes such that

$$\tilde{U} = \Phi = [\Phi_1, \Phi_2, \ldots, \Phi_r]\,. \tag{3.5}$$

Vectors in Φ are orthogonal to each other thus supply a coordinate transformation from the high-dimensional input space into the low-dimensional pattern space.

3.2 Autoencoders

An alternative to obtaining an optimal basis is to employ a machine learning architecture situated in the field of deep learning called autoencoders. An autoencoder is a feedforward neural network, that is trained to learn salient features of its input. Hence, the input is compressed and successively reconstructed from the compressed version. Arguably, an autoencoder simply copies its input to its output [5]. Figure 3.1 shows a schematic representation of the architecture for a deep undercomplete autoencoder and the necessary terminology used to describe its components. For now, the difference between an undercomplete and overcomplete autoencoder is ignored, however, introduced when arriving at regularization.
The distinction between encoder and decoder represents the biggest allocation units in autoencoders. They are separated at the central code layer. The encoder is a mapping h. Thus, the encoder maps the input P to the code Φ whilst compressing it, written as $h(\mathrm{P}) = \Phi$. Hence the encoder consists of the input layer, a variable number of hidden layers, and the code layer. This is the left side of the schematic depiction of an autoencoder in fig. 3.1. The decoder mirrors the encoder,

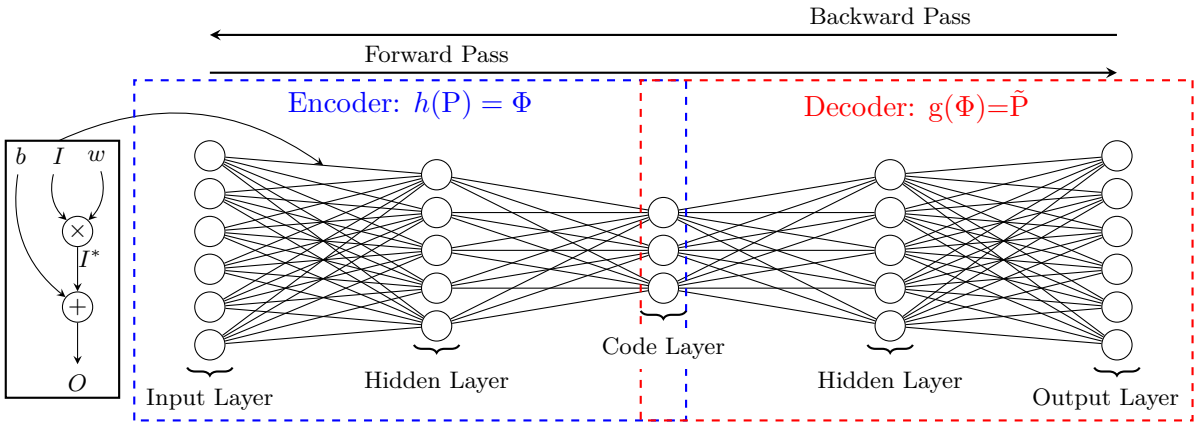

Figure 3.1: Scheme of an undercomplete autoencoder with five fully connected layers. An input layer, an output layer, the code or bottleneck layer, and two hidden layers. Every layer is made up of nodes, represented as circles. More hidden layers deepen the architecture of the autoencoder thus increasing the capacity of the model. Not shown are possible activations for each layer. Labeled are decoder and encoder. The decoder is a mapping $g(\Phi) = \tilde{\mathrm{P}}$, taking Φ as an input, outputting an approximation $\tilde{\mathrm{P}}$ of P. Similarly, the encoder is a mapping $h(\mathrm{P}) = \Phi$, taking Φ as an input and outputting the code Φ. The box, left of the autoencoder, shows a computational graph for the feedforward connection of two nodes. The input of a node is I which is multiplied with w a weight. A bias b is added to the result I^*, which yields the output O, the input of a node right of the initial node.

which is not a necessity but often chosen that way, seen on the right side of fig. 3.1. It comprises the same code layer, a variable number of hidden layers, and the output layer. Similarily it is a mapping g which maps Φ to $\tilde{\mathrm{P}}$, an approximation to the initial P, and is written as $g(\Phi) = \tilde{\mathrm{P}}$. The number of hidden layers in the encoder and the decoder is the first of the so-called hyperparameters that can be tuned to improve the performance of the autoencoder. Note that autoencoders with more than one hidden layer, the code layer, are referred to as deep autoencoders. The reverse is termed shallow autoencoder. The second-largest allocation unit in autoencoders (and in general neural networks) are the layers. Each layer can be a vector, a matrix, or a three-dimensional tensor. For the time being, each layer is chosen to be vector-valued. Therefore, the input layer can be an input vector e.g. $\mathbf{u_1} \subseteq \mathrm{P}$. The vectors in the hidden layers are abstractions of the input. The term hidden stems from the fact, that one usually does not look at them as the interest mainly lies in the code -and output layer. The code layer is of main interest, as it holds the compressed abstraction of the input. Coming to the smallest allocation unit, the nodes. Each node refers to an entry in the vector/layer and is displayed as a circle in fig. 3.1. The number of nodes per hidden layer is a second hyperparameter. Two nodes are connected in a forward pass through solving $O = I * w + b$. This is represented as a computational graph in fig. 3.1. Here the input is I is multiplied with a weight w, and by adding a bias b, one obtains the output O. Hence every connection between nodes contains two free parameters: a weight w and a bias b. Hence the whole network holds a set of parameters which we call $\theta \in \mathbb{R}$ in the following. A forward pass in this sense refers to the flow of information from the left side of the encoder to the right side of the decoder in fig. 3.1. The aforementioned is provided in [5].

3.2.1 Training

In a feedforward neural network the information flows forward from the input layer to the output layer evaluating $AE(\mathrm{P}) = g(h(\mathrm{P})) = \tilde{\mathrm{P}}$. When applied, the layer structure in fig. 3.1 equates to a composition of functions

$$l^{(4)}(l^{(3)}(l^{(2)}(l^{(1)}(l^{(0)}(\mathrm{P}))))) = g(h(\mathrm{P})) = AE(\mathrm{P}) = \tilde{\mathrm{P}}, \tag{3.6}$$

where every function represents one layer. Here $l_{(0)}$ and $l_{(4)}$ are input layer and output layer, $l_{(1)}$ and $l_{(3)}$ the hidden layers in the encoder and the decoder respectively with $l_{(2)}$ the bottleneck layer. The evaluation of one layer or function is a linear transformation of the incoming data with

$$\tilde{\mathbf{u}}_1 = \mathbf{u}_1 W + \mathbf{b}. \tag{3.7}$$

Here $\mathbf{u}_1$ can be chosen as in eq. (3.2), W is the weight matrix and $\mathbf{b}$ a bias vector, which is the same equation as shown in the computational graph in fig. 3.1. The weight matrices and bias vectors of each layer are aggregated in the set $\theta \in \mathbb{R}$. θ does not minimize the cost function $J(\theta)$ from the start with

$$J(\theta) := \frac{1}{n}\sum_{i=1}^{n}(\mathbf{u}_i - AE(\theta; \mathbf{u}_i))^2, \tag{3.8}$$

and needs to be optimized through a learning process, which is called training. Note that the cost function $J(\theta)$ comprises the mean squared error over all snapshots $\mathbf{u}_i$, written as $L(\mathrm{P}, \tilde{\mathrm{P}})$ the so-called loss with

$$L(\mathrm{P}, \tilde{\mathrm{P}}) := \frac{1}{n}\sum_{i=1}^{n}(\mathbf{u}_i - \tilde{\mathbf{u}}_i)^2 = E, \tag{3.9}$$

when specifically referring to E the distance between P and $\tilde{\mathrm{P}}$. In order to minimize $J(\theta)$, the gradient of $J(\theta)$ with respect to the free parameters θ written as $\nabla_\theta J$ is required. In particular, the derivative of the network with respect to the free parameters as seen in eq. (3.8). The opposite direction of the gradient yields an update of θ. The so-called learning rate ϵ determines the magnitude of the updates with

$$\theta \leftarrow \theta - \epsilon\, \mathbf{g}\,, \qquad \text{where} \qquad \mathbf{g} := \nabla_\theta J. \tag{3.10}$$

Backpropagation: The computation of the gradient $\mathbf{g}$ is performed with the backpropagation algorithm. As the name implies, the information flows backward through the network, from output layer to input layer, and propagates E backward through the network. Responsible for this backward motion is the recursive application of the chain rule of calculus. Considering as a simple illustrative example fig. 3.2 with $y = g(z, b) = g(f(x, a), b)$, a single node connection from input x to output y with a single hidden node. Then a is a weighting constant of the first node and b defines a weighting constant of the hidden node. Backpropagating the distance E with $E = \frac{1}{2}(y_0 - y)^2$ between the output and the ground truth y_0 though the network yields

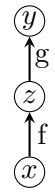

Figure 3.2: A single node network with one hidden node between input and output node.

$$\frac{\partial E}{\partial a} = -(y_0 - y)\frac{\partial y}{\partial z}\frac{\partial z}{\partial a} \qquad \text{and} \tag{3.11}$$

$$\frac{\partial E}{\partial b} = -(y_0 - y)\frac{\partial y}{\partial b}, \tag{3.12}$$

which requires $\frac{\partial E}{\partial a} = -(y_0 - y)\frac{\partial y}{\partial z}\frac{\partial z}{\partial a} = 0$ to minimize E. The update rule is then given by

$$a_{i+1} = a_i + \epsilon\frac{\partial E}{\partial a_i} \qquad \text{and} \qquad b_{i+1} = b_i + \epsilon\frac{\partial E}{\partial b_i}. \tag{3.13}$$

This example is taken from [23] and shows how the chain rule of calculus provides the backward direction when deriving the gradients of each layer with respect to the free parameters.

Generalization: The objective for training a neural network is called generalization. The difference between pure optimization and learning lies in the differing objectives. Pure optimization minimizes a cost function like $J(\theta)$ in order to fit P to $\tilde{\mathrm{P}}$. That is the objective of the optimization task. Learning uses the same objective as the optimization task but equally cares about the so-called generalization task. Generalization is the ability of the learning algorithm to not only fit the input data but at the same time to fit different data from the same source. Thus, using salient features of the input data enables generalization, which can only be achieved to a certain extent and is sometimes intractable. But how is the generalizing performance measured? The input data P is randomly shuffled and split it into a training and a validation set in a 80/20 fashion with $\mathrm{P} = \{\mathrm{P}_{train}, \mathrm{P}_{val}\}$. The random shuffling eliminates any bias on both sets. Then $J(\theta)$ is minimized using only P_{train} which minimizes $L(\mathrm{P}_{train}, \tilde{\mathrm{P}}_{train})$ and it is checked if indirectly $L(\mathrm{P}_{val}, \tilde{\mathrm{P}}_{val})$ is being minimized as well. The indirect minimization of $L(\mathrm{P}_{val}, \tilde{\mathrm{P}}_{val})$ is called the generalization task. The loss over the validation set is called the validation error. The loss over the training set is called the training error. Both are equally valued. As previously stated, an optimal basis Φ that specifically contains salient features of P is sought for. By minimizing only the optimization task, the same basis as in POD is acquired. With learning, it is tried to find an even more powerful basis Φ that enables the network to generalize.

Initialization: Initial values of θ are crucial for the success of any neural network to learn something useful in a reasonable time since a strong bias is introduced to the network, considering that Adam only makes marginal contributions to θ at every update. Usually, the biases have a heuristically constant value. The weights are required to break the symmetry between nodes. For example, if two hidden nodes with the same activation function are connected to the same input, then the same gradient would lead to symmetric evolution during training. Thus, making one of the nodes redundant. Therefore weights are initialized randomly drawn from a Gaussian distribution. The spectrum of initial weight sizes ranges from large initial weights to small initial weights and sparse initialization. If the scale of the distribution yields large weights, then all nodes are characteristically connected and symmetry is broken. Contrarily, small initial weights give less connectivity. Thus, the learning algorithm can connect nodes and choose the strength [5].
Several heuristics for the scale of the initial weights exists. Each preserves the norm of the weight matrix of each layer to stay close to or below unity. Envisage that during forward propagation and backward propagation matrix multiplications from one layer to the next are performed. Keeping the norm of each layer from exceeding unity prevents the development of exploding values and gradients in the respective last layer. A preventive measure is to scale the distribution for one layer with respect to its non-linear activation with a factor called gain. Gains for non-linear activations can be found in [**?**] along with several sampling methods. The effects described above become severe with large layers or equally with networks of a certain depth. This is not the case for the autoencoders used in this thesis allowing comfortably to choose the default initialization in `pytorch` for linear -and convolutional layers, where the initial weights are drawn from a normal distribution

with $U(-\frac{1}{\sqrt{m}}, \frac{1}{\sqrt{m}})$ as suggested in [24]. The number of input nodes, also called fan-in, per layer, is m.
More details are available in [5], and initialization for deep networks with more than eight layers and rectifying non-linear activations see [25].

Adam: The algorithm to compute the updates to θ is called Adam, introduced by Kingma(2017) [26]. Adam is an upgraded version of the classic stochastic gradient descent algorithm (SGD) with moments. The name stems from adaptive moment estimation, which refers to the adaptation of moments which in combination with the learning rate ϵ applies scaled, directional updates to θ during training. The steps of Adam are shown in algorithm 1. Initial hyperparameters are the step size/learning rate ϵ, the exponential decay rates d_1 and d_2 in $[0, 1)$ and a small constant δ for numerical stability. The default values are $\epsilon = 1e-2$, $d_1 = 0.9$, $d_2 = 0.999$ and $\delta = 1e-8$. Note, despite the learning rate ϵ, Adam is fairly robust w.r.t. changing it's hyperparameters. Hence solely the hyperparameter ϵ requires tuning [5]. SGD derives from the common gradient descent

Algorithm 1: The Adam algorithm

Require: Step size ϵ
Require: Exponential decay rates from moment estimates d_1 and d_2 in $[0, 1)$
(Suggested defaults: 0.9 and 0.999 respectively)
Require: Small constant δ used for numerial stabilization (Suggested default: 10^{-8})
Require: Initial parameters θ
Initialize 1st and 2nd moment variables $\mathbf{s} = 0$ and $\mathbf{r} = 0$;
Initialize time step i = 0;
while *stopping criterion not met* **do**
Sample a minibatch $\mathrm{P_i}$ containing m examples from the training set P_{train};
Compute gradient: $\mathbf{g} \leftarrow \frac{1}{m}\nabla_\theta \sum_m L(\mathrm{P_i} - AE(\theta; \mathrm{P_i})$;
$t \leftarrow t + 1$;
Update biased first moment estimate: $\mathbf{s} \leftarrow d_1\mathbf{s} + (1 - d_1)\,\mathbf{g}$;
Update biased second moment estimate: $\mathbf{r} \leftarrow d_2\mathbf{r} + (1 - d_2)\,\mathbf{g} \circ \mathbf{g}$;
Correct bias in first moment: $\hat{\mathbf{s}} \leftarrow \frac{\mathbf{s}}{1-d_1^t}$;
Correct bias in second moment: $\hat{\mathbf{r}} \leftarrow \frac{\mathbf{r}}{1-d_2^t}$;
Compute update: $\Delta\,\theta = -\epsilon\frac{\hat{\mathbf{s}}}{\sqrt{\hat{\mathbf{r}}}+\delta}$ (operations applied element-wise);
Apply update: $\theta \leftarrow \theta + \Delta\,\theta$
end

method, where the whole batch P_{train} is used per iteration to compute the gradient for an update of θ. Therefore gradient descent is a batch gradient method or deterministic gradient method. SGD is a stochastic method. It approaches updates for θ as in eq. (3.10) in a stochastic manner, using only small portions of P_{train} per update. Randomly sampling only a small number of examples from P_{train} and taking the average gradient, computes an unbiased estimate of the true gradient, which is cheaper. Additionally, SGD can find a minimum even before processing the whole batch, important especially for large datasets [5]. Unfortunately, this leads to noisy updates of θ. Thus, SGD trains with mini-batches of size κ, delivering $\mathrm{P}_{train} = \{\mathrm{P}_{t_i}, \ldots, \mathrm{P}_{t_n}\}$. Here i counts through all the mini-batches, n is the total number of mini-batches. The mini-batch size κ constitutes yet

another hyperparameter. Minibatch sizes κ touch the following observations: One minibatch can be processed in parallel to compute an update. Hence, small κ underutilize multicore architectures. Large κ, on the other hand, can be limited by available memory. Furthermore, small κ can have a regularizing effect, which improves generalization. But they amplify the noisy behavior. Therefore, noisy updates require a small learning rate or equally one that decays over time. Besides, κ of the power of two is advised for graphics processing units (GPUs) to fully exhaust the hardware (array sizes of the power of two achieve better runtime in GPUs)[5]. Up to now, small mini-batches improve generalization, underutilize available multicore hardware and amplify noisiness which needs to be tackled with small learning rates. Hence, the learning process is slow. Momentum can stabilize training besides reducing the learning rate.
Momentum applies an exponentially decaying moving average of previous gradients to the current gradient. It is an analogy to momentum in physics and therefore named after. Goodfellow(2016) consults the following examples to explain momentum. A tightrope walker uses the moment of inertia of a long rod for balance as crossing the rope. Oscillations of the walker need to overcome the moment of inertia of the long rod to destabilize the walker. Equally, a fast car taking a sharp turn will drift because of momentum. The new direction is influenced by the old orthogonal momentum. The update rule for the first moment estimate $\mathbf{s}$ of Adam in algorithm 1 gives for three consecutive updates

$$\mathbf{s}_i = d_1\mathbf{s}_{i-1} + (1-d_1)\mathbf{g}_i, \tag{3.14}$$
$$\mathbf{s}_{i-1} = d_1\mathbf{s}_{i-2} + (1-d_1)\mathbf{g}_{i-2}, \tag{3.15}$$
$$\mathbf{s}_{i-2} = d_1\mathbf{s}_{i-3} + (1-d_1)\mathbf{g}_{i-3}. \tag{3.16}$$

A combination and simplification gives

$$\mathbf{s}_i = d_1d_1(1-d_1)\mathbf{g}_{i-2} + \cdots + d_1(1-d_1)\mathbf{g}_{i-1} + \cdots + (1-d_1)\mathbf{g}. \tag{3.17}$$

Past gradients contribute to the current gradient, just like in the car example or the tightrope walker. Moreover, these contributions vanish exponentially over the iterations. This leads to a moving average of past and current gradients, which is called momentum. Note, the entanglement of updates is taken from [27].
Now taking into account that if eq. (3.14) computes the moment of the first iteration, there are no previous gradients available which leads to a biased first computation. Hence $\mathbf{s}_i$ is divided by $(1-d_1^i)$ for the bias correction of the first moment in algorithm 1 which yields $\hat{\mathbf{s}}$. In consecutive iterations, the bias correction approaches zero. The same steps apply to the second biased moment estimate $\mathbf{r}$. It is nothing more than the squared past gradients written as $\mathbf{g}\circ\mathbf{g}$ in algorithm 1. Together they form the parameter update $\Delta\,\theta$. Without going into further details, it is shown in [26] that the parameter updates have an approximate upper bound of $\Delta\,\theta \lessapprox \epsilon$, see [26]. This upper bound is a necessary criterion for the updates, as the learning rate ϵ is a specifically tuned hyperparameter that should not be exceeded a threshold during training. The ratio $\frac{\hat{\mathbf{s}}}{\sqrt{\hat{\mathbf{r}}}+\delta}$ is called signal to noise ratio (SNR) in [26], which evolves towards zero as an optimum is reached. Furthermore, the updates are invariant to the scale of the gradients. The factor a cancels out with $(a\cdot\hat{\mathbf{s}})/\sqrt{(a^2\cdot\hat{\mathbf{r}})} = \hat{\mathbf{s}}/\sqrt{\hat{\mathbf{r}}}$. To sum up, using first and second momentum accelerates training because the moving average gradient smooths the noisy updates. Thus, giving a better estimate of the true gradient. The bias is corrected in the first iteration and invariance to gradient scaling is provided. The flowchart in fig. 3.3 shows how the generalization query, weight initialization, backpropagation,

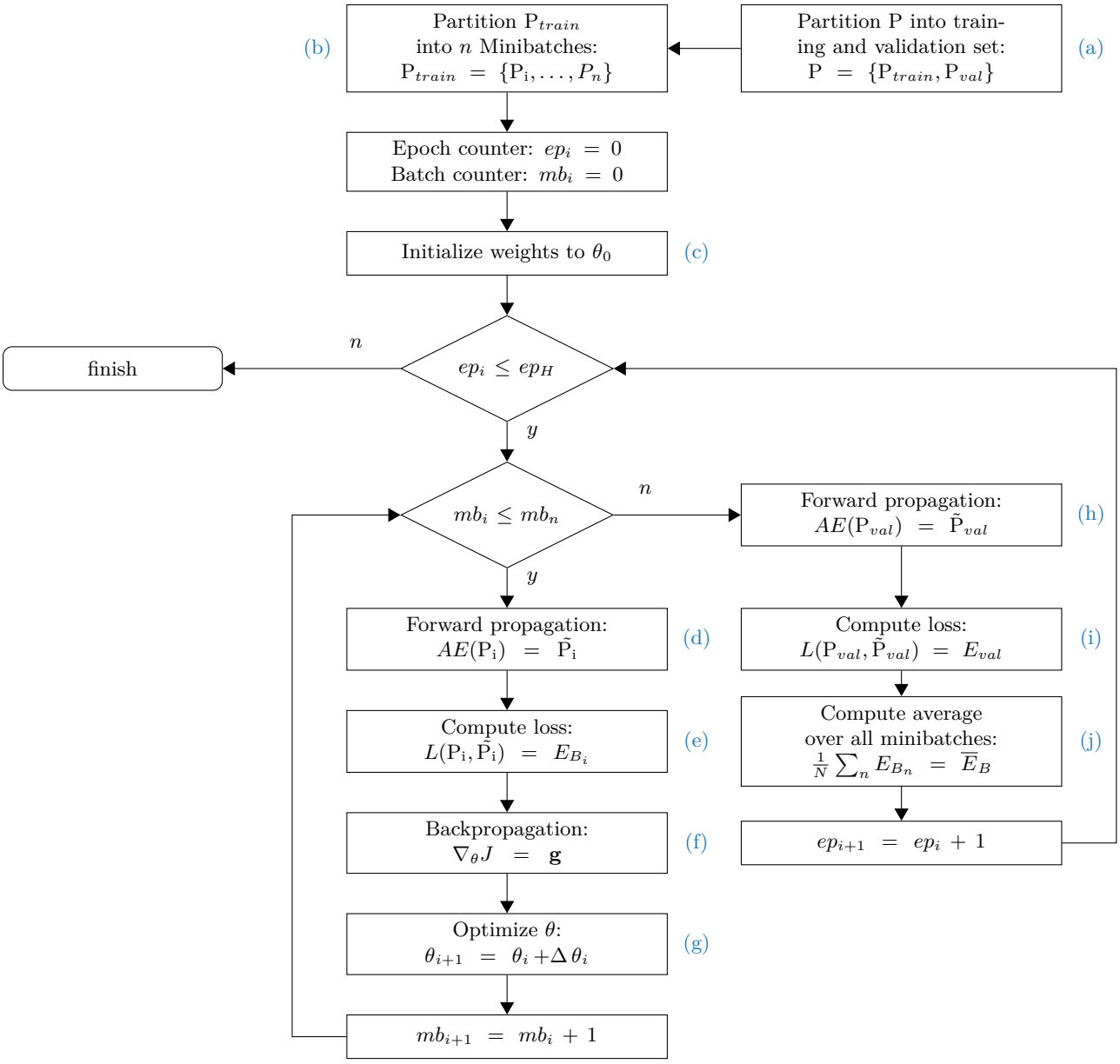

Figure 3.3: Flowchart of the training process used in this thesis for an autoencoder. The data set P for training is split up into a training P_{train} and a validation P_{val} set with a 80/20 ratio (a). The P_{train} set is equally devided into n minibatches (b). The network will be trained over H epochs and n minibatches. First the weights w are initialized as in [24] and biases set to zero (c). A successive evaluation of the first minibatch with $AE(\mathrm{P_{i}}_i) = \tilde{\mathrm{P}}_{\mathrm{i}i}$ called forward propagation takes place in (d). The mean squared error between $\mathrm{P}_{\mathrm{i}i}$ and $\tilde{\mathrm{P}}_{\mathrm{i}i}$ yields the average error over one minibatch E_{B_i}. Thereafter E_{B_i} is backpropagated through the network (f) yielding the gradient $\mathbf{g}$. This gradient is then used to optimize weights w and biases b with *Adam*, an optimization algorithm seen in algorithm 1, (g). In the fashion of using (d) to (g) all n minibatches are shown to the network and lead to an optimization of the network's free parameters θ which are weights w and biases b. After all minibatches are shown to the network a validation step is taken. Hence the network evaluates P_{val}, which it has not seen before, in (h) with $AE(\mathrm{P}_{val}) = \tilde{\mathrm{P}}_{val}$. Subsequently, the evaluation of the mean squared error between P_{val} and $\tilde{\mathrm{P}}_{val}$, produces the validation error E_{val} in (i). Afterwards the arithemtric mean of all minibatch errors E_{B_i} is taken. This produces $\overline{E}_B$ and concludes the first epoch. The maximum number of epochs H is reached when E_B and E_{val}, have dropped to a satisfactory value and the training finishes.

and the integration of Adam into the training procedure within this thesis. The training encompasses two loops. The outer loop runs over so-called epochs. The inner over the mini-batches. One epoch completes after the network saw all mini-batches. Finally, the validation error and the training error are calculated. The number of epochs H is determined based on over- and underfitting and how many epochs Adam needs to converge, which is yet another hyperparameter.

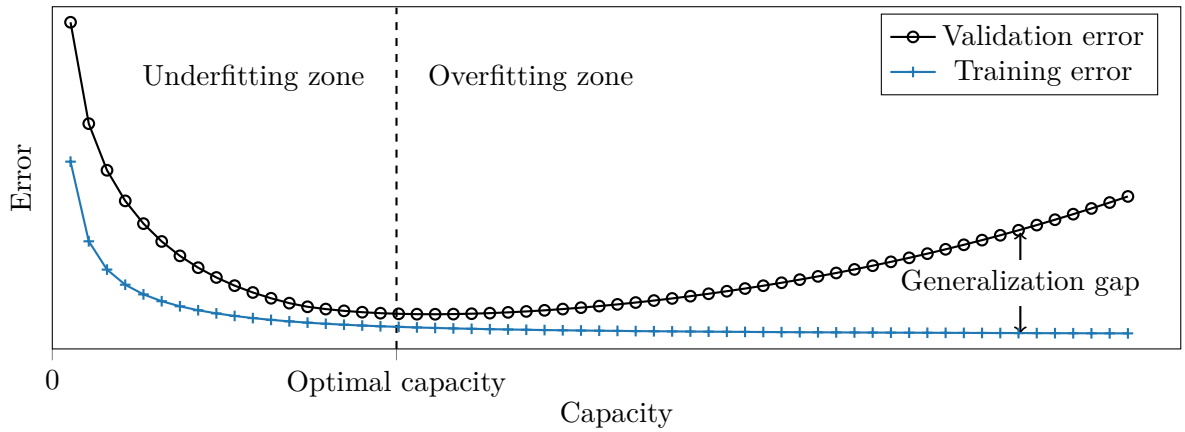

Figure 3.4: This is a figurative example of capacity influencing the evolution of training and validation error. Increasing the capacity enables the model to fit the training and validation set thus both error decreases. Typically the training error is smaller than the validation error. Yet both errors are too high. The model underfits. A further increase of capacity equally increases the validation error with decreasing the training error further. The gap between training- and validation error is called the generalization gap. Once the generalization gap dominates the training error, the model is overfitting. The capacity passed the point of optimality. Optimal capacity is the point where both optimization and generalization are in balance.

Capacity, regularization, over- and underfitting: To satisfy the objective of learning an optimal basis in the code layer, autoencoders need to be regularized. Regularization is defined as "any modification made to a learning algorithm that is intended to reduce its generalization error but not its training error"[5][p.117]. As previously mentioned, autoencoders have a central hidden layer between the equally sized input -and output layer. In undercomplete autoencoders, the central hidden layer is called the bottleneck layer, because its size is smaller than the input. Thus the undercomplete autoencoder is forced to decide which information to copy and by that measure is regularized. Overcomplete autoencoders on the other hand have the central hidden layer greater or of the same size as the input, thus making it indispensable to use additional regularization, which, necessary to add, can be also fruitful in undercomplete autoencoders. Note that an undercomplete autoencoder as shown in fig. 3.1 is used in this thesis which is called autoencoder for simplicity. Regularization is always advantageous when the capacity of an autoencoder is too big. The capacity of any neural network can be altered through the number of free parameters available for the model to fit the input data. Recall that an autoencoder has a variable number of hidden layers (excluding the bottleneck layer) of variable size and thus a variable number of free parameters. For example having a model big enough in terms of free parameters to memorize the whole training set, good results would be achieved for the optimization task, but missed out on learning useful features thus failing at the generalization task. This relationship is shown in fig. 3.4 where a point of optimal capacity is defined. Optimal capacity is reached when optimization and generalization in the form of training error and validation error are in balance. Note that fig. 3.4 is taken from [5][p.112].

Another way that alters the capacity of a neural network is to add non-linear activation functions to layers. So far every node and by that layers are connected through linear transformations as in eq. (3.7). Thus the network's so-called hypothesis space solely includes linear transformations of the input. The hypothesis space from which a neural network can choose the composition of the solution can be enriched with non-linear functions by simply evaluating layers through non-linear functions σ, also called activations, leading to

$$\tilde{\mathbf{u}}_1 = \sigma(\mathbf{u}_1 W + \mathbf{b}). \tag{3.18}$$

Activations: Non-linear activations typically used for neural networks are summarized in table 3.1. In this thesis, these are also the activations used in the final network design or during hyperparameter search. Two classes of activations are used. One is of type rectifier, which is linear for positive inputs and is zero, or decay below linear for negative inputs. The other is the hyperbolic tangent (Tanh) and the Sigmoid-weighted linear unit (SiLU). Tanh and sigmoid share a similar "S"-shaped curve hence are put in one class. SiLU can be written as $\text{SiLU} = \frac{1}{2}x(1+\tanh(\frac{x}{2}))$. Note that Tanh saturates for input values exceeding the range $[-2, 2]$ which leads to a so-called vanishing gradient. In the most severe case, all updates can be zero. However, in this thesis, a vanishing gradient was not encountered. Theoretically, it is possible to take any function as an activation. Though indispensable is their differentiability, which reduces to partly differentiable for rectifiers, to allow backpropagation. Activations σ and to place them in the network is yet another hyperparameter.

Table 3.1: Non-linear activation functions of type rectifier are the rectified linear unit (ReLU), it's leaky variant LeakyReLU, the exponential version ELU. The negaive slope of LeakyReLU below zero α is typically, and also in this thesis set to $\alpha = 0.001$. Activations based on the hyperbolic tangent (Tanh) are the sigmoid function with $\text{sig}(x) = \frac{1}{2}(1+\tanh(\frac{x}{2}))$ and it's variant SiLU. The functions are shown over an illustrative domain.

ReLU	LeakyReLU	ELU	SiLU	Tanh
$\sigma = \begin{cases} x, & \text{if } x \geq 0 \\ 0, & \text{if } x < 0 \end{cases}$	$\sigma = \begin{cases} x, & \text{if } x \geq 0 \\ \alpha x, & \text{if } x < 0 \end{cases}$	$\sigma = \begin{cases} x, & \text{if } x > 0 \\ \alpha(e^x - 1), & \text{if } x \leq 0 \end{cases}$	$\sigma = x\text{sig}(x)$	$\sigma = \tanh(x)$
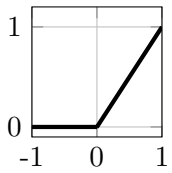	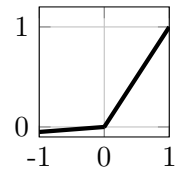	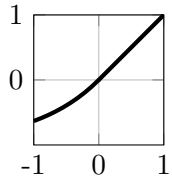	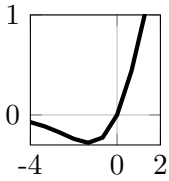	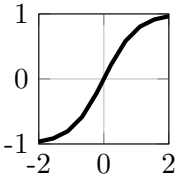

Layer types: The idea that, for two successive layers, all nodes from the first layer are connected to all nodes from the following layer and that all layers are vectors, has been adopted. Hence the types of layers are called fully connected or `Linear` in `pytorch`[**?**]. If now the input is a vector, a matrix, or a three-dimensional tensor another type of layer called convolutional layer has to be used. In `pytorch` these layers are called `Conv1D`, `Conv2D` and `Conv3D` respectively. To begin with, a simple example is given to illustrate conceptual features of convolutional layers. A digital image can be viewed as a distribution of pixels over a two-dimensional surface, where the dimensions of the surface are described with the width and height of the image. Furthermore, each pixel has a color expressed in values of the primary colors red, green, and blue (RGB). Hence each pixel is a combination of different RGB values. The RGB values for each pixel are stored in so-called channels. The red channel, green channel, and blue channel. This concludes, that the dimension of

a digital image is additionally equipped with the channel dimension. Let an image be Img, then $Img \in \mathbb{R}^{m \times n \times c}$, with m the width of this image, n the height of this image and c the three RGB channels. Another important characteristic of images is the spatial correlation between neighboring pixels. This can be for example sharp corners that separate foreground from background or differentiate between entities portrayed in the image. Therefore similarly to saving information about color composition in channels, we can imagine saving spatial information in additional channels. For example corners and other geometric shapes, saved in channels for themselves. With this idea in mind, convolutional layers can be introduced. Convolutional layers comprise a so-called kernel, which moves over the image and by that all the input channels. Therefore, if the kernel is K then $K \in \mathbb{R}^{i \times j \times c}$. The height i and width j of the kernel can be adjusted and is usually smaller than the input's height and width. The c dimension is always equal to the c dimension of the input. The distance the kernel travels over the input at every step is specified with the so-called stride s. For a two dimensional input image like Img the strides are given in direction s_1 and s_2, where the latter corresponds to m and the former corresponds to n of the Img. The kernel performs the same linear transformations of the input as fully connected layers at every part of the input visited. This action outputs a so-called feature map, which as the name implies should capture features of the input. A comparison of a one strided convolution with $s_1 = s_2 = 1$ and a two strided convolution with $s_1 = s_2 = 2$ is given in fig. 3.5. The one strided convolution yields a feature map with a reduction of m and n by one, while the two strided convolution yields a feature map with a reduction of m and n by two. Note that in fig. 3.5 eventual channels are omitted.
Even though the name convolutional layer implies the use of the convolutional operation `PyTorch` and other neural network libraries instead use the cross-correlation operation, which is an operation closely related to the convolution [5] [**?**]. Details on why the cross correlation is used instead of the convolution are available in [5]. In eq. (3.19) the two dimensional discrete cross correlation without channels is given with

$$M_{m,n} = \sum_{i,j} Img_{((m-1)\times s_1)+i,((n-1)\times s_2)+j} K_{i,j}. \tag{3.19}$$

Here $M_{m,n}$ represents a point on a feature map, where m and n refer to the location of that point. The input to the cross correlation is exemplary the image Img, where coordinates of a pixel are also given in m and n. The kernel is given as K with coordinates in i and j. The summation in eq. (3.19) is evaluated over i, j. For example, taking a point on M at $m = 1$ and $n = 1$ with $s_1 = 1$ and $s_2 = 1$, then the summation is performed over all pixels of Img that the kernel covers in i and j from the starting point $m = 0$ and $n = 0$ on Img. Further, by moving to $m = 2$ as seen in fig. 3.5 (a), the new starting point on Img is at $m = 1$ and $n = 0$. Hence, the kernel K moved along the m axis of the input image Img. Eventually the kernel will cover the whole input Img.
If many features are present in the input then more feature maps are required. Thus, more kernels can be specified to move over the input, which yields as many feature maps as there are kernels. In fig. 3.6 an illustrative example of a convolutional neural network with four convolutional layers, which downsamples the width and height of the input in every layer while adding channels (feature maps) in every layer. When arriving at the last convolutional layer, the feature maps are flattened and fully connected to the code layer. A comparable scheme for the encoder side of a convolutional autoencoder is used in this thesis. The decoder is acquired by mirroring the encoder in fig. 3.6 at the code layer and replacing all convolutional layers with transposed convolutional layers. With encoder and decoder, the architecture arrives at the typical autoencoder architecture as in fig. 3.1. In conclusion, five additional hyperparameters can be identified for a single convolutional layer:

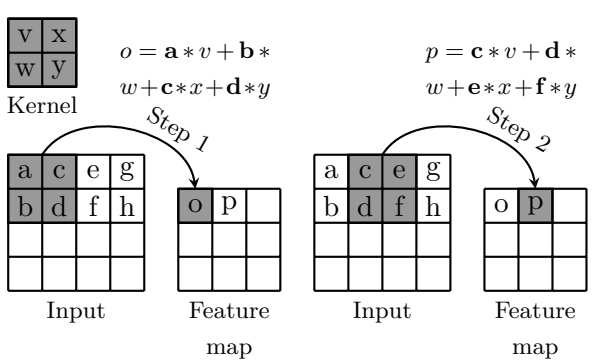

(a) Two dimensional example of a **one** strided convolution over a 4×4 input matrix with a 2×2 kernel matrix. The equations for obtaining the components i and j of the feature map are given. Note that all biases are omitted for simplicity and bold symbols should help readability and do not represent vectors. The resulting feature map is a 3×3 matrix, as the input is downsampled by a factor of 0.75.

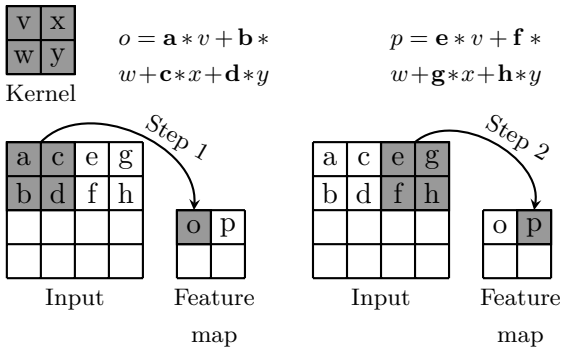

(b) Two dimensional example of of a **two** strided convolution over a 4×4 input matrix with a 2×2 kernel matrix. The equations for obtaining the components i and j of the feature map are given. Note that all biases are omitted for simplicity and bold symbols should help readability and do not represent vectors. The resulting feature map is a 2×2 matrix, as the input is downsampled by a factor of 0.5.

Figure 3.5: Comparison of a one strided convolution (a) and a two strided convolution (b). Illustrated are two steps of a kernel matrix moving over an input matrix. The two strided convolution yields an increased downscaling compared to the one strided convolution.

kernel width and height, number of feature maps, usually called output channels, and stride in two directions.

Fully connected layers can down- and upsample making them applicable for the decoder and encoder in autoencoders. This applies also to convolutional layers, nevertheless not every downsampling can be reversed with convolutional layers. Hence the transposed convolutional layer is introduced. The respective modules for vectors, matrices and three dimensional tensors are called `ConvTranspose1d`, `ConvTranspose2d` and `ConvTranspose3d` in `pyTorch`. The transpose of a convolutional layer has nothing in coming with the transposition of a matrix. The transpose simply refers to recovering a specific shape. Note, that a transpose of a convolutional layer can be viewed as a convolutional layer in which the backward- and forward passes are swapped. Thus they are often implemented in that way [5] [28] [29]. In fig. 3.7a and fig. 3.7b two simplified examples of two dimensional transposed convolutions without channels are sketched out. In both figures, with point a of the input a linear transformation is performed with every kernel entry k_1 to k_6 resulting in the first part of the upsampled output located at the upper left corner. This first part is of the same size as the kernel. Linear transforming a successive point b of the input with all six kernel entries gives the second part of the upsampled output. Again, the second part is of the same size as the kernel. The distance the two parts separate from each other on the output is determined by the stride. When the stride in one direction is shorter than the kernel in that direction, both parts overlap. Overlaps are added and therefore constitute bigger values. In fig. 3.7a this process is shown for an 3×3 input matrix, which is upsampled by a 3×3 kernel moving with stride length $s_1 = s_2 = 2$. The upsampled result is of size 7×7. With a kernel size of 3 in one direction and a stride $s_1 = 2$ in the same direction, there is always an unevenly distributed overlap in the output entries resulting in the checkerboard structure as seen in fig. 3.7a. This is a common problem with transposed convolutional layers. When the kernel width and height are divisible by the respective stride length

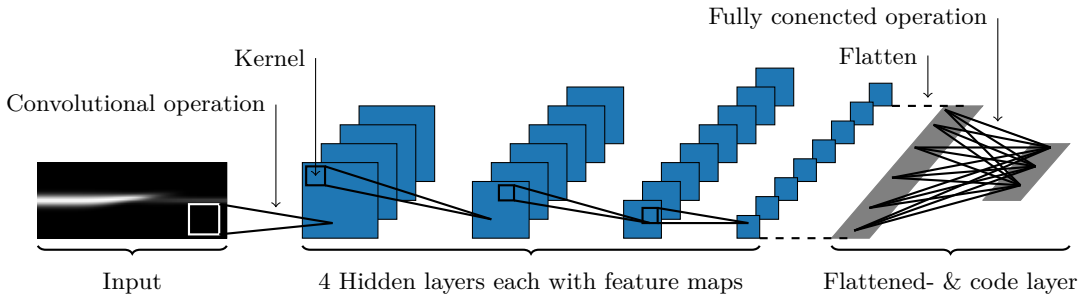

Figure 3.6: Schematic representation of typical components and their structural set-up in a convolutional neural network (CNN). Shown is the convolutional operation and the associated kernel, the flattening and successive fully connected operation. First a kernel moves over the one dimensional input performing convolutional operations, which yields the components of a feature map in the successive hidden layer. One channel in a hidden layer can aswell be called feature map. Here the input has just one channel, but four different kernels move over the input which produces four feature maps in the first hidden layer. Hence the first hidden layer comprises four channels or feature maps. Whenever one layer has different channels, the kernel moves with different parameters over all channels at the same time. Therefore we can think of it in this case as a three dimensional kernel tensor. Note that for simplicity this is not depicted in this figure. While the width and height of the input decreases over the hidden layers, the number of channels typically increases . The last hidden layer is flattend and successively connected to the code layer through a fully connected operation.

s_1 and s_2 this issue can be mitigated, as the overlaps are evenly distributed. For example, when the stride lengths $s_1 = s_2 = 3$ are of the same size as the kernel width and height no overlap occurs. This case is depicted in fig. 3.7b.
Transposed convolutional layers have the same hyperparameters as convolutional layers. Their impact on the down- and the upsampling rate is non-negligible. But customizing both hyperparameters only that matter can be detrimental for learning off the input. For example, a kernel can be too small thus miss overkill edges in pictures. Similarly, a large step size that overpasses thin edges. Hence kernel size and stride width are somewhat determined by the structure of the input. Through zero-padding outlines of the input, down- and upsampling rates can be tuned independently from kernel size and stride width. Zero-padding is available for convolutional layers as well as for the transpose of convolutional layers. It refers to padding the outer edges of the input with zeros. Putting everything together, the output size of convolutional layers and transposed convolutional layers can be computed with

$$o = \left[\frac{i + 2p - k}{s}\right] + 1 \qquad (3.20) \qquad \text{and} \qquad o = (i-1)s - 2p + k \qquad (3.21)$$

respectively. Here all variables are the sizes of one-dimension e.g. the width of an image. Hence, o is the output, i the input, $2p$ the padding of opposing edges, k the kernel, and s to the stride size. Besides, whenever the stride width exceeds the input size in a particular direction, then the input is automatically padded with the necessary number of zeros on the left or bottom. Note, nearly every transpose of a convolutional layer can be described by an associated convolutional layer for which the input is spread using zeros in between every point. Calculating output sizes of convolutional layers and transposed convolutional layers is available in [30].
Neural networks have many hyperparameters determining their capability for learning which were introduced in this section. There is little systematic knowledge about how the hyperparameters interact in the model. Goodfellow(2016) points out that with a combination of intuition, specific

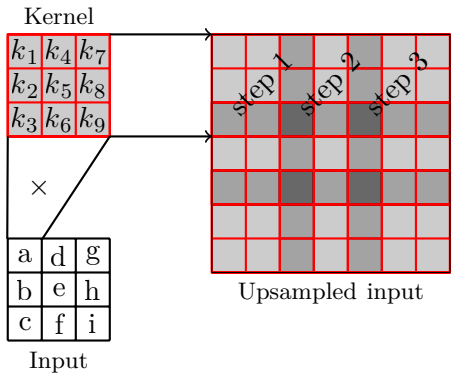

(a) Mechanism of a two dimensional **two** strided transposed convolution over a 3×3 input matrix with a 3×3 kernel matrix. Upsampled by a factor of 2.33 produces a 7×7 matrix. Three kernel locations on the output are indicated with step 1, step 2, and step 3. The extent of the kernel is not divisible by the stride width. Uneven overlapping produces a checkerboard-like structure.

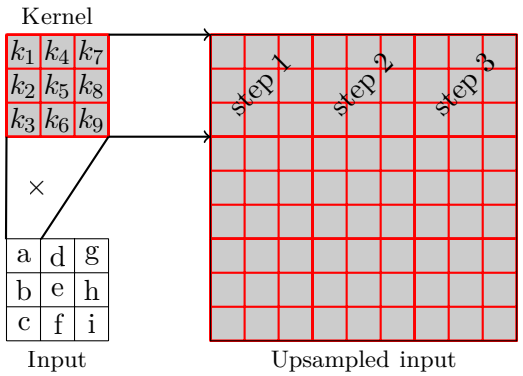

(b) Mechanism of a two-dimensional **three** strided transposed convolution over a 3×3 input matrix with a 3×3 kernel matrix. The resulting output upsampled by a factor of 3 is a 9×9 matrix. Three kernel locations on the output are indicated with step 1, step 2, and step 3. The extent of the kernel is identical to the stride width. Overlaps and checkerboard-like structures are avoided.

Figure 3.7: Visualization of the mechanism in transposed convolutional layers. Shown is pixelation, a common problem with transposed convolutional layers (a) and a possible solution, mitigating the pixelation effect.

methods, and first of all experience, practitioners find hyperparameters that work well [5]. As for this thesis, a discussion of the selection of hyperparameters for a fully-connected and a convolutional autoencoder is given in appendix A and appendix B respectively. In the following, the fully-connected autoencoder is named FCNN and the convolutional autoencoder is named CNN.

4 Model Order Reduction

This chapter introduces model order reduction (MOR) of the BGK-model in the Sod's shock tube, for which POD and in particular autoencoders are adopted to obtain a reduced basis (RB).
Model order reduction is a technique used for reducing the computational cost when evaluating PDEs [16][3][31]. To achieve this, the solution to a PDE is approximated by reducing one or more of its dimensions. The reduction performs a mapping onto a low-dimensional manifold. In this case the solution to the BGK model is a function $f(x, v, t) \in \mathbb{R}^3$. For example, v could be reduced to n, where k represents the number of elements in v and p represents the number of elements in n. With $p << k$ we obtain a reduced order model (ROM) which we call $q(x, n, t)$ of significantly lower dimension. In particular, n is called the reduced basis or the intrinsic variable. Chapter 2 shows that the BGK-model is a PDE which through discretization in the spatial dimension x and the velocity dimension v holds a system of KJ ODE's in time in 1D and K^3J^3 ODE's in time in 3D. By the reduction of v, we arrive at nJ ODE' in time for 1D and nJ^3 ODE's in time in 3D. This example illustrates the number of computations that can be saved by MOR. The mapping from $f(x, v, t)$ to $q(x, n, t)$ can be performed by one of the reduction algorithms from chapter 3. The remapping back to $\tilde{f}(x, v, t)$ is carried out by the same algorithm under the condition, that the distance $||f - \tilde{f}||$ is small.

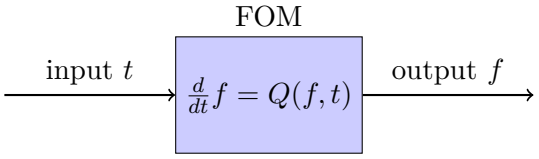

(a) Evolving the BGK model in Sod's shock tube in time is generated through evaluating the FOM in space x, velocity v and time t, which yields the solution $f(x, v, t)$. The operator Q is here the FOM described in chapter 2.

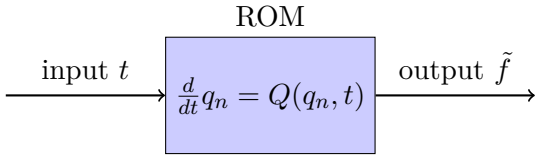

(b) Evolving the ROM of the BGK model in Sod's shock tube in time through evaluating the ROM at n and μ_i yields an approximation to the FOM solution $\tilde{f}$. The operator Q is here either POD or an autoencoder described in chapter 3.

Figure 4.1: Outline of the correlation between the FOM solution and the approximation obtained from the ROM.

To summarize, the idea that every high dimensional dynamical-state space W, also called solution manifold, can be mapped onto a state-space i.e. V of lower dimension, is exploited within MOR [31]. Thus, $f(x, v, t) \in W$ and $q(n, \mu_i) \in V$, where μ_i gives the variables omitted by the reduction and n the intrinsic variables. Again, p counts through the intrinsic variables. The state-space of the lower dimension is called the intrinsic solution manifold V with $q(n, \mu_i) \in V$[3]. MOR is partitioned into two successive phases called the *offline* - and the *online* phase. During the offline phase, experiments or simulations of the full order model (FOM) generate *snapshots* of a dynamical

system. The snapshots $F = \{f(t_1), ..., f(t_n)\}$ are created once, each representing one moment in time of the dynamical system. Thus a snapshot database of solutions $f(x, v, t)$ of the BKG model in Sod's shock tube is required. Next the mapping Q is constructed such that $\tilde{f} = Q(f)$, for which $f(t_i) \approx \tilde{f}(t_i)$, reducing the dimensionality of the FOM solution as outlined before. During the online phase, the reduced-order model is evaluated and the error is estimated by

$$\mathrm{L}_2 = \frac{||f - \tilde{f}||_2}{||f||_2} \tag{4.1}$$

which is called the relative L_2-Error norm. Note, the abbreviation L_2-Error is used from here on. Therefore the online phase may be described as a stage of independence from the full order model. Following [31] and [3], the success when building a ROM through linear reduction methods like the POD, depends on a rapidly decaying Kolmogorov N-width. In particular, advection-dominated problems exhibit a slow decay of the Kolmogorov N-width as described in [31], thus yielding the need for non-linear methods like autoencoders. The Kolmogorov N-width is given by

$$d_V(W) := \sup_{f \in W} \inf_{\tilde{f} \in V} ||f - \tilde{f}|| \tag{4.2}$$

and measures the worst best-approximation error for elements of W. The convergence behavior of the Kolmogorov N-width for advection-dominated problems, especially when jump conditions are involved as in Sod's shock tube, decays with

$$d_p(W) \leq \frac{1}{2} p^{-1/2}, \tag{4.3}$$

where p denotes the number of RB or intrinsic variables. Further insight is provided in [31].
Note, that hereafter the term intrinsic variables will be used solely. The relevance of using non-linear reduction methods for MOR is often formulated in terms of a slow decaying Kolmogorov N-width. And even though the BGK-model in Sod's shock tube describes an advection problem with jump discontinuities implies that linear reduction methods should fail, the following will show that this is only partly true for this case.

4.1 Offline phase and number of intrinsic variables

The FOM is the 1D BGK-model in Sod's shock tube for which solutions $f(x, v, t)$ for two levels of rarefaction are gratefully provided by Julian Köllermeier and the Departement of Mathematics at the RWTH Aachen.
One level with $Kn = 0.01$ is a slip flow as explained in [19]. The dilution up to this level is little. However, the boundary to view this flow as a continuum is reached, leading to inaccuracies when employing the common Navier Stokes equations. Still, the NFS-equations (Navier-Stokes-Fourier) could be used in addition to the BGK-model [18]. The solution with this level of rarefaction is hereafter referred to as **R**. The other solution is situated in the continuum flow regime with $Kn = 0.00001$, for which the Navier-Stokes equations can be utilized without hesitation. Hereafter, the solution for this flow will be referred to as **H**. A description of the BGK model and Sod's shock tube is available in chapter 2.
Note, that both **H** and **R** are three dimensional tensors comprising $f(x, v, t)$.
Sod's shock tube is discretized in space x with 100 nodes, in velocity v with 40 nodes for 25 time steps t, presented in table 4.1 and fig. 2.3.

Table 4.1: Problem setup for the BGK model in Sod's shock tube. The diaphragm is positioned at $x_d = 0.5025$. For the initial condition with $t = 0$ the gas is present at $x < x_d$ and absent for $x \geq x_d$.

Variable	Number of nodes i	Domain extension	Step size (uniform)
x	200	[0.0025,0.9975]	0.00499
v	40	[-10,10]	≈ 0.51282051
t	25	[0,0.12]	0.005

The reduction algorithms, introduced in chapter 3, require a distinct reshaping of the input data before they can be used. The preprocessed matrix for the FCNN as one batch $\mathrm{P_{FCNN}}$, is shown in eq. (4.4). Each row of $\mathrm{P_{FCNN}}$ represents $\mathrm{P_{FCNN},}_l = f(v, t_i, x_j)$, an example, that can be fed to the FCNN. Hence $x_j t_i = 5000$ samples can be acquired. POD can use $\mathrm{P_{FCNN}}$ as well as P_{FCNN}^T its transposition as input.
The preprocessed matrix for the CNN, $\mathrm{P_{CNN}}$, is shown in eq. (4.5) with $\mathrm{P_{CNN,}}_l = f(x, t, v_k)$. Hence $v_k = 40$ examples can be obtained to be fed into the CNN. Because of the little number of available examples per rarefaction level, it is decided to combine $\mathbf{H}$ and $\mathbf{R}$ to one dataset, yielding 80 available examples for training the CNN. This measure leads to one model, that potentially generalizes about the BGK model for a variety of rarefaction levels in Sod's shock tube. Details are presented in appendix B. Note, the following omits a distinction between $\mathrm{P_{CNN}}$ and $\mathrm{P_{FCNN}}$, when referring to the preprocessed matrices

$$\mathrm{P_{FCNN}} = \begin{bmatrix} f(v_1,t_1,x_1) & \cdots & f(v_n,t_1,x_1) \\ f(v_1,t_1,x_2) & \cdots & f(v_n,t_1,x_2) \\ \vdots & \vdots & \vdots \\ f(v_1,t_1,x_n) & \cdots & f(v_n,t_1,x_n) \\ f(v_1,t_2,x_1) & \cdots & f(v_n,t_2,x_1) \\ \vdots & \vdots & \vdots \\ f(v_1,t_n,x_n) & \cdots & f(v_n,t_n,x_n) \end{bmatrix}, \qquad \mathrm{P_{CNN}} = \begin{bmatrix} n_{Filters}, & f(v_1,\mathbf{t},\mathbf{x}) \\ n_{Filters}, & f(v_2,\mathbf{t},\mathbf{x}) \\ \vdots & \vdots \\ n_{Filters}, & f(v_n,\mathbf{t},\mathbf{x}) \end{bmatrix}. \tag{4.4, 4.5}$$

With the FOM solution at hand, it is possible to construct a mapping Q such that $Q(f) \approx \tilde{f}$. Again, for Q, POD and two autoencoders, the FCNN and the CNN are employed. With considering appendix A and appendix B, the selection of hyperparameters and training for the FCNN and the CNN is discussed, providing fully trained and tuned FCNNs and a CNN, which are given from now on.
Note that since this thesis focuses on the use of neural networks, POD acts as a benchmark. Consequently, to contrast the number p of intrinsic variables of the autoencoders (sizes of the code layer), POD will be utilized as a reference framework. The intrinsic variables obtained from POD, the FCNNs, and the CNN, will be referred to as $\mathbf{h}$ and $\mathbf{r}$, where the former describes the intrinsic variables when reducing $\mathbf{H}$ and the latter when reducing $\mathbf{R}$.
The first step is to perform a POD with $\mathbf{H}$ and $\mathbf{R}$ distinctively. The obtained singular values σ, as well as the cumulative energy (cusum-e) defined as

$$\text{cusum-e} = \frac{\text{cusum}}{\sum_i \sigma_i} \tag{4.6}$$

$$\text{with} \qquad (\text{cusum})_i = (\text{cusum})_{i-1} + \sigma_i \tag{4.7},$$

over the singular values, are shown in fig. 4.2. With a total of $p = 4$ intrinsic variables, a cumulative energy of over 99% can be achieved for **H**. The fourth singular value measures to a value of $\sigma_4 = 0.706$. The cumulative energy of the singular values of **R** arrives above 99% with $p = 6$ singular values. The sixth value is at $\sigma_6 = 0.275$. Thus a slight difference can be observed for both datasets when emplying POD.
The Kolmogorov N-width in eq. (4.2) linked to the decay of the singular values, invalidates the application of eq. (4.3) for the FOM solutions. The rate at which the singular values drop is approximately exponential in **H** and **R**. Consequently, a rapid decay of the Kolmogorov N-width is indicated. This supports the assumption, that advection and sharp shock fronts do not appear predominantly. The even though small, but dissimilar, decay rate of the singular values is a manifestation of the different rarefaction levels. With a decreasing number of particles present in Sod's shock tube, the lesser the probability of a single bulk macroscopic behavior emerges as seen in the full survey of the BGK model in chapter 2. Thus leading to an expected increase in the number of intrinsic variables necessary to achieve similar L_2-errors.

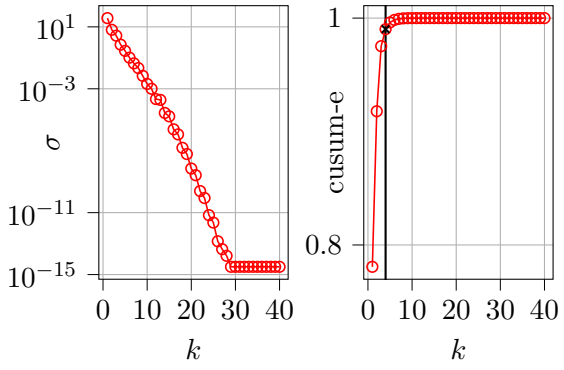

(a) Sigular values σ over k number of singular values (left) and cumulative energy, here labeled as „cusum-e“ over k (right) for **H**. A black cross marker corresponds to over 99% cumulative energy.

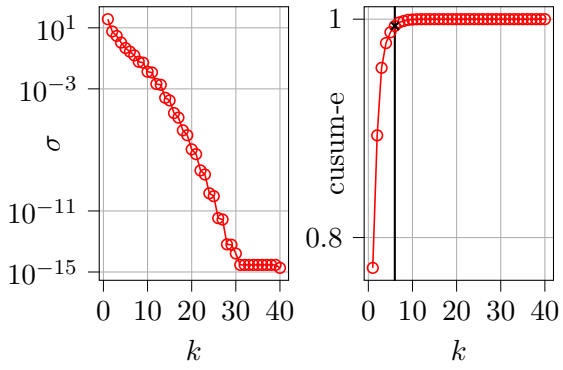

(b) Sigular values σ over k number of singular values (left) and cumulative energy, here labeled as „cusum-e“ over k (right) for **R**. A black cross marker corresponds to over 99% cumulative energy.

Figure 4.2: Comparison of singular variables σ and cumulative energy for **H** and **R**. The decay of the singular values can be used to estimate the decay of the Kolmogorov n-width.

From a fluid mechanical point of view, the number of intrinsic variables for **H** in theory suffices with $p = 3$, as a slip-flow can be described in terms of three macroscopic quantities i.e. density ρ, macroscopic velocity u and total energy E_{tot} as in eq. (2.11) to eq. (2.13) and in [1][16]. As mentioned previously, requires **R** a larger number for p because more than a single Maxwellian describes the microscopic velocities. Therefore, **h** with $p = 3$ is employed for the FCNN as a starting value for the hyperparameter search. A starting value of $p = 5$ on the other hand is chosen for **r**. Note that this implies, that the CNN, which is trained with both rarefaction levels simultaneously, initially uses $p = 5$. The same value for p is chosen for the FCNN and **R**.
The following variation of p, sheds light on the performance of the autoencoders with different bottleneck layer sizes.
To this end, p is varied for POD, the FCNNs and the CNN over $p \in \{1, 2, 4, 8, 16, 32\}$ for both rarefaction levels. Note that the neural networks are trained again for these experiments. By

changing p i.e. widening the bottleneck layer, a gain or loss of capacity occurs that can be connected to stability during training, see chapter 3 and [5]. Shown in fig. 4.3 is the outcome of said

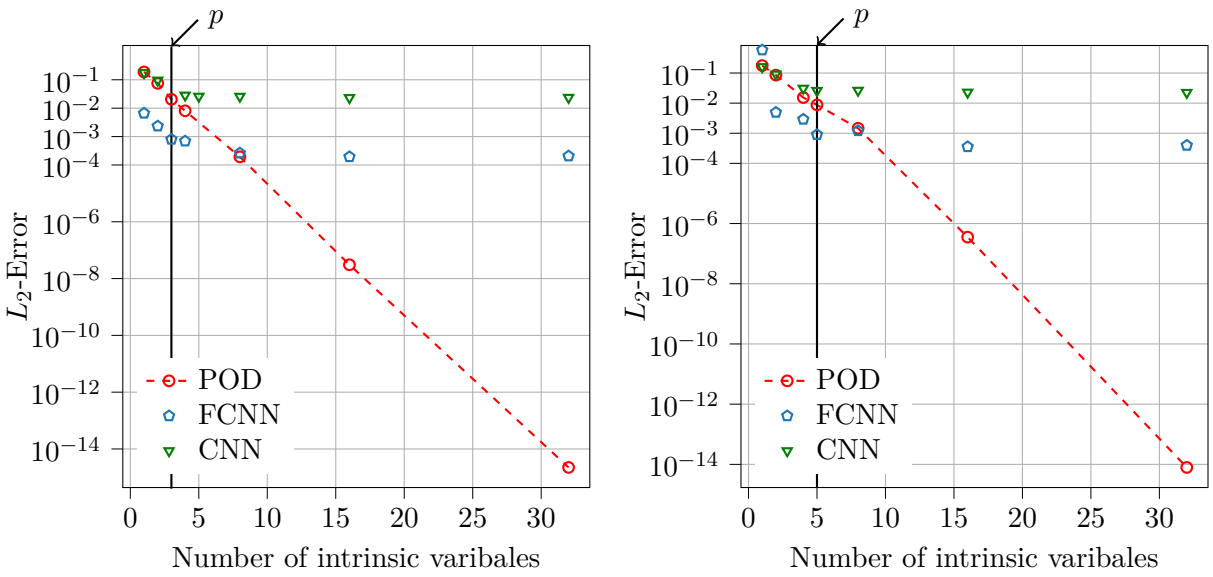

Figure 4.3: The L_2-Error over the variation of p, the number of intrinsic variables using POD, the FCNNs and, the CNN. Results for **H** are displayed on the left and for **R** on the right.

experiments. The design for fig. 4.3 is taken from [3]. The loss of information when applying POD goes exponentially to zero with increasing p which is not surprising when consulting the *Eckard-Young Theorem* provided in eq. (3.4) taken from [23]. The left plot of fig. 4.3 displays the results for **H** with $p = 3$, the estimated size of **h**, emphasized with a black line. The L_2-error of the FCNN first drops until $p = 3$ reaching $L_2 = 0.0008$ to then drop further until $p = 8$ with $L_2 = 0.00026$. Afterwards the L_2 stagnates with a best value of $L_2 = 0.00019$ at $p = 16$. Interestingly, the biggest improvement can be observed until $p = 3$.
The L_2-error of the CNN, that was trained with both rarefaction levels, drops until $p = 4$ reaching $L_2 = 0.028$. Afterwards, the L_2-error stagnates reaching it's best value of $L_2 = 0.023$ at $p = 16$ and $p = 32$. It is assumed that the value of the L_2-error is approximately the same for $p = 3$ and $p = 4$, as it is for the FCNN. Therefore, the CNN as well as the FCNN, seem to reflect the assumptions for p considering **H**. While the CNN and POD are congruent for $p = 1$ and $p = 2$ with POD outperforming the CNN afterward, the FCNN is only outperformed by POD after $p = 8$, where the L_2-error of both algorithms meet.
Moving forward, to assess the value of p for **R**, consider the right plot of fig. 4.3. Once again, $p = 5$ is highlited with a black line to indicate it's assumed value. The L_2-Error of the FCNN begins as the highest of all three algorithms with $L_2 = 0.58$ at $p = 1$. Afterwards the L_2-error plummets outperforming POD and the CNN until $p = 8$. After $p = 8$, where POD and the FCNN meet with $L_2 = 0.012$ and $L_2 = 0.014$ respectively, POD outperforms both algorithms. From $p = 4$ to $p = 5$ the L_2-error of the FCNN drops from $L_2 = 0.0029$ to $L_2 = 0.0009$. The increase in L_2-error moving from $p = 5$ to $p = 8$ is not a result of overfitting as seen in appendix B, and therefore can only be explained with a bad initialization point of the networks free parameters θ. A continued widening of the bottleneck layer results in the lowest error of $L_2 = 0.00035$ at $p = 16$ for the FCNN.
Resulting L_2-error values of POD and the CNN match for $p = 1$ and $p = 2$. Thereafter, the error

drops to $L_2 = 0.03$ and $L_2 = 0.026$ for $p = 4$ and $p = 5$ respectively. Continuing to widen the bottleneck layer, it can be observed that the L_2-error stagnates. Nevertheless, the lowest error is reached with $L_2 = 0.022$ at $p = 16$ and $p = 32$.
The variation of p shows that for the assumed values of $p = 3$ and $p = 5$, the FCNN outperforms POD. Additionally, the performance of both autoencoders increases up to those points, which accentuates the previously made assumptions for p. Nonetheless, those are not the lowest values the FCNN, and with some limitations also the CNN can reach. Until $p = 8$ the FCNN reaches its limitations for surpassing POD. Therefore, depending on p, either POD or the FCNN can surpass each other. In order to evaluate the interpretability of all three algorithms, $p = 3$ and $p = 5$ is chosen for sizes of $\mathbf{h}$ and $\mathbf{r}$ respectively.

The following chapter covers the discussion of results obtained from POD, the FCNN, and the CNN. Additionally, the evaluation of new states of the FOM is offered, which can be viewed as the online phase of MOR.

5 Results

This chapter covers the evaluation of reconstructions $\tilde{f}$ obtained from the FCNNs and the CNN through a comparison against reconstructions obtained from POD. Additionally, an analysis of the interpretability of the intrinsic variables **h** and **r** is provided. This chapter concludes with the attempt to create new states of the FOM with the FCNN, which can be viewed as an online phase of MOR.

The benchmarking of POD and neural networks begins with a contrast of the number of parameters to obtain $\tilde{f}$. Beforehand, solely the number of trainable parameters that compose both neural networks were called θ. For this comparison, θ is extended and includes all elements of the left and right singular vectors as well as the singular values of POD. Additionally, the amount of intrinsic variables used for reconstruction is set to $p = 3$ and $p = 5$ for **H** and **R** respectively. An exception is the CNN which uses $p = 5$ independently from rarefaction level. A summary is provided in table 5.1.

POD uses 15129 and 25225 parameters to reconstruct **H** and **R** respectively. This is the largest

Table 5.1: Amount of parameters θ used to reconstruct f, the number of intrinsic variables p and the corresponding L_2-Error for POD, the FCNNs, and the CNN.

Algorithm	Parameters θ		Int. variables p		L_2-Error	
	H	**R**	**H**	**R**	**H**	**R**
POD	15129	25225	3	5	0.0205	0.0087
FCNN	2683	3725	3	5	0.0008	0.0009
CNN	8246	8246	5	5	0.025	0.027

amount of parameters of all three algorithms, which yield L_2-errors of 0.0205 and 0.0087 respectively. Interestingly, the elevation of p amounts to an increase of parameters by approximately 1.7, which is comparable to the FCNN with an approximate increase of 1.4. The FCNN, which holds the best L_2-errors of 0.0008 and 0.0009 for **H** and **R** respectively, does so with the least amount of parameters. For reconstructing **H** solely 2683 and for the reconstruction of **R** solely 3725 parameters are used, which is a fraction of the need for POD. The second most populous algorithm is the CNN, which uses 8246 parameters for both rarefaction levels. The resulting L_2-errors with 0.025 for **H** and 0.027 for **R** are the largest of all three algorithms.

Next, a qualitative analysis with actual reconstructions is presented. For this purpose the L_2-error over time t, seen in fig. 5.1, is used to localize the most challenging snapshot for each algorithm.

With POD and the CNN the last timestep, at $t = 0.12s$, for both rarefaction levels is the most rich in the $L2$-Error. In contrast, the FCNN does not show a distinct time dependence of the

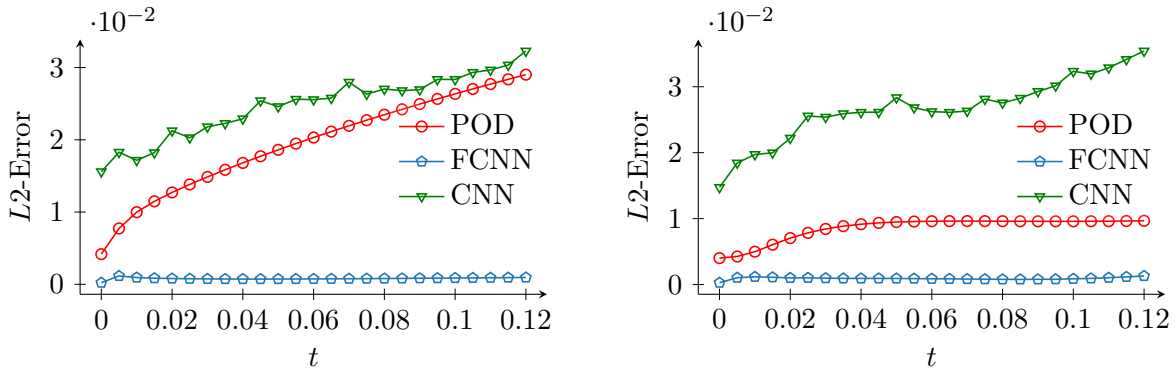

Figure 5.1: L_2-error over time for POD, the FCNNs, and the CNN. Results for **H** are displayed on the left, the results for **R** are displayed on the right.

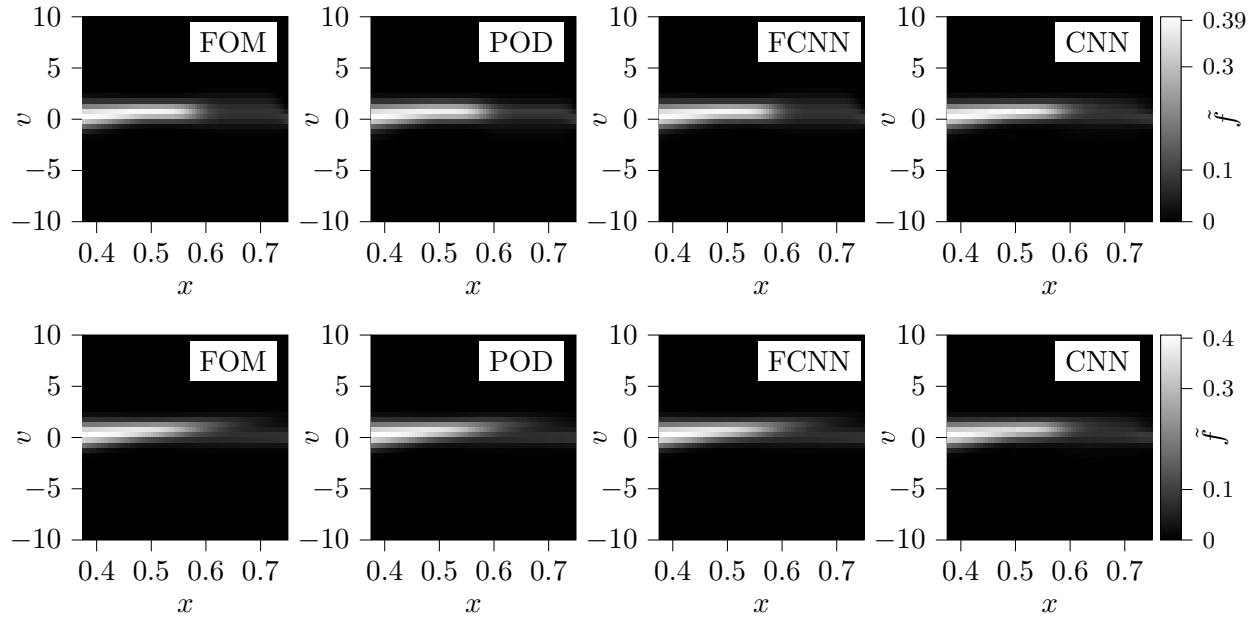

Figure 5.2: Comparison of the FOM solutions f with three reconstructions $\tilde{f}$ obtained from POD, the FCNNs and the CNN. Reconstrucions are shown at $t = 0.12s$ for $x \in [0.375, 0.75]$. The top row displays case **H**, bottom row displays case **R**. The colobars reference f and $\tilde{f}$.

L_2-error. Nonetheless, struggles at the onset at around $t = 0.005s$ with **H** and around $t = 0.005s$ and $t = 0.0115$ (in the beginning and at the end) with **R** can be observed for the FCNN. Examples of reconstructions $\tilde{f}(x, v, t_i)$ with $t_i = 0.12s$ and $x \in [0.375, 0.75]$ are given in fig. 5.2.

The FOM solution viewed as $f(x, v, t_i)$ has been introduced in chapter 2. There, $f(x_j, v, t_i)$ is the probability distribution of the microscopic velocities v at point x_j in space at one moment t_i in time for a gas. With this in mind, a qualitative comparison between the three algorithms is made, considering the rendition of the velocity probabilities. Starting with **H**, seen in the top row of fig. 5.2 it can be observed that $\tilde{f}(x, v, t_i)$ starting around $x = 0.6$ gets defective for POD and the CNN. Noteworthy, here the probability distribution is thinner than the original with POD. This in

turn leads to errors in the temperature T once passing $x \approx 0.6$. Prominent qualitative deviations using the CNN are especially blurriness/pixelation of $\tilde{f}(x, v, t_i)$ after $x \approx 0.6$. In contrast, the FCNN seems to reproduce the FOM solution almost exactly.
Continuing with a row further down in fig. 5.2 and therefore with **R**. The FCNN seems to reproduce the FOM solution without any visible drawback. POD also seems to reproduce all important structures, except after $x \approx 0.7$ around the contact discontinuity, some values for velocities with $v > 0$ appear to be missing. Again, the CNN struggles with blurriness making $\tilde{f}$ for both rarefaction levels look largely similar.

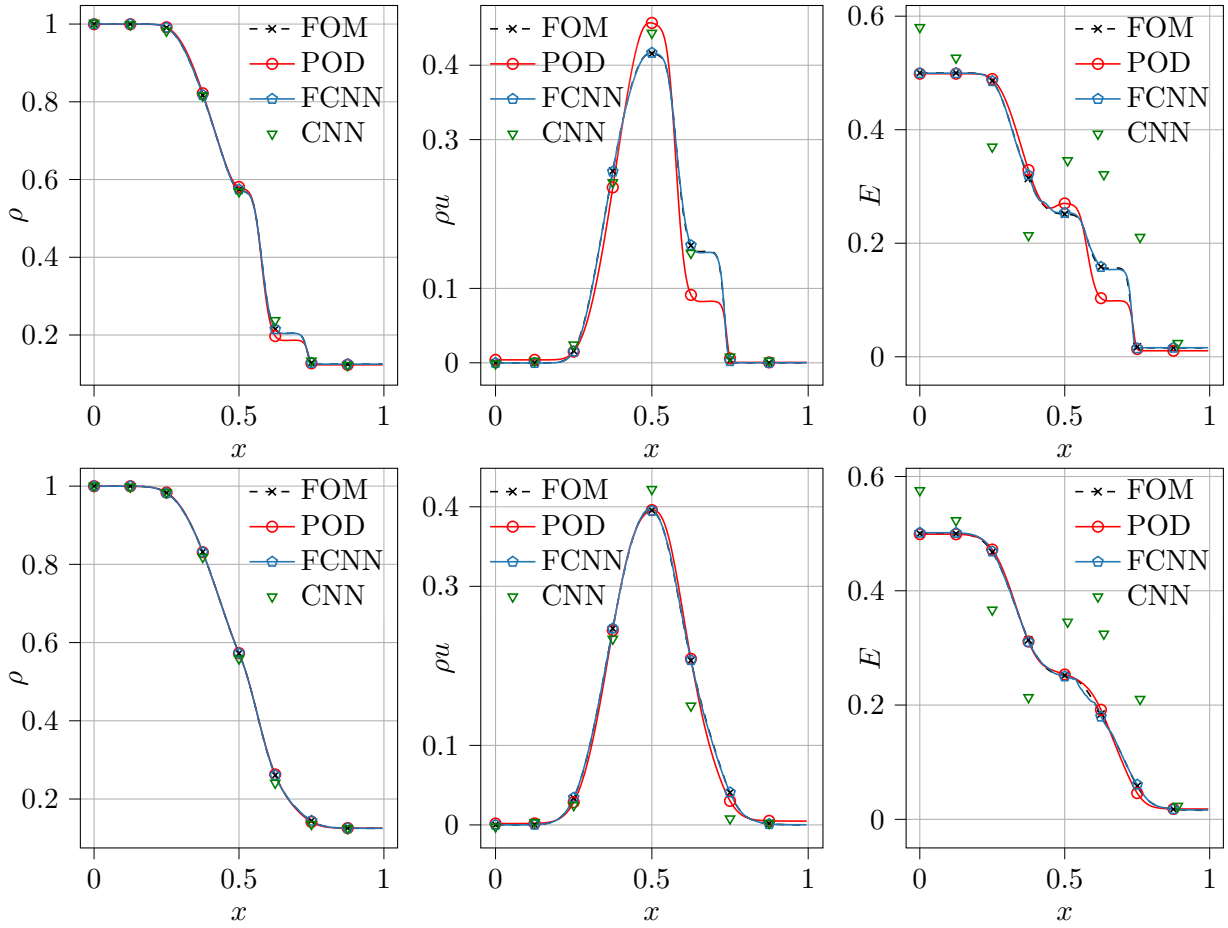

Figure 5.3: Matching of macroscopic quantities ρ, ρu and E reproduced by POD, the FCNNs the and CNN with macroscopic quantities computed from the FOM. Top row shows results for **H**, bottom row for **R** at time $t_i = 0.12s$. The CNN is displayed with marks only because of trembles in the signal.

Loss of information described above can unfold in severe mistakes in ρ, ρu and E, the macroscopic quantities, as displayed in fig. 5.3. Examining the macroscopic quantities enables a detailed look at the reconstruction errors. Features of the macroscopic quantities are discussed in terms of rarefaction wave, contact discontinuity, and height as well as the position of the shockfront. For a detailed elaboration of these terms see chapter 2. Following the structure in the preceding figures, macroscopic quantities of **H** are displayed in the top row and for **R** in the bottom row of fig. 5.3. Firstly, the reproduction of the macroscopic quantities ρ, and ρu obtained by the FCNN match

the FOM solution exact for both levels of rarefaction **H** and **R**. Interestingly, despite the overall impressive performance of the FCNN regarding the small number of parameters it uses, the total energy shows small deviations around the tail of the rarefaction wave for **H** and somewhat severe errors at the transition from rarefaction wave to shock front for **R**. Secondly, the CNN produces trembles in ρu and especially in E which is why it's shown with marks only. The macroscopic quantities reproduced by the CNN show, its inability to differentiate between **H** and **R**. Specifically, the macroscopic quantities for **R** appear to be a copy of the ones for **H**. Additionally, considering **H**, it can be observed, that the momentum ρu holds small errors for the tail of the rarefaction wave as well as the contact discontinuity. The value for the tip of the shockwave exceeds, comparable with POD, the exact solution. Thirdly POD performs better on **R**, which is unsurprising considering the difference in the number of used parameters, holding only small deviations of the contact discontinuity and the shockwave for the momentum ρu and the total energy E. The density ρ matches the FOM solution exact. Pronounced deviations from the FOM solution occur using POD on **H**. The density ρ undercuts the original shockwave. The momentum ρu heavily exceeds the tail of the rarefaction wave and to the same extent undercuts the contact discontinuity. Thus, in the total energy E, the same is observable for the tail of the rarefaction wave and the contact discontinuity.

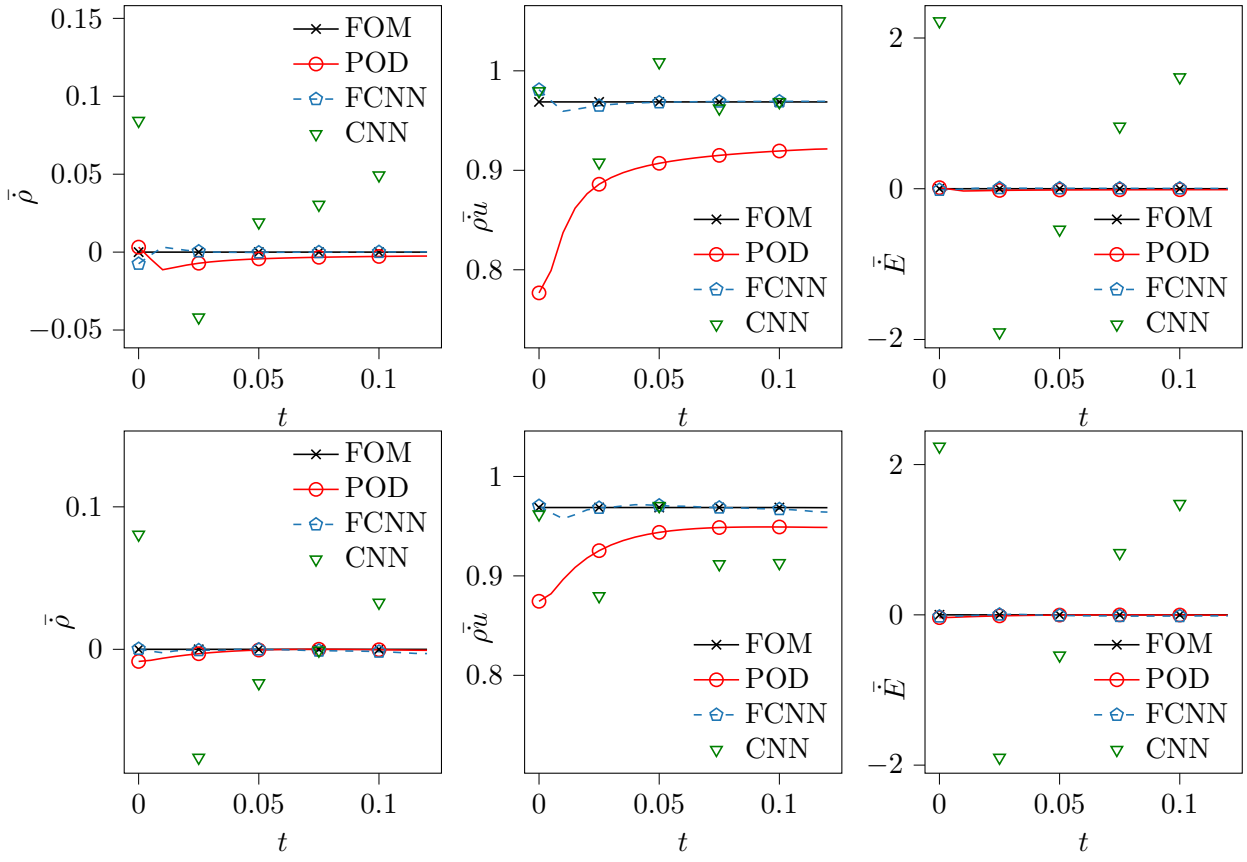

Figure 5.4: Comparison of the conservative properties of reconstructions obtained from POD, the FCNNs, and the CNN against the conservative properties of the FOM solution using the temporal mean.

The physical consistency of $\tilde{f}$, in terms of conservation of mass momentum and energy, is a critical criterion for its validity. Hence, conservation properties are analyzed in the following. In that respect, the temporal mean over the time derivative, which can be calculated exemplary for ρ with

$$\frac{\mathrm{d}}{\mathrm{d}t}\int \rho(x,t)\,\mathrm{d}x\Delta t = \bar{\dot{\rho}}, \tag{5.1}$$

of the macroscopic quantities is employed. Figure 5.4 shows the conservation of mass, momentum, and total energy as a temporal mean for **H** in the top row and **R** in the bottom row.
Conservation of mass is met using the FCNN, except for small deviations at the outset for both cases **H** and **R**. Similarly, POD meets conservation of mass for **R**. The erroneous **H** case losses mass at the onset and gains mass towards the end with POD. Conservation of momentum meets the FOM solution, except for minor gains and loses, after $t \approx 0.03s$ using the FCNN for both cases **H** and **R**. POD gains momentum of 0.13 for **H** and 0.07 for **R**. The conservation of total energy is met for **H** and **R** using POD and the FCNN. Finally, the reconstructions of the CNN do not conserve mass, momentum nor total energy. All conservative properties behave comparable to a sawtooth wave. A gain and loss of either of the quantities can be observed.

Because of the black-box nature of neural networks, the question of interpretability often arises when working with them [32]. Especially benchmarking neural networks for model order reduction with POD asks for evaluating the interpretability of the intrinsic variables. Owing to the tremendous quality of POD, which lies in "the physically interpretable decomposition"[23][p.375] of the input data, as stated in chapter 3.
Following the deduction, that **H** can be completely described in terms of three macroscopic quantities and that **R** is describable in a similar way, it is put to test if the intrinsic variables **h** and **r** show any similarities, if not match any macroscopic quantity. To this end, two supplementary macroscopic quantities, namely the temperature T and macroscopic velocity u, are added to the three macroscopic variables. In fig. 5.5 and fig. 5.6, these are depicted first over the whole domain of x and t and for two specific timesteps $t = 0.055s$ and $t = 0.12s$ for **H** and **R** respectively. Similarily are the intrinsic variables **h** and **r** with

$$[h_0(x,t),\ldots,h_p(x,t)] = \mathbf{h} \tag{5.2}$$

and

$$[r_0(x,t),\ldots,r_p(x,t)] = \mathbf{r} \tag{5.3},$$

depicted in fig. 5.7 and fig. 5.8 respectively.
Strikingly, most intrinsic variables appear to be a sort of linear combination of the five intrinsic variables. In particular **h**. For example, the rarefaction wave, shock wave, and contact discontinuity, which can be identified in h_0 reflect a combination of those found in the density ρ and the total energy E. Furthermore, h_1 seems to be a mirror image of the momentum ρu, where beginning end values are inspired by the temperature T. Then again, T plays a more pronounced role in h_2, where its fluctuation appears. The peak of h_2 could be guessed from the peak of the macroscopic velocity u with its bump at $t = 0.12$.
A clear identification of macroscopic quantities that can be seen in **r** is possible for r_3, which reflects the shape of the density ρ. Moreover, the peak of the velocity u can be rediscovered in the through of r_0. For other intrinsic variables of **r** namely r_1, r_2 and r_3 a clear discernability of macroscopic quantities is not observed. It seems rather that those constitute abstract information about the rarefied flow. Nonetheless, it can't be verified, that their creation through linear combinations is impossible.

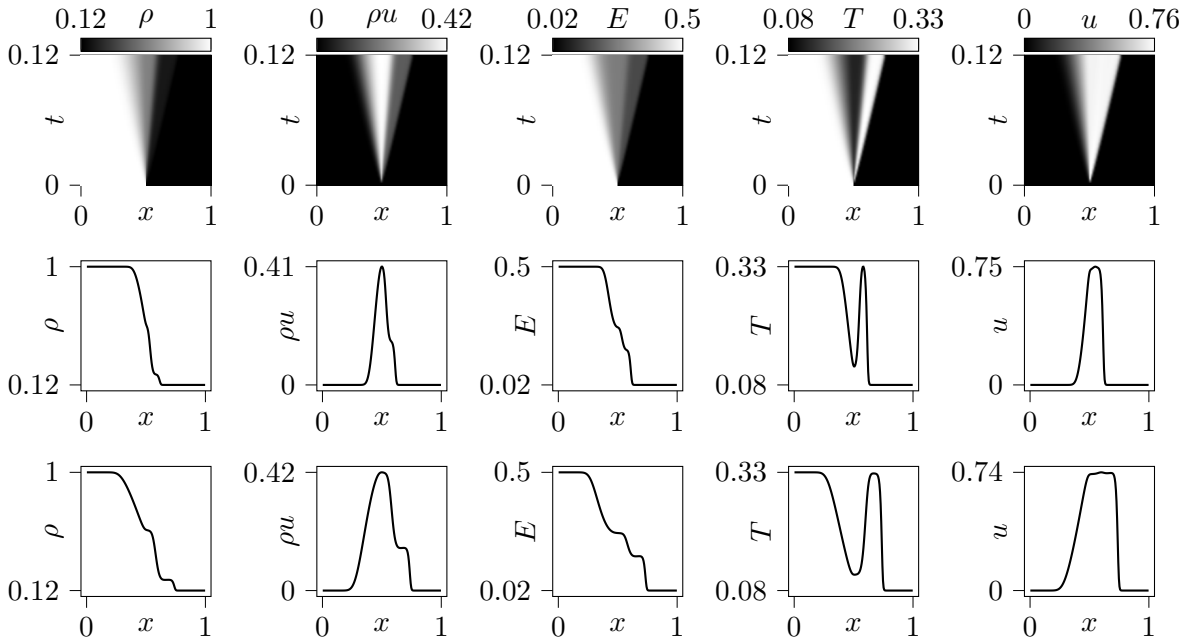

Figure 5.5: Macroscopic quantities of **H**. Density ρ, momentum ρu, total energy E, teperature T and velocity u over time t and space x in the top row and specifically at $t_i = 0.055s$ and $t_i = 0.12$ in the middle and bottom row respectively.

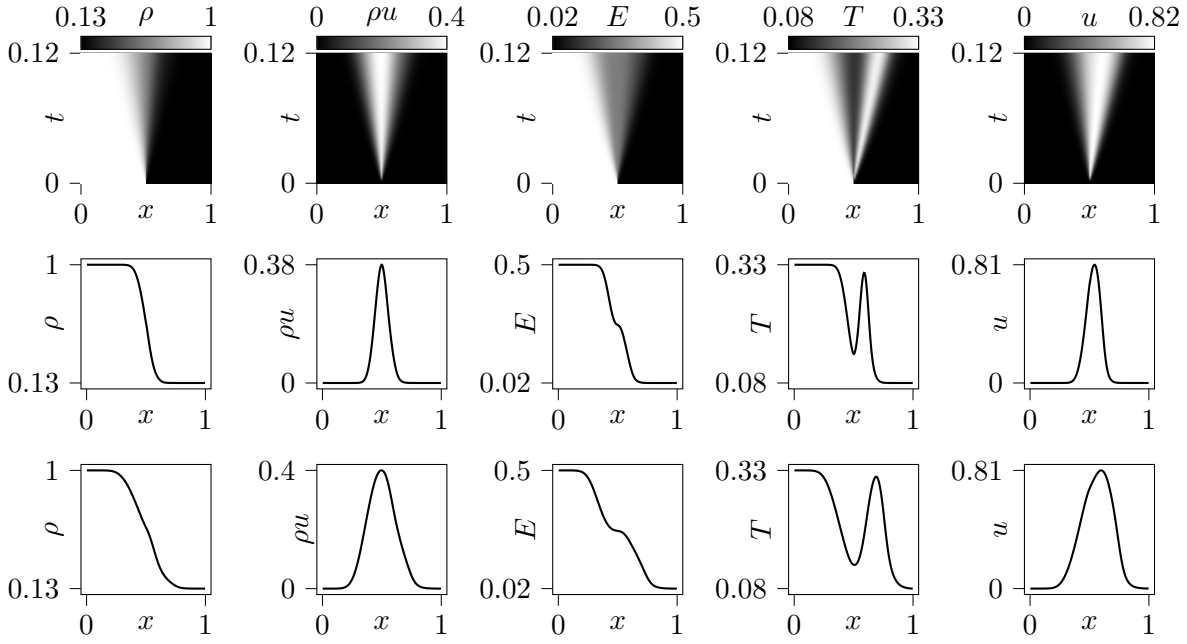

Figure 5.6: Macroscopic quantities of **R**. Density ρ, momentum ρu, total energy E, teperature T and velocity u over time t and space x in the top row and specifically at $t_i = 0.055s$ and $t_i = 0.12$ in the middle and bottom row respectively.

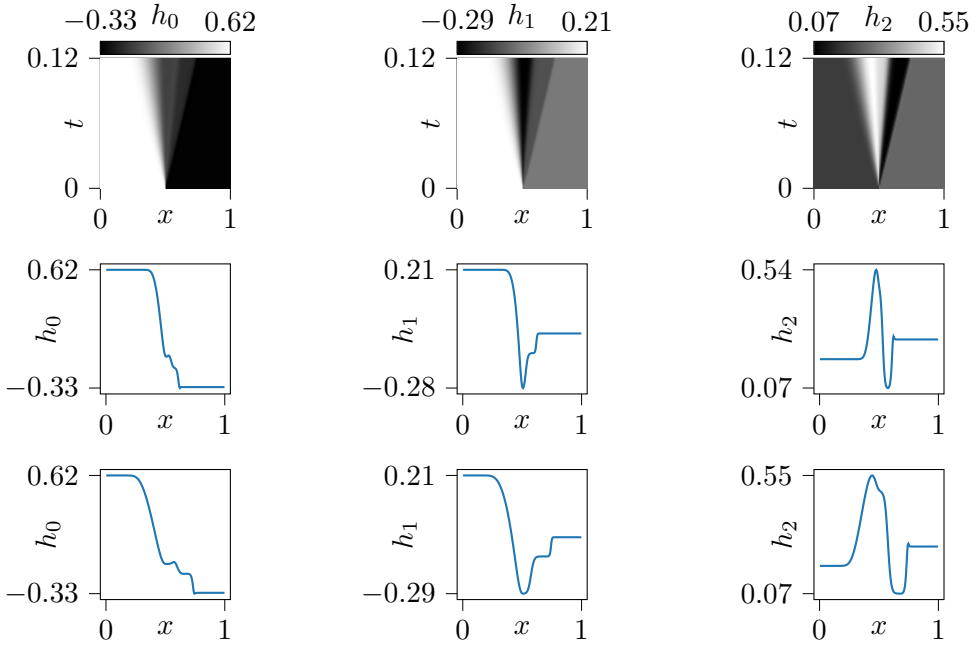

Figure 5.7: Intrinsic variables $h_0(x,t)$, $h_1(x,t)$ and $h_2(x,t)$ of $\mathbf{h}$ obtained from the FCNN. Top row depicts $\mathbf{h}$ over the whole (x,t) domain, middle and bottom row for $t = 0.055$ and $t = 0.12$ respectively.

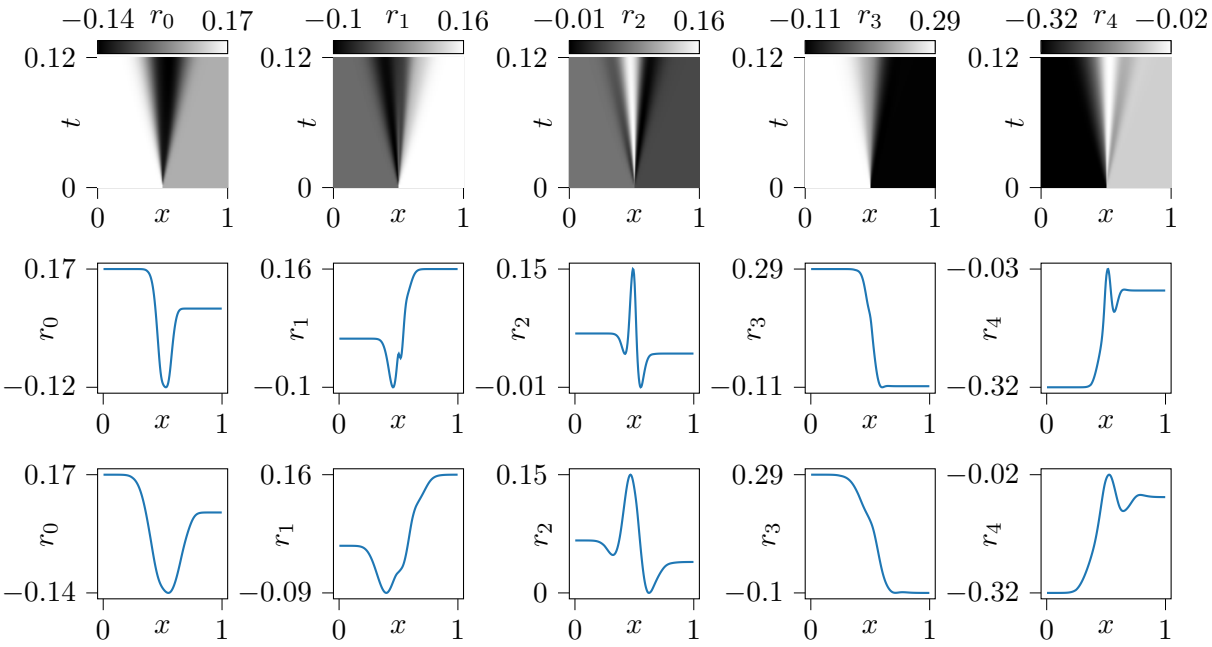

Figure 5.8: Intrinsic variables $r_0(x,t)$, $r_1(x,t)$, $r_2(x,t)$, $r_3(x,t)$ and $r_4(x,t)$ of $\mathbf{r}$ obtained from the FCNN. Top row depicts $\mathbf{r}$ over the whole (x,t) domain, middle and bottom row for $t = 0.055$ and $t = 0.12$ respectively.

The intrinsic variables extracted from the CNN and POD are shown in fig. 5.9. They are only dependent on v with

$$[h_1(v), \ldots, h_p(v)] = \mathbf{h} \qquad (5.4) \qquad \text{and} \quad [r_n(v), \ldots, r_p(v)] = \mathbf{r} \qquad (5.5)\cdot$$

The third and fourth row of fig. 5.9 show the first three and five POD modes of $\mathbf{H}$ and $\mathbf{R}$ respectively. As expected, the first three modes of both rarefaction levels do not differ significantly. Equally, the bulk dynamic answer of the two gas flows to the test case doesn't. Pronounced differences of $\mathbf{h}$ and $\mathbf{r}$ extracted from the CNN, seen in the first and second row of fig. 5.9, are also not observed. This aligns with previous findings that the CNN fails to differentiate between $\mathbf{H}$ and $\mathbf{R}$. Qualitatively, the intrinsic variables of the CNN show less complexity compared to those of POD. Nonetheless, a rough analogy between the two can be observed. Especially h_0 and r_0, the first intrinsic variables of the CNN, resemble those of POD. Furthermore, a small through in h_1 and r_1 of the CNN can be identified. This through, though much more pronounced, is also present in h_1 and r_1 of POD. Worth mentioning is that h_0 and r_0, h_1 and r_1 as well as h_4 and r_4 of the CNN encompass the largest peaking of all intrinsic variables.

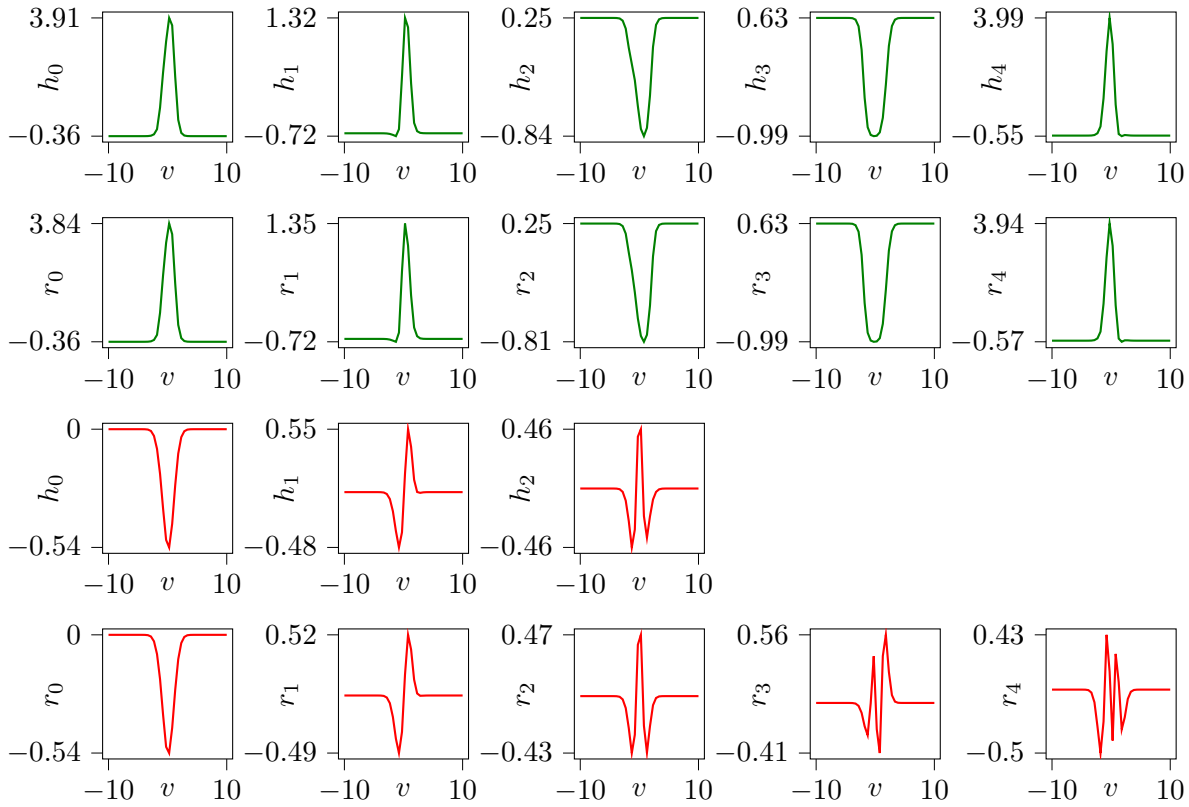

Figure 5.9: Intrinsic variables $h_0(v)$, $h_1(v)$, $h_2(v)$, $h_3(v)$ and $h_4(v)$ of $\mathbf{h}$ in the top row and $r_0(v)$, $r_1(v)$, $r_2(v)$, $r_3(v)$ and $r_4(v)$ of $\mathbf{r}$ of in the second row extracted from the CNN. Third and fourth row show $h_0(v)$, $h_1(v)$, $h_2(v)$ of $\mathbf{h}$ and $r_0(v)$, $r_1(v)$, $r_2(v)$, $r_3(v)$ and $r_4(v)$ of $\mathbf{r}$ extracted from POD respectively.

Usually, POD within a Galerkin framework exploits the intrinsic variables as in [16] to produce new states. The same is possible with the intrinsic variables obtained from autoencoders as in

[3]. Both won't be discussed in this contribution. Rather, new states are obtained by performing an interpolation in time t of $\mathbf{h}$ and $\mathbf{r}$. This approach tests a different kind of ability to generalize about the FOM solution. So far there have been two kinds of generalization tested: The first can be encountered during training, where a split into train- and validation set, probes the ability to fit unseen examples. A second approach to generalization is tried with the CNN, where both rarefaction levels as training examples probe the ability to fit both in the same model. The third insight into the ability to generalize is tested using the FCNN. By the temporal interpolation in the intrinsic variables, it is probed if new states can be generated that meet the condition of MOR that the distance $||f - \tilde{f}||$ is small.
For this thesis, an additional solution $\mathbf{H}^*$ of the BGK model in Sod's shock tube with $Kn = 0.00001$ is provided with a temporal resolution of 241 snapshots. This resolution is 9.64 times finer than the original one. Hence, an interpolation using cubic splines in the temporal axis of $\mathbf{h}$ is performed, thus resulting in intrinsic variables called $\mathbf{h}^*$. The temporal resolution $\mathbf{h}^*$ is as well 241 and fed into the decoder of the FCNN generating $\widetilde{\mathbf{H}}^*$. A comparison of $\mathbf{H}^*$ against $\widetilde{\mathbf{H}}^*$ as truth against prediction in terms of macroscopic quantities density ρ, momentum ρu and total energy E is provided in fig. 5.10.

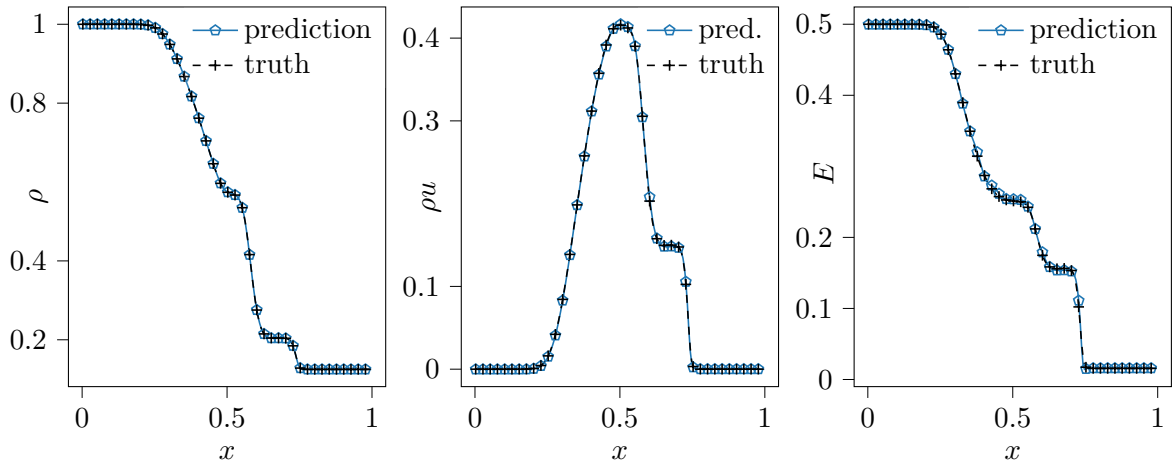

Figure 5.10: Macroscopic quantities density ρ, momentum ρu and total Energy E, displayed in this order, at time $t = 0.12$ against predictions generated from interpolation. Temporal interpolation with cubic splines is performed in $\mathbf{h}$ from 25 snapshots to 241 snapshots.

The generated snapshots match the macroscopic quantities almost exactly, similar to the results obtained without interpolation. Nonetheless, the resulting L_2-error for $\widetilde{\mathbf{H}}^*$ increases to $L_2 = 0.0012$, which is 1.5 times higher than the original L_2-error.

In summary, the reconstructions obtained from the CNN do not meet conservation of mass, momentum, and total energy, which devalues their physical applicableness. Nonetheless, the CNN uses with 8246, the second-highest amount of parameters. The attempt to learn both levels of rarefaction with the CNN subsequently also failed. Specifically, the CNN reconstructs $\mathbf{H}$ from $\mathbf{R}$ as input. In addition, the intrinsic variables of the CNN show, to some degree, similarities to POD basis modes.
The FCNN uses with 2683 to 3725 parameters the least amount, while achieving the lowest L_2-error in the range of 8×10^{-4} to 9×10^{-4}. At the same time for $\mathbf{H}$, fewer parameters than for $\mathbf{R}$ are

needed to achieve comparable results using the FCNN. Conservation of mass momentum and total energy is met, hence macroscopic quantities of considerable accuracy can be obtained which show a good fit to the FOM solution's. The question of the interpretability of the intrinsic variables is up to discussion owing to their entangled nature, especially for $\mathbf{R}$. Generalization was successfully tested, by generating new snapshots of $\mathbf{H}$ but at the same time increasing the L_2-error to 1.2×10^{-3}.
Both neural networks are tested against POD. By fixing p the algorithm is artificially limited and performs under its abilities. However, POD uses with this adjustment five to six times more parameters than the FCNN. Its deterministic character enables POD to achieve any possible accuracy, which was not observed with the neural networks.

5.0.1 Discussion and Outlook

An interesting finding during the hyperparameters search is the different number of parameters, that the FCNN requires to achieve comparable results for the slip- and the continuum flow. The continuum flow requires 1.4 times fewer parameters compared to the rarefied flow. To recap, a continuum flow can be described in terms of three macroscopic quantities, a rarefied flow is described as a probability distribution of the macroscopic velocities of all involved particles. In turn, the necessity of using more parameters for the rarefied flow arises. This can be interpreted as a validation of the FCNN, as physical properties are reflected.
POD and the FCNN have different qualities. With the setting described above, POD uses up to 6.7 times more parameters than the FCNN for the given reconstruction losses. This suggests, that the quality of the parameters, that the FCNN has learned surpasses those of POD. On the other hand, the FCNN shows to be limited in terms of reconstruction loss that can be achieved. Therefore, the applicability of either of the methods for MOR can eventually be decided by the use case. Whenever computational resources like available memory are scarce, then the FCNN would be the method of choice. In other cases where reconstruction loss needs to be below that of the FCNN and computational resources are not limited, POD would be the preferred method.
Why was the training of the CNN not successful, even though it could benefit from using more parameters compared to the FCNN? Convolutional layers comprise sparsity through local connectivity of nodes as explained in [5]. This in turn yields a regulative effect. Additionally, convolutional layers have more hyperparameters that can be tuned than fully connected layers. This can make it harder to find the right set of hyperparameters for convolutional neural networks. Furthermore, the CNN could feed on much fewer examples of the flows, considering 5000 examples for the FCNN versus 40 per flow for the CNN. This effect was tried to compensate through data augmentation methods but did not yield any improvement. Those three driving factors, the intrinsic regulative effect of convolutional layers, unfit hyperparameters, and data scarcity are thought to be responsible for the performance of the CNN.
These considerations raise the question of the optimality of hyperparameters for both neural networks. It is unknown if both neural networks reached an optimal local minimum of the cost function. Hence the continued search for hyperparameters is left to future works. For example, both neural networks are intentionally kept small enough to not overfit. Therefore, it is possible to raise the capacity of both networks and letting them intentionally overfit, to then use regularizing methods as e.g. weight decay or dropout, to decrease the generalization gap. Both methods enable for a flexible adjustment of capacity, that, to some extend, is learned by the network. An important hyperparameter, that has been left out during the hyperparameter search, is the loss function. Ultimately the loss function determines what is considered as a good solution and what is not. The

binary cross-entropy loss with logits from `pyTorch` could be used as an alternative. Promising are also physically inspired considerations, like a loss function that includes the conservation of mass, momentum, and energy.
Furthermore, it is proposed, to test LSTM (long short term memory) cells or similar GRUs (gated recurrent units) in an encoder-decoder configuration against projection methods like the Galerkin projection, in evolving the intrinsic variables in time. Additionally, could the variational autoencoder (VAE) or the Wasserstein autoencoder (WAE) be used to generate disentangled intrinsic variables. In this regard, it is as well proposed to explore the possibility of the existence of a linear system of equations that entangles the intrinsic variables found in this thesis. Finally, methods from natural language translation like transformer models introduced to rarefied gas dynamics could be applied to translate flows of differing levels of rarefaction into each other.

Appendix

A Hyperparameters for the Fully Connected Autoencoder

The finding of appropriate hyperparameters for the fully-connected autoencoder is described here. The hyperparameters include the number of layers i.e. depth, number of nodes per hidden layer i.e. width, batch size and non-linear activation functions, number of epochs for training, and the learning rate. Experiments are evaluated through the validation error which estimates the model's ability to generalize, the training error which estimates the optimization to training data, and the L_2-error as described in chapter 4. Both validation- and training error are described in chapter 3 and provide information about under- and overfitting. Moreover, the validation error is the essential metric for validating a model's performance. The L_2-error, on the other hand, gives an estimate of how well the model performs on the whole dataset hence is applied as a comparative metric against POD.
To start with a working model, an estimate over the initial hyperparameters is done, which are summarized in Table A.1. These include a mini-batch size of 16, the width of the bottleneck layer is 3 and 5 for **H** and **R** respectively and a learning rate of 0.0001. LeakyReLU is applied for the output, input, and any hidden layer besides the output of the bottleneck layer, and is referred to as activation hidden. Tanh is applied for the output of the last hidden layer in the encoder which outputs the code, referred to as activation code. A visualization of the activation scheme is provided in fig. A.1. Moreover, 2000 initial number of epochs are used. This might appear exaggerated but is justified by the little amount of input data and the small size of the network which yields fast training.

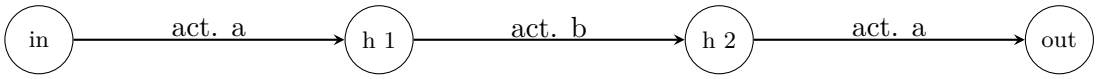

Figure A.1: Scheme of a network with four layers showing the location of the activations within the network. Activation act. a activates the output of the input layer and the output of any other hidden layer besides the output of the bottleneck layer. Act. b activates the bottleneck layer.

Table A.1: The initial selection of batch size, bottleneck size, number of epochs, learning rate, and applied activation functions.

Mini-batch size	Intrinsic dimensions	Epochs	Learning rate	Activations hidden/code
16	3/5	2000	0.0001	LeakyReLU/Tanh

Five designs for finding an optimal number of layers i.e. depth are run. The hidden layers are designed to halve the input at each step. Not within this scope is the bottleneck layer, which

has a fixed size of 5 and 3 for **R** and **H** respectively, and the first and last hidden layer (after the input layer and before the output layer). Those should provide an abstraction without shrinking the incoming data. Note that this design feature was validated in an initial exploration cycle, not included in this thesis. The five designs range from 10 layers in (a) to 2 layers in (e), always taking one layer away from the encoder and decoder, thus decreasing the architecture by two layers. These are as follows:

(a) 10 layers with layer widths: 40, 40, 20, 10, 5, 3/5, 5, 10, 20, 40, 40.

(b) 8 layers with layer widths: 40, 40, 20 , 10, 3/5, 10, 20, 40, 40.

(c) 6 layers with layer widths: 40, 40, 20 , 3/5, 20, 40, 40.

(d) 4 layers with layer widths: 40, 40, 3/5, 40, 40.

(e) 2 layers with layer widths: 40, 3/5, 40.

The model's depth is determined in a primary step because it sets a consequential part of the model's representational capacity and therefore can initiate over- and underfitting at an early stage in the hyperparameter search. The results of the experimentation are shown in fig. A.2 and table A.2 for both rarefaction levels.
For **H**, the lowest validation error of 7.74×10^{-8} and an L_2 of 0.0031 is reached with 4 layers and

Table A.2: Results for the variation of depth. Given are minimum values of training and validation error as well as the L_2. The minima were reached around the last 50 epochs of the training. The L_2 is evaluated with the model at the last epoch.

Depth	Minimum training error		Minimum validation error		L_2	
	H	**R**	**H**	**R**	**H**	**R**
10	1.53×10^{-7}	5.96×10^{-7}	2.22×10^{-7}	5.19×10^{-7}	0.0048	0.0091
8	1.17×10^{-7}	2.05×10^{-7}	1.58×10^{-7}	2.32×10^{-7}	0.0041	0.0054
6	9.76×10^{-8}	1.40×10^{-7}	1.49×10^{-7}	1.72×10^{-7}	0.0038	0.0045
4	6.29×10^{-8}	1.52×10^{-7}	7.74×10^{-8}	1.61×10^{-7}	0.0031	0.0048
2	1.29×10^{-6}	3.29×10^{-6}	1.37×10^{-6}	3.42×10^{-6}	0.0136	0.0217

constitutes the best performing design out of the five. Additionally, as seen in fig. A.2(left), a design that exceeds 4 layers results in slight overfitting from the 500th epoch on. Less than 4 layers do not reach the validation error and L_2 of the other designs, yielding the conclusion, that the capacity is too low. Overfitting occurs with 4 layers only after the 1000th epoch and is of smaller magnitude compared to the other three models that show overfitting.

For **R**, the lowest validation error of 1.61×10^{-7} is reached again with 4 layers. On the other hand, the lowest L_2 of 0.0031 and the lowest training error of 1.40×10^{-7} are reached with 6 layers. Contrary to the previously discussed case, the training error and L_2 are of lower magnitude for 6 layers, except for the validation error. Looking at fig. A.2(right), it is observed that the model with 6 layers starts to overfit after the 1500 epochs, yielding a decreasing training error and a stagnating validation error. Hence the model improved in the optimization task which additionally improves the L_2. Its generalization ability, measured by the validation error, did not improve and is greater

than the validation error reached with 4 layers. This concludes a model with 4 layers constitutes the best performing design out of the five.

Qualitatively, the overall training for both rarefaction levels is very stable. Training and validation errors do not diverge excessively and converge early in training. Separation of training and validation error occurs prominently for the hydrodynamic solution. This is thought to be connected to the emersion of sharp shock fronts towards the end of the simulation. Therefore, variance is increased in the whole dataset and also in the training- and validation set.
The number of epochs is now doubled to 4000 epochs because the lowest validation error was achieved towards the end of the training in the previous experiments. Again this is justifiable as one epoch takes less than 1s to finish and no prominent overfitting is observed.

The width of the two remaining hidden layers is examined in the following. For both the hydrodynamic and the rarefied regime five experiments are conducted, lowering the hidden units of the hidden layers from fifty to ten. Note that the decoder is chosen to be structurally a reflection of the encoder. Therefore only one parameter is changed. Results for **H** and **R** are shown in table A.3. Note that the contribution of over-and underfitting is negligible and therefore the training error is omitted. A model with 30 hidden units in encoder and decoder performs best with **H** and reaches a validation error of 1.77×10^{-8}. The corresponding $L_2 = 1.5 \times 10^{-3}$ with a shrinkage factor of 0.015. Overall the loss of each experiment with **H** is quite similar and ranges from 1.77×10^{-8} to 5.11×10^{-8}. The L_2 behaves similarly and is even equal for 50 and 30 layers. A model with 40 hidden units performs best for **R**. The corresponding validation error is 1.65×10^{-8} with $L_2 = 1.4 \times 10^{-3}$, which is smaller than **H**. The shrinkage factor is 0.125. In all experiments, a model with 10 hidden nodes performs worst. Training and validation errors over 4000 epochs for both experiments can be seen in fig. A.3. The aforementioned separation of training- and validation error, which was observed solely for **H**, is mitigated when moving away from 40 hidden units for encoder and decoder. Not shrinking the input in the first hidden layer only serves the performance when using **R**.

Table A.3: Results for the variation of width. Given is the minimum value of validation error as well as the L_2. The minima were reached around the last 50 epochs of the training, the L_2 is evaluated with the model at the last epoch.

Hidden units	Validation error		L_2		Shrinkage factor	
	H	**R**	**H**	**R**	**H**	**R**
50	1.91×10^{-8}	5.05×10^{-8}	0.0015	0.0025	0.06	0.01
40	2.65×10^{-8}	1.65×10^{-8}	0.0018	0.0014	0.075	0.125
30	1.77×10^{-8}	3.40×10^{-8}	0.0015	0.0021	0.015	0.0167
20	2.50×10^{-8}	5.25×10^{-8}	0.0017	0.0027	0.1	0.25
10	5.11×10^{-8}	3.97×10^{-7}	0.0025	0.0077	0.3	0.5

Table A.4: Results for the variation of batch sizes. Given is the minimum value of validation error as well as the corresponding epoch. Additionally, the L_2 is given but evaluated with the model at the last epoch.

Batch Size	Validation error		L_2		Epoch	
	H	**R**	**H**	**R**	**H**	**R**
32	5.40×10^{-8}	2.17×10^{-8}	0.0024	0.0017	4998	4992
16	1.95×10^{-8}	2.06×10^{-8}	0.0015	0.0016	4999	5000
8	2.25×10^{-8}	1.03×10^{-8}	0.0017	0.0012	4965	4961
4	1.52×10^{-8}	6.30×10^{-9}	0.0013	0.0010	3956	4534
2	1.15×10^{-8}	9.18×10^{-9}	0.0012	0.0013	4956	4872

Next, the mini-batch size is analyzed. Epochs are increased by 1000 epochs, as training- and validation error show potential to decrease further as seen in fig. A.3 for **R** with 40 hidden nodes. Results for **H** and **R** are displayed in table A.4. Experiments are conducted with mini-batch sizes of 2, 4, 8, 16, 32. Batch sizes to the power of 2 are typically chosen to fully exploit the computational capabilities of a GPU i.e. aligning the batch size with the way memory is structured within a GPU. The smallest batch size of 2 yields the lowest validation error of 1.15×10^{-8} with corresponding $L_2 = 0.0012$ at epoch 4956 for **H**. The lowest validation error with 6.30×10^{-9} is achieved for **R** at epoch 4534 with a batch size of 4. The corresponding $L_2 = 0.001$. Compared to a batch size of 16 in the previous experiments, it is observed that small batch sizes have a regularizing effect on training as described in chapter 3 and therefore are beneficial to generalization. At the same time, the lower the batch sizes are, the more unstable is the training as seen in appendix B. The oscillations which begin with batch sizes of 8 and lower, which make the training unstable, can be battled with a lower learning rate as soon as training starts to tremble. Additionally, small batch sizes drastically increase training time, thus a batch size as low as 2 is not used for the next experiments. In conclusion, a batch size of 4 is chosen. Furthermore, a reduction of the learning rate from 1×10^{-4} to 1×10^{-5} is applied after the 3000th epoch.

Eight experiments with different activation functions, namely ReLU, ELU, Tanh, SiLU, and LeakyReLU, are performed. The experiment designs and results are given in table A.5 for hidden and code activations. With **H**, a combination of ELU and ELU for hidden and code activation, yields the best results in validation error with 4.44×10^{-9} and a corresponding $L_2 = 0.0008$. These values are achieved at the last epoch. For **R**, a combination of ReLU and ReLU for hidden and code activation, produces a validation error of 7.18×10^{-9} and a corresponding $L_2 = 0.0009$. Both are reached close to the last epoch. Note that all models reach their lowest loss at, or very close to the last epoch. The reason is the stable training after the 3000th epoch, where the learning rate is lowered to 1×10^{-5} as seen in appendix A. This measure shows in all experiments an immediate success for learning. Both validation and training errors fall at the 3001st epoch and only decrease slightly thereafter. This behavior clearly shows that the updates to the free parameters θ were too big, which prohibitively slowed down or even prevented the learning process. Small updates to θ made all models quickly reach a minimum.

If the learning rate could have been reduced earlier in training, whilst producing similar results, remains unanswered. The results are satisfactory. Note that for **R** in the previous experiment, a validation error of 6.30×10^{-9} was achieved, which is slightly lower than the current result.

Nonetheless, it is decided to take the current model as the final result.

Table A.5: Results for the variation of activations for hidden-/code layers. Given is the minimum value of validation error as well as the corresponding epoch and the L_2. The L_2 is evaluated with the models saved when the minimum validation error was achieved during training.

Activations hidden/code	Validation error		L_2		Epoch	
	H	**R**	**H**	**R**	**H**	**R**
ReLU/ReLU	9.79×10^{-9}	7.18×10^{-9}	0.0010	0.0009	5000	4998
ELU/ELU	4.44×10^{-9}	1.11×10^{-8}	0.0008	0.0012	5000	5000
Tanh/Tanh	7.83×10^{-9}	2.58×10^{-8}	0.0011	0.0018	5000	5000
SiLU/SiLU	7.69×10^{-9}	1.37×10^{-8}	0.0011	0.0013	5000	5000
LeakyReLU/LeakyReLU	1.86×10^{-8}	9.39×10^{-9}	0.0015	0.0010	5000	4997
ELU/Tanh	5.49×10^{-9}	1.87×10^{-8}	0.0008	0.0014	5000	5000
LeakyReLU/Tanh	1.00×10^{-8}	1.42×10^{-8}	0.0010	0.0012	4997	4992
ELU/SiLU	8.11×10^{-9}	1.93×10^{-8}	0.0011	0.0015	5000	5000

The final hyperparameters for both input data are summarized below in table A.6. From the initial models to the final models, the decrease in validation error gained $\approx 1.5 \times 10^{-7}$ for **H** and $\approx 7.2 \times 10^{-8}$ for **R** which is 93% of the initial values for both models.

Table A.6: Summary of the final hyperparameters for both input data.

Input data	Act. hidden/code	Batch size	Width	Depth	Learning rate	Epochs
H	ELU/ELU	4	30	4	$10^{-4}/10^{-5}$	≈ 3000
R	ReLU/ReLU	4	40	4	$10^{-4}/10^{-5}$	≈ 3000

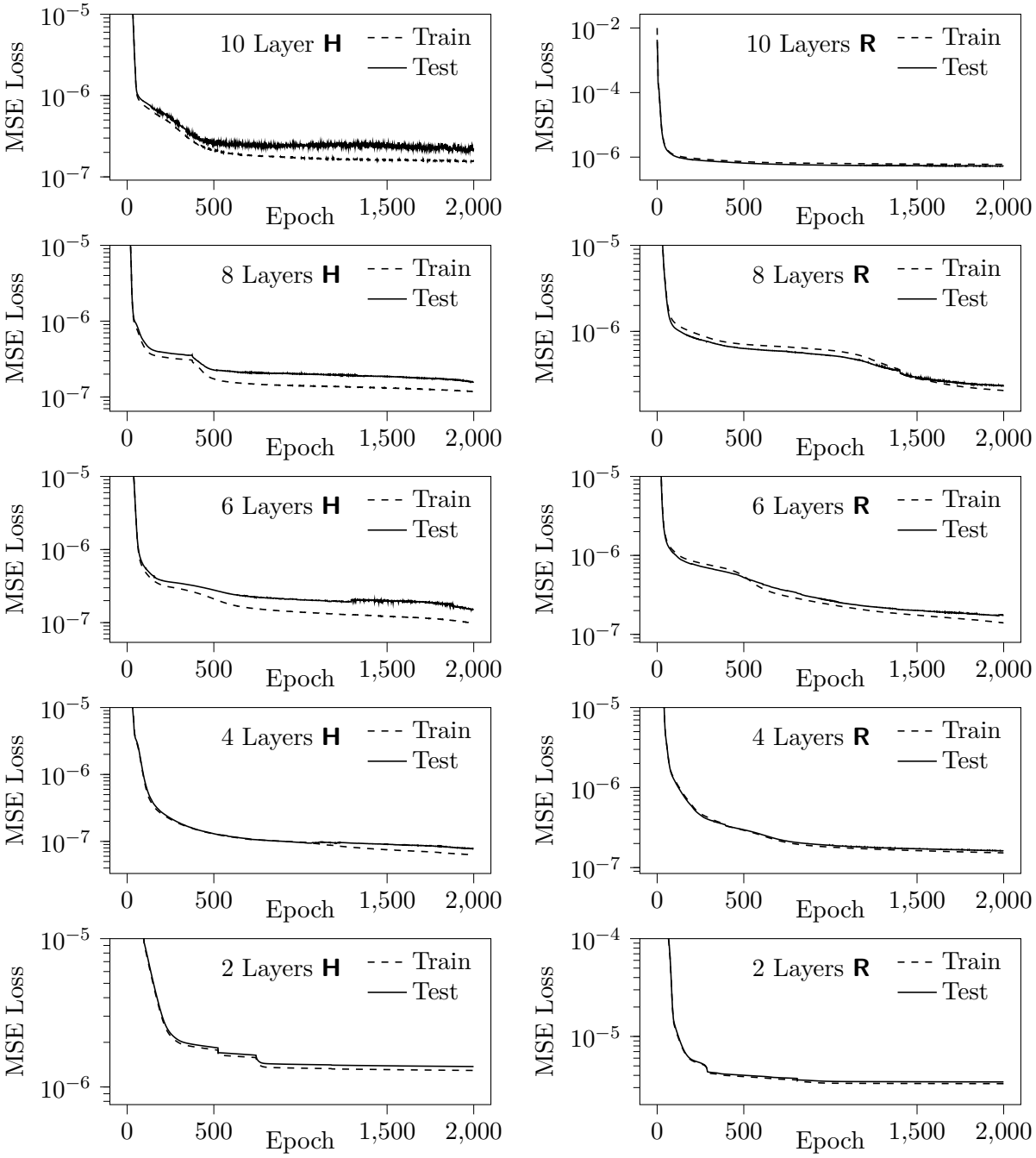

Figure A.2: Five experiments over the different depths with **H** left and **R** right. The number of layers used for every experiment is given. Training and validation loss are shown over 2000 epochs.

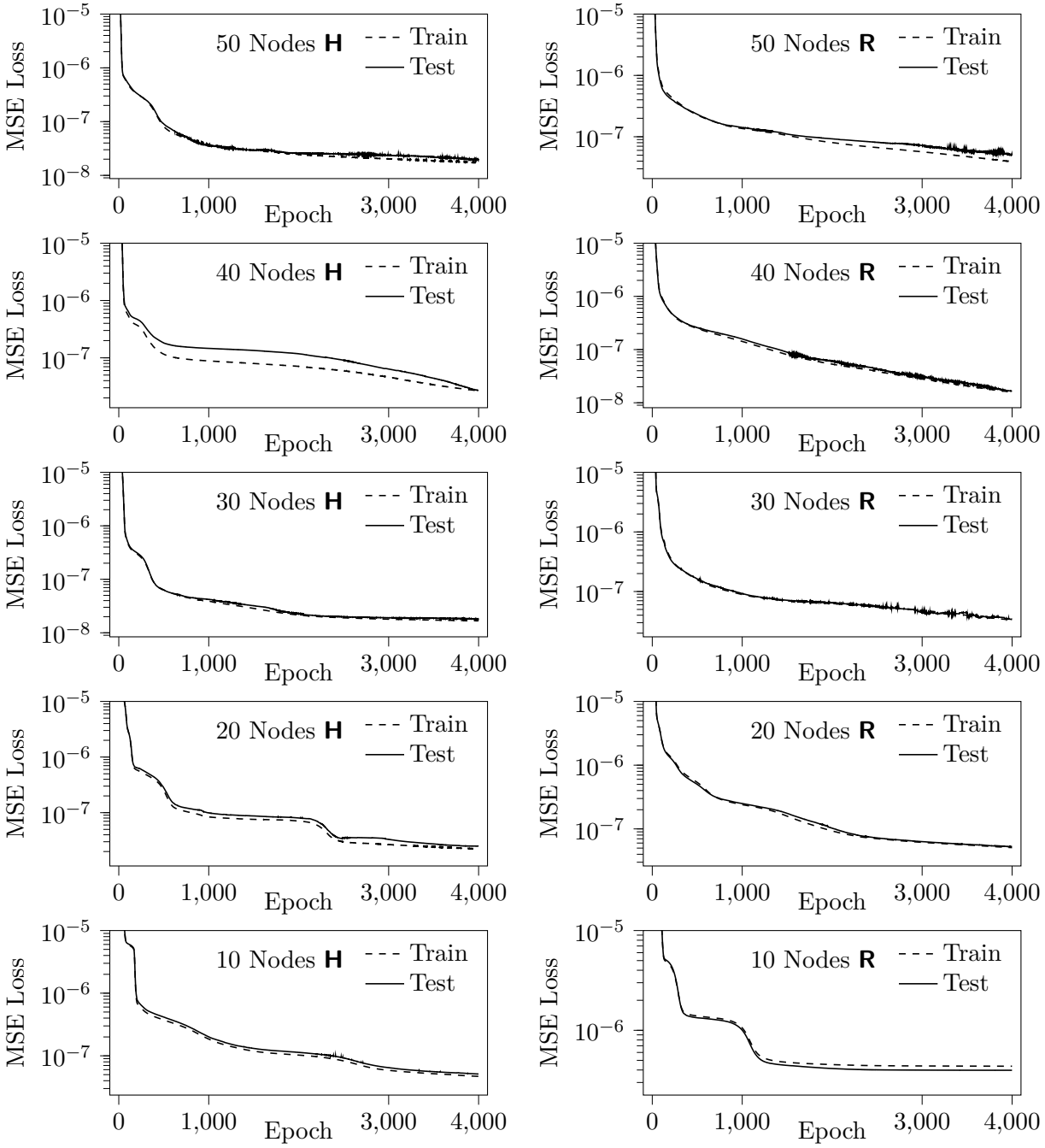

Figure A.3: Five experiments over different widths with **H** left and **R** right. The number of nodes used for every experiment is given. Training and validation loss are shown over 4000 epochs.

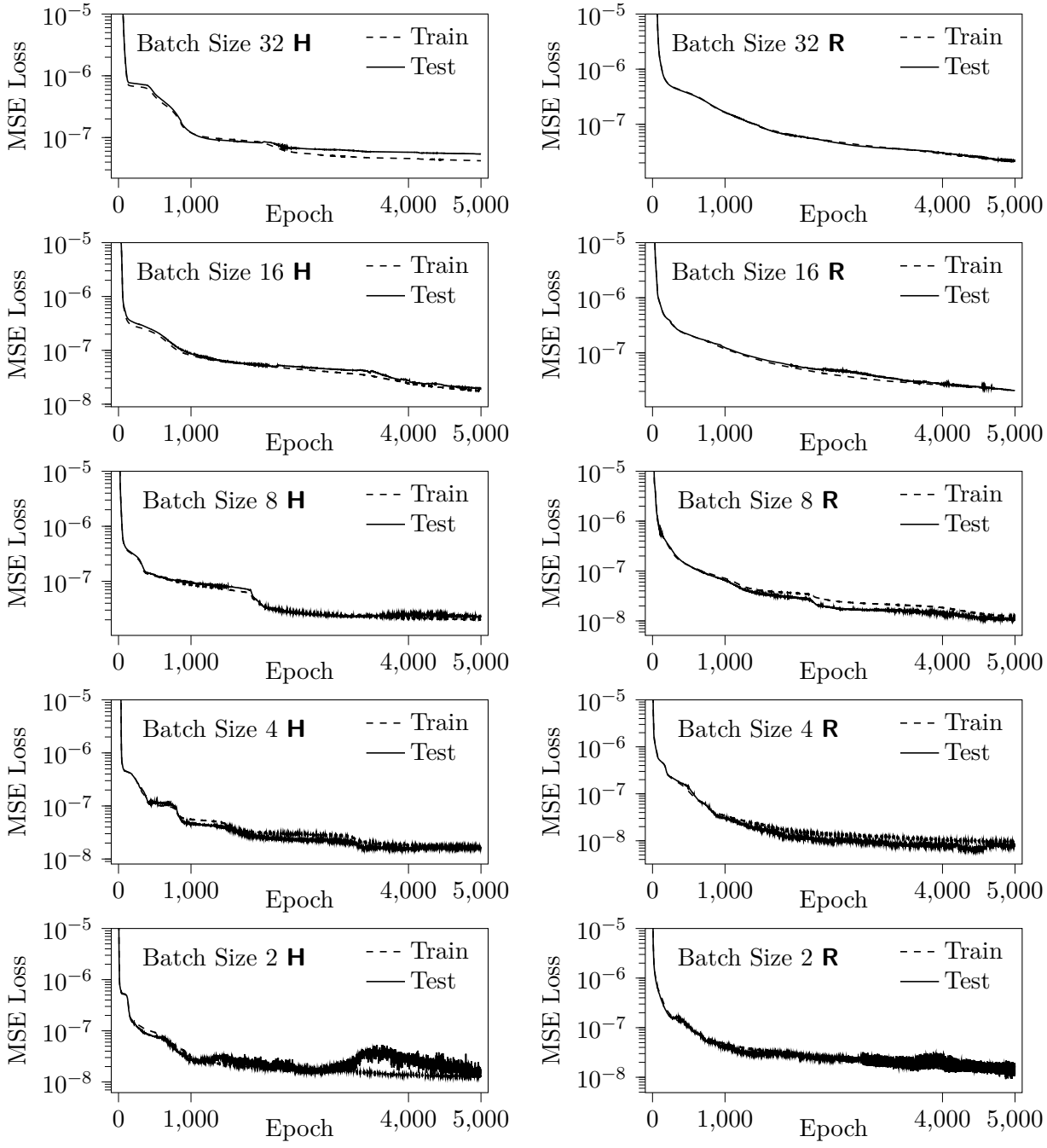

Figure A.4: Five experiments over different batch sizes with **H** left and **R** right. The batch size used for every experiment is given. Training and validation loss are shown over 5000 epochs.

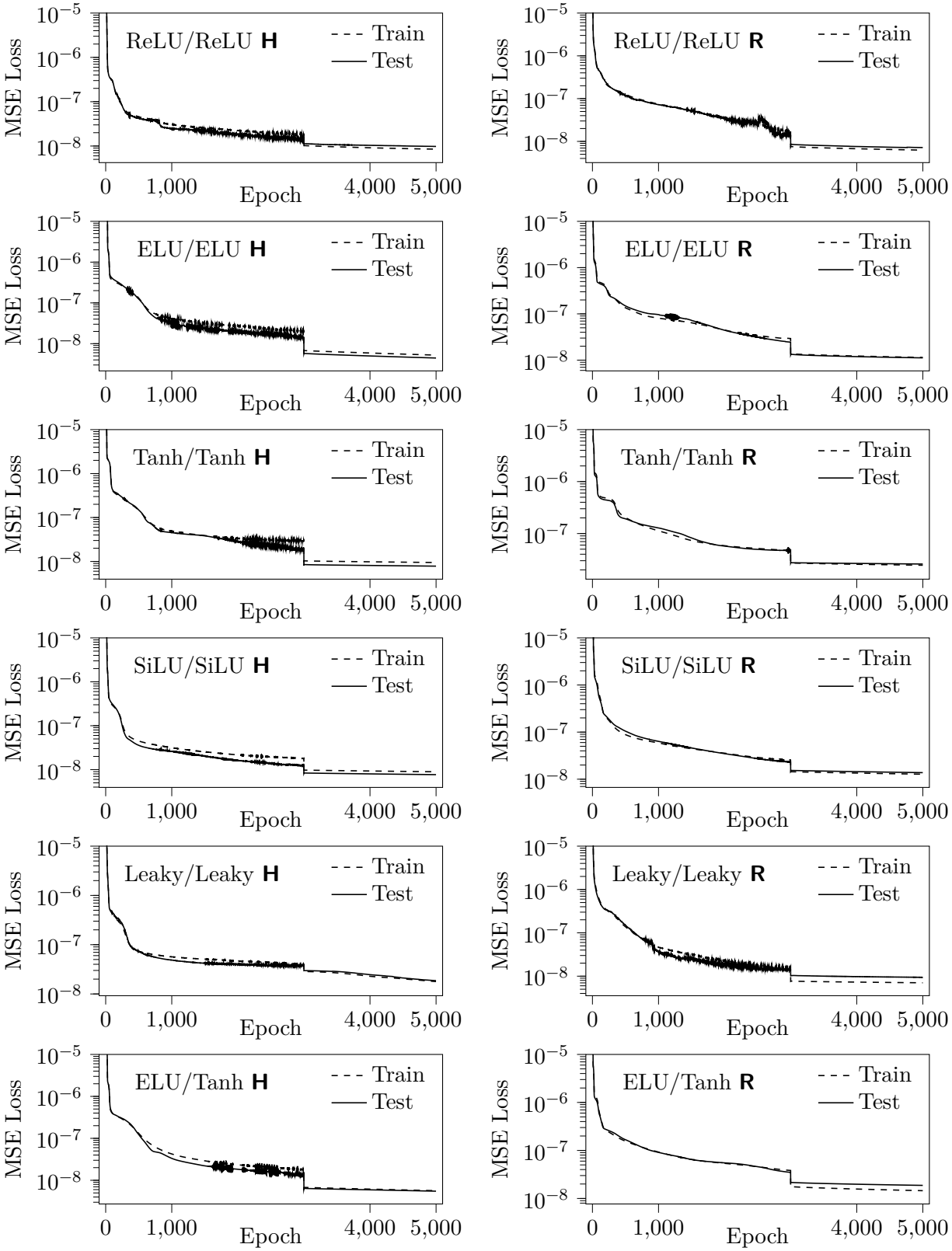
ReLU/ReLU H
ReLU/ReLU R
ELU/ELU H
ELU/ELU R
Tanh/Tanh H
Tanh/Tanh R
SiLU/SiLU H
SiLU/SiLU R
Leaky/Leaky H
Leaky/Leaky R
ELU/Tanh H
ELU/Tanh R
Train
Test
MSE Loss
Epoch
0
1,000
4,000
5,000
10^{-5}
10^{-6}
10^{-7}
10^{-8}

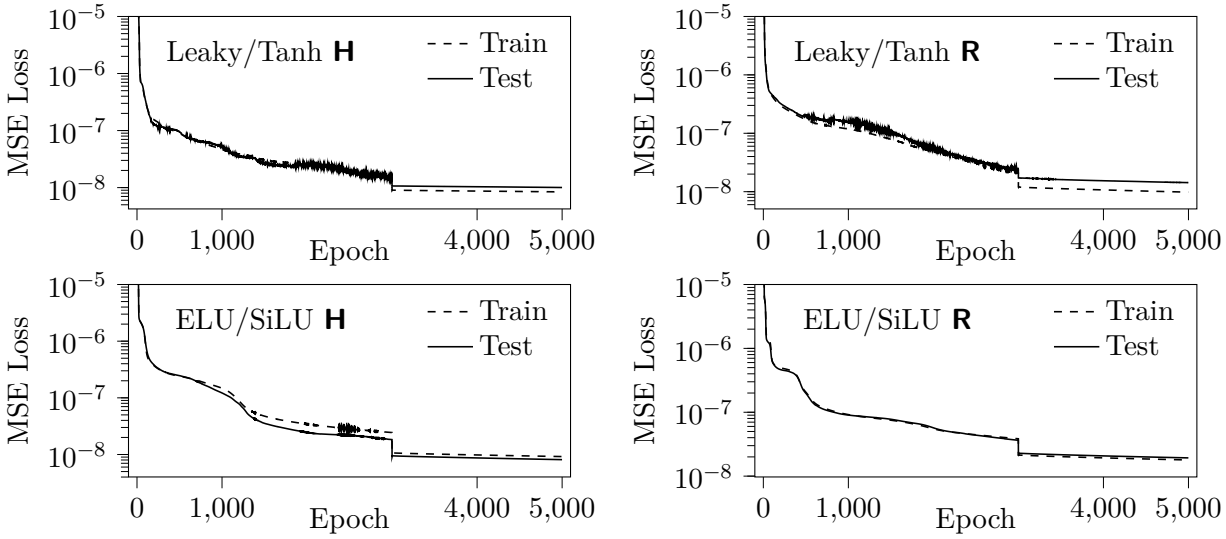

Figure A.5: Eight experiments with different combinations of activation functions for **H** (left) and **R** (right). Shown are training- and validation error over 5000 epochs.

B Hyperparameters for the Convolutional Autoencoder

The finding of appropriate hyperparameters for the convolutional autoencoder is described here. The hyperparameters include batch size, non-linear activation functions, number of epochs for training and learning rate, and number of layers i.e. depth. Depth comprises kernel size, stride width as well as the number of channels per layer.
This analysis follows the prior finding of hyperparameters for the fully-connected autoencoder, hence utilizes insights thereof. Additionally, this analysis follows a slightly different scheme than before, as there are solely 40 examples for training and validation for both rarefaction levels **H** and **R**. Therefore, it is tried to find a combined model that performs well on both rarefaction levels. With this measure, datasets for both rarefaction levels are concatenated to one dataset of 80 examples for training and validation. Furthermore, this approach aims at answering how well a model can generalize about the BGK model for different rarefaction levels in Sod's shock tube.
Again, the initial model is small and architecture and hyperparameters are summarized in table B.1. The activations and learning rate stem from conclusions made in appendix A. The application of

Table B.1: The initial selection of hyperparameters comprises 6 layers, of which 4 are either convolutional (Conv.) or transposed convolutional (Tr.Conv.). The learning rate is switched from 10^{-4} to 10^{-5} at the 500th epoch as in appendix A. Depth counts the number of convolutional/transposed convolutional layers and excludes the fully connected layers.

Encoder				Decoder			
Layer	Type	Channels	Output size	Layer	Type	Channels	Output size
1	Conv	8	5×40	4	Lin.	-	128
2	Conv.	16	1×8	5	Tr.Conv.	16	1×8
3	Lin.	-	5	6	Tr.Conv.	8	25×200
Epochs	Act. hidden/code		Batch size	Depth	Kernel size	Stride width	Learning rate
1000	ReLU/ReLU		2	4	5×5	5×5	$10^{-4}/10^{-5}$

activation functions follows the same scheme as described in appendix A seen in fig. A.1. Kernel size and stride width are chosen to circumvent checkerboard artifacts, as described in chapter 3. The number of channels is inspired by the architecture chosen in [3].
The number of available examples for training and validation is limited as previously stated. Therefore, the split in training and validation sets encompasses the risk of a bias in one of the sets. For instance, if out of the 40 examples, a few of them, maybe five, contain considerable variance to the other examples and all of them are found in the training set, then the validation error could not estimate the model's ability to generalize. Therefore, the k-fold algorithm described in [5] is adopted. The k-fold algorithm provides from the complete shuffled dataset, k independent splits

into training and validation set with which the model is trained. By that, each example gets the chance to be either in the training or validation set once. For an 80/20 split, as used in this thesis and described in chapter 3, five independent folds can be obtained. Therefore, with 80 available examples, the training set P_{train} consists of 74 examples and the validation set P_{val} of the remaining 16 examples. The results of the said preliminary experiment are summarized in table B.2 and appendix B.

The lowest validation error of 1.3×10^{-5} is achieved with the second fold at the last epoch and

Table B.2: Training of five independent folds. Summary of minimum training- and minimum validation error for a small model with two convolutional layers in the encoder as well as the corresponding L_2 and the epoch in which those values are reached. The mean and standard deviation of the validation error are 3.55×10^{-5} and 2.13×10^{-5} respectively with a corresponding variance of 4.56×10^{-10}.

Fold	Minimum training error	Minimum validation error	L_2	Epoch
1	2.4×10^{-5}	7.0×10^{-5}	0.053	498
2	1.4×10^{-5}	1.3×10^{-5}	0.044	1000
3	1.7×10^{-5}	5.0×10^{-5}	0.057	1000
4	1.7×10^{-5}	1.8×10^{-5}	0.039	997
5	1.6×10^{-5}	2.7×10^{-5}	0.053	1000

$L2 = 0.044$. As the training error is lower than the validation error, it is assumed that the "difficult" examples are within the training set. Therefore, the training set could be biased. The second-lowest validation error of 1.8×10^{-5} and a corresponding $L_2 = 0.039$ is achieved with fold 4 at the 997th epoch. For both folds, training and validation errors evolve in unison and get unstable even before the 500th epoch. The instability is eliminated by lowering the learning rate at said epoch, but the training does not improve thereafter as in appendix A. For the other folds, a separation of training and validation error can be observed and less instability. The mean validation error of 3.55×10^{-5} gives an estimate of the models performance with a standard deviation of 2.13×10^{-5} and variance of 4.56×10^{-10}. For the continuation of experiments fold 4 is used, as it provides a balanced split in training- and validation split which also manifests in the lowest L_2-error of all folds.

Next, the capacity of the model is increased by successively adding convolutional layers, thus obtaining two additional models. One encompasses three convolutional layers, the other four convolutional layers in encoder and decoder. An exact description of both architectures is summarized in table B.4. The maximum number of channels for this analysis is kept at 16. This measure decreases the growth rate of channels per layer, which is quadratic for the first model and now scales to linear to increase capacity rather smoothly. Note that it is also possible to keep the growth rate constant while adding layers. Here this is done in the following steps.

Kernel size and stride width shrink the input as described in chapter 3. In the previous model shrinkage evolved with a pace of $\frac{1}{5}$. This reduction rate can reduce the input size over two successive layers to unity. Therefore, the same kernel size and stride width can only be adopted by using excessive zero padding between successive convolutional layers. To overcome this issue, a balance between zero padding, which cannot be omitted for four convolutional layers with the given input dimensions, and kernel size and stride width, needs to be found. Here both features are chosen to have sizes 3×3. Extra padding, which is needed for one to reduce the shrinkage rate per layer in the encoder and for the other to transpose the shrinkage of the encoder in the decoder, is summarized in table B.4. In `pytorch`'s implementation of transposed convolutional layers, a handy

parameter can be used called output padding. This parameter provides a measure to effectively increase the output size by one, left or at the bottom of the output, to resolve the ambiguity when stride > 1. Then the respective convolutional layer maps multiple input sizes to the same output size. For example, the second and sixth layer of the model with three convolutional layers in encoder and decoder. Here the convolutional layer maps a size of 23 to 8, however, the respective transposed convolutional layer maps size 8 to size 22. In this case, output padding resolves the issue by increasing the output size by one.

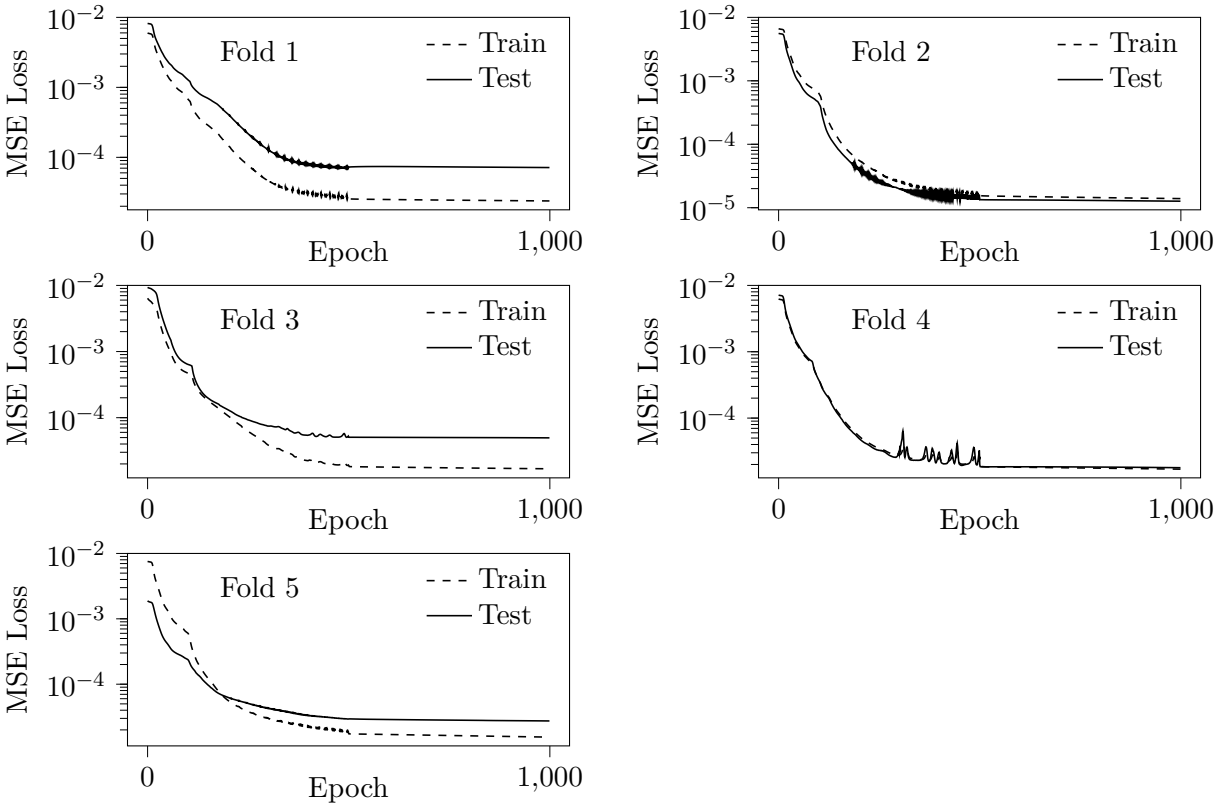

Figure B.1: Training- and validation error over 1000 epochs for five independent folds.

Results for both models are summarized in table B.4. Training- and validation errors for the model with three convolutional layers achieve slightly better results than the small model. On the contrary does the L_2 not achieve the results of the small model with $L_2 = 0.044$. In appendix B the evolution of training- and validation error is depicted over 2000 epochs. The model with three convolutional layers shows an unstable training after the 500th epoch, which is ignored for now. It can be observed that the model with four convolutional layers is underfitting and does not achieve comparable results to the small model.

Next, the batch size is increased from two to four. The initial batch size was chosen so small as the limited available data permits reasonable training time. The results for all three models are

Table B.3: Architecture for the models with three (left) and four (right) convolutional layers in encoder and decoder. Kernel size and stride width are 3×3 for both features and models.

Encoder				
Layer	Type	Channels	Padding	Output
1	Conv	4	in: 1/1	9×67
2	Conv.	8	in: 0/1	3×23
3	Conv.	16	in: 0/1	1×8
4	Lin.	-	-	5

Decoder				
Layer	Type	Channels	Padding	Output
5	Lin.	-	-	128
6	Tr.Conv.	16	in: 0/1 out: 0/1	1×8
7	Tr.Conv.	8	in: 0/1 out: 0/1	3×23
8	Tr.Conv.	1	in: 0/1	25×200

Encoder				
Layer	Type	Channels	Padding	Out
1	Conv	2	in: 3/2	10×68
2	Conv.	4	in: 3/2	5×24
3	Conv.	8	in: 3/2	3×9
4	Conv.	16	in: 3/3	1×3
5	Lin.	-		5

Decoder				
Layer	Type	Channels	Padding	Out
6	Lin.	-	-	128
7	Tr.Conv.	16	-	3×9
8	Tr.Conv.	8	in: 2/2 out: 0/1	5×24
9	Tr.Conv.	4	in: 3/2	9×68
10	Tr.Conv.	1	in: 1/2	25×200

Table B.4: Results for increasing the number of layers. Summary of minimum training- and minimum validation error for a model with three and a model with convolutional layers in the encoder as well as the corresponding L_2 and the epoch in which those values are reached.

Layer	Minimum training error	Minimum validation error	L_2	Epoch
3	1.4×10^{-5}	1.5×10^{-5}	0.044	1975
4	7.3×10^{-4}	8.1×10^{-4}	0.327	1995

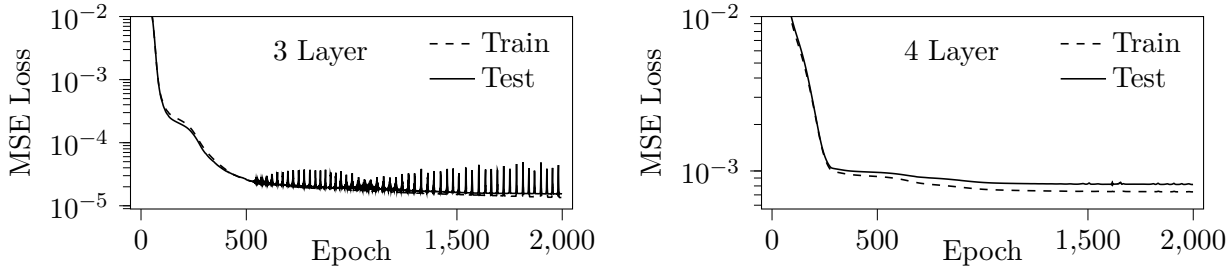

Figure B.2: Increasing the number of layers. Shown are training- and validation errors over 2000 epochs a model with two and a model with three convolutional layers in the encoder. Channels are chosen to reach a maximum of 16 in the last layer of the encoder. Kernel size and stride width are both 3×3.

shown in table B.5. The models with two and three convolutional layers benefit from increasing the batch size. The small model reaches the best training- and validation error with 6.0×10^{-6} and 8.0×10^{-6} respectively and $L_2 = 0.03$. In appendix B it can be observed, that the increased batch size results in a stable training for both shallow models. The underfitting of the deep model with four convolutional layers in encoder and decoder is increased.

Table B.5: Increasing the batch size to four. Summary of minimum training- and minimum validation error for the models with two, three, and four convolutional layers in the encoder as well as the corresponding L_2 and the epoch in which those values are reached.

Layer	Min. training error	Min. validation error	L_2	Epoch
2	6.0×10^{-6}	8.0×10^{-6}	0.030	1999
3	1.0×10^{-5}	1.3×10^{-5}	0.038	1965
4	6.0×10^{-3}	6.9×10^{-3}	0.94	109

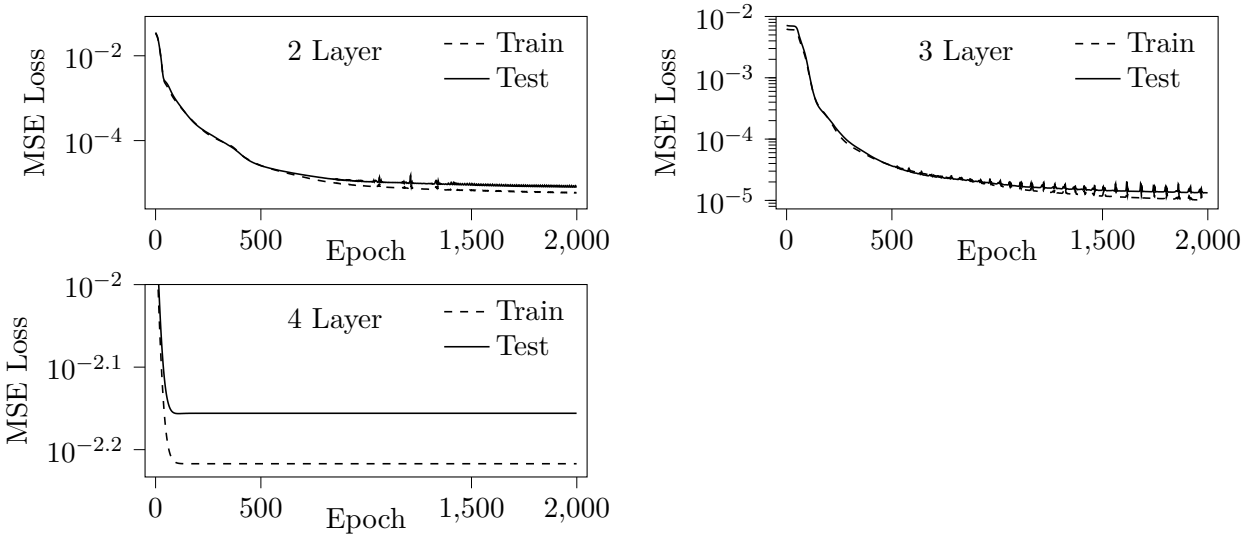

Figure B.3: Increasing the batch size to four. Shown are training- and validation error over 2000 epochs for the models with two, three, and four convolutional layers in the encoder.

The underfitting of the deepest model is now tackled by increasing the capacity of the model by raising the channel growth rate to quadratic, as it is found in [3]. The same is performed for the model with three convolutional layers in encoder and decoder. Additionally, the channel sizes of the small model are increased. The results and available channel sizes in the order of appearance in the encoder are summarized in table B.6. Note that the decoder mirrors the channel sizes of the encoder. The small model does not learn at all as seen in appendix B. The training was repeated several times, but no improvement could be produced. The reason for this behavior is not known and can't be classified as underfitting and overfitting, as there is no change in training-

and validation error observed. On the other hand, the deep network with four convolutional layers achieve comparable results to the small model in the previous experiment. The model with three convolutional layers improves slightly. In conclusion, the quadratic growth rate of the channels starting from eight channels is suitable for the following experiments, for which the three-layer model is discarded as the other models reach the lowest validation error so far.

Table B.6: Increasing the channel growth rate to quadratic. Summary of minimum training- and minimum validation error for the models with two, three, and four convolutional layers in the encoder as well as the corresponding L_2 and the epoch in which those values are reached. Note that the channel sizes of the two-layer model are only increased, the growth rate has already been quadratic.

Layer	Channels	Minimum training error	Minimum validation error	L_2	Epoch
2	16,32	6.8×10^{-3}	7.6×10^{-3}	1.0	0
3	8,16,32	9.0×10^{-6}	1.1×10^{-5}	0.037	1985
4	8,16,32,64	7.0×10^{-6}	9.0×10^{-6}	0.033	1953

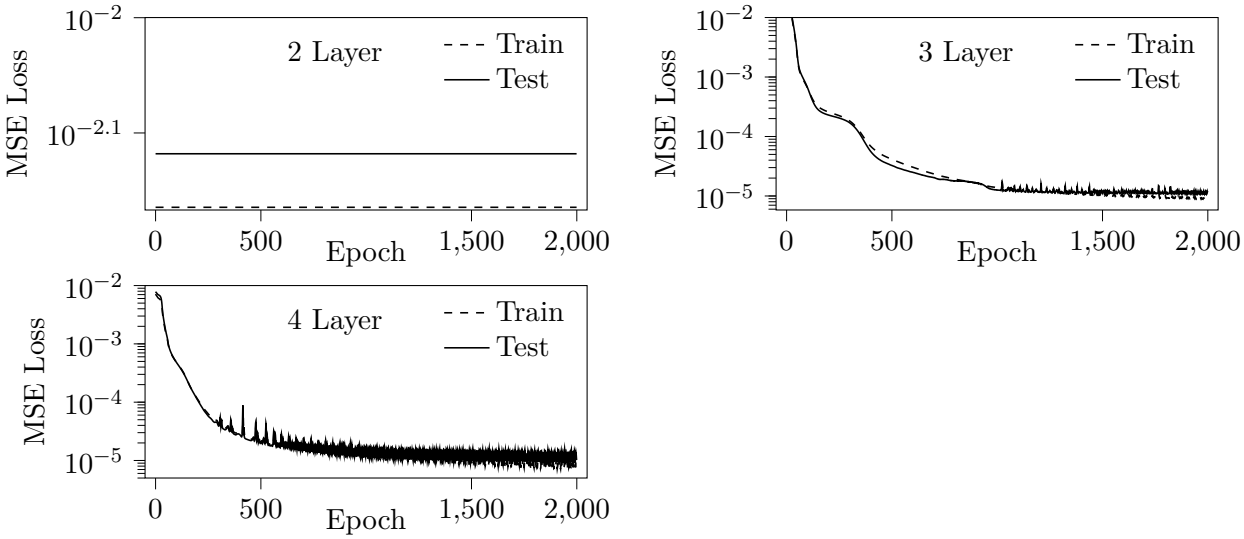

Figure B.4: Increasing the channel growth rate to quadratic. Shown are training- and validation errors over 2000 epochs for the model with two, three, and four convolutional layers in the encoder.

The variation of activation functions follows the same scheme as already outlined in appendix A. Eight experiments are conducted using ReLU, ELU, Tanh, SiLU, and LeakyReLU in different combinations for the hidden convolutional layers and the code layer. Results are summarized in table B.7. Training- and validation error over 2000 epochs are displayed in fig. B.8. For both models, the validation error reaches the region of 10^{-6} using combinations of ELU, SiLU, and Tanh. With applying rectifiers, the validation error stays in the region of 10^{-5}. Especially, with utilizing SiLU/SiLU for the four-layer model, the validation error reaches a minimum of 6.0×10^{-6}. Utilizing the combinations ELU/SiLU and ELU/Tanh for the two-layer model also yields a minimum

validation error of 6.0×10^{-6}. In addition, this combination produces the smallest L_2-error with $L_2 = 0.024$ applying ELU/SiLU for the four-layer model and applying ELU/Tanh for the two-layer model produces $L_2 = 0.023$. These values correspond to the minimum training error which is 4.0×10^{-6} and 3.0×10^{-6} respectively. Here the four-layer model overfits after the 500th epoch which produces, compared to the other models, a significant generalization gap. The same logic applies to the two-layer model with ELU/Tanh but yields a smaller generalization gap. In general, the training of the four-layer model is unstable for all combinations of activation functions. The greater amount of free parameters, compared to the two-layer model, requires a smaller learning rate or a greater batch size to stabilize the training. Finally, the combination of SiLU/SiLU is chosen for the four-layer model and ELU/SiLU for the two-layer model. Both choices lead to the lowest validation error while maintaining the generalization gap small.

A comparison with the validation loss of the fully connected model suggests that the two and three-

Table B.7: Variation of activations for hidden-/code layers. Summary of minimum training- and minimum validation error for the models with two and four convolutional layers in the encoder as well as the corresponding L_2 and the epoch in which those values are reached.

Act. hid./code	Min. training error		Min. validation error		L_2		Epoch	
	2 Layer	4 Layer	2 Layer	4 Layer	2 Layer	4 Layer		
ELU/ELU	5.0×10^{-6}	4.0×10^{-6}	7.0×10^{-6}	7.0×10^{-6}	0.026	0.031	1969	1365
ELU/SiLU	5.0×10^{-6}	4.0×10^{-6}	6.0×10^{-6}	8.0×10^{-6}	0.026	0.024	1991	1808
ELU/Tanh	3.0×10^{-6}	5.0×10^{-6}	6.0×10^{-6}	9.0×10^{-6}	0.023	0.029	1998	1498
Leaky/Leaky	6.0×10^{-6}	7.0×10^{-6}	1.1×10^{-5}	1.0×10^{-5}	0.032	0.032	1976	1971
Leaky/Tanh	5.0×10^{-6}	6.0×10^{-6}	7.0×10^{-6}	9.0×10^{-6}	0.030	0.035	1977	1722
ReLU/ReLU	8.0×10^{-6}	7.0×10^{-6}	1.3×10^{-5}	1.1×10^{-5}	0.036	0.036	1984	1989
SiLU/SiLU	6.0×10^{-6}	6.0×10^{-6}	8.0×10^{-6}	6.0×10^{-6}	0.030	0.035	1972	1550
Tanh/Tanh	8.0×10^{-6}	5.0×10^{-6}	8.0×10^{-6}	8.0×10^{-6}	0.033	0.030	1999	975

layer model gets stuck at a local minimum of $\min J(\theta)$. Therefore, the input data is augmented for the following experiments. All examples in the training- and validation set are rotated around their center by 180° and flipped about their central vertical axes. These methods add examples to the input data without altering the information about the flow field present in each example. In fig. B.5 is an example in its original, rotated, and flipped version. The flow field stays the same, just the direction in which it evolves has been altered. Using this method, available examples for training and testing triple from 80 to 240 examples.

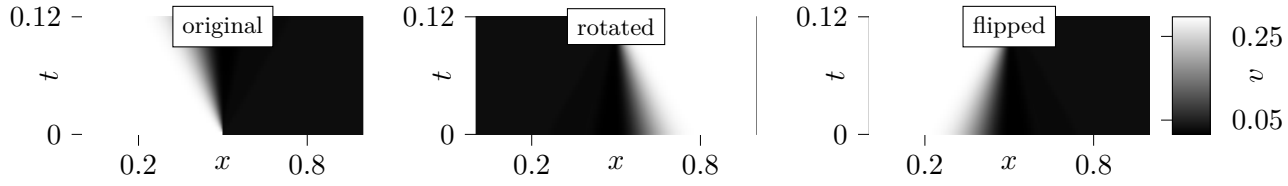

Figure B.5: Rotated and flipped version of one original example from the dataset showing v over x and t.

Results for using augmented data are summarized in table B.8. Two experiments are conducted for each model. One with learning rate adjustment, which decreases from 1×10^{-4} to 1×10^{-5} after the 1250th epoch, and one without. The minimum validation error ranges between 2.2×10^{-5} and 1.4×10^{-5}. Therefore, data augmentation could not decrease the validation error further. Instead, it increases. However, as seen in fig. B.6 and fig. B.7, the training is stabilized compared to the previous experiments. In addition, overfitting cannot be observed for the two-layer model. The four-layer model overfits after the around the 1150th epoch. Furthermore, both models benefit from reducing the learning rate. A drop in the training and validation errors can be observed after the 1250th epoch for both models.

Table B.8: Data augmentation with and without learning rate adjustment after the 1250th epoch. Summary of minimum training- and minimum validation error for the models with two and four convolutional layers in the encoder and the corresponding L_2 and the epoch in which those values are reached.

Layer	Min. training error	Min. validation error	L_2	Epoch
2	1.5×10^{-5}	1.4×10^{-5}	0.048	2000
2 (lr adjusted)	2.2×10^{-5}	2.2×10^{-5}	0.064	2000
4	7.0×10^{-6}	1.6×10^{-5}	0.034	1991
4 (lr adjusted)	1.1×10^{-5}	1.9×10^{-5}	0.045	2000

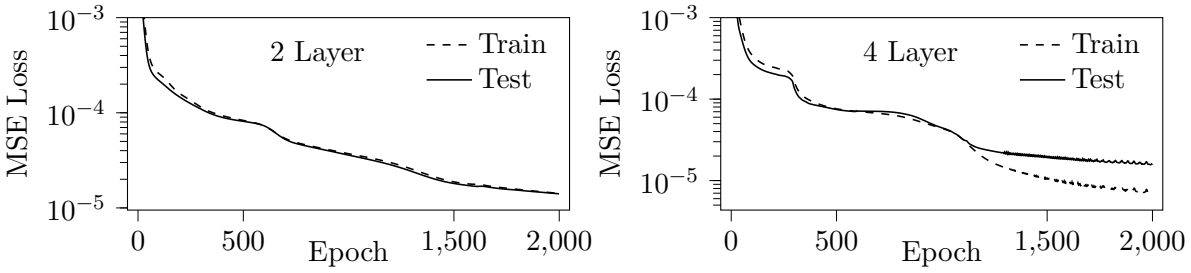

Figure B.6: Using augmented data. Shown are training- and validation errors over 2000 epochs for the model with two and four convolutional layers in the encoder.

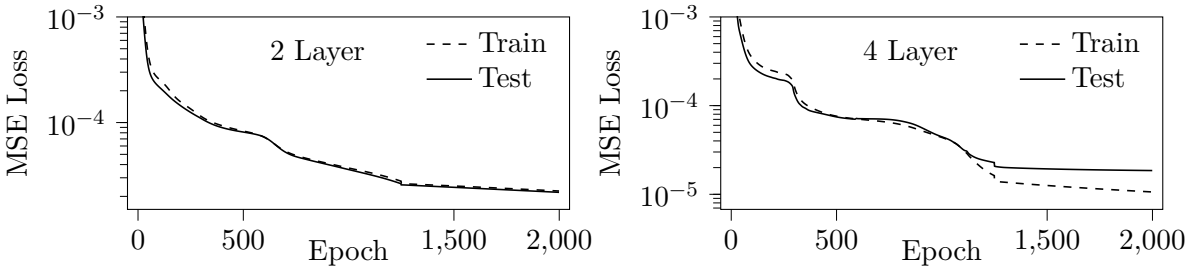

Figure B.7: Learning rate adjustment with augmented data. Shown are training- and validation errors over 2000 epochs for the model with two and four convolutional layers in the encoder.

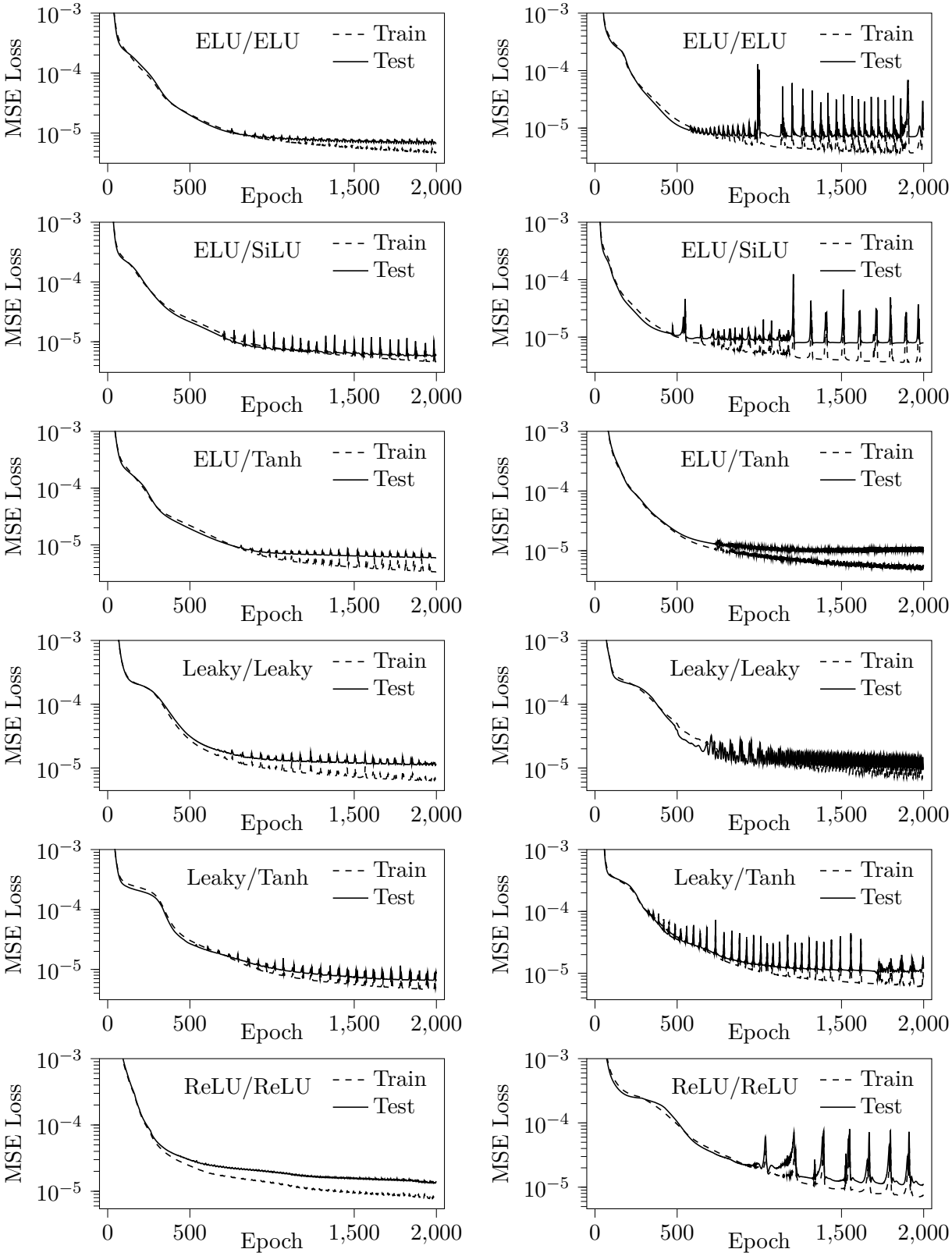
ELU/ELU
ELU/SiLU
ELU/Tanh
Leaky/Leaky
Leaky/Tanh
ReLU/ReLU
Train
Test
MSE Loss
Epoch
10^{-3}
10^{-4}
10^{-5}
0
500
1,500
2,000

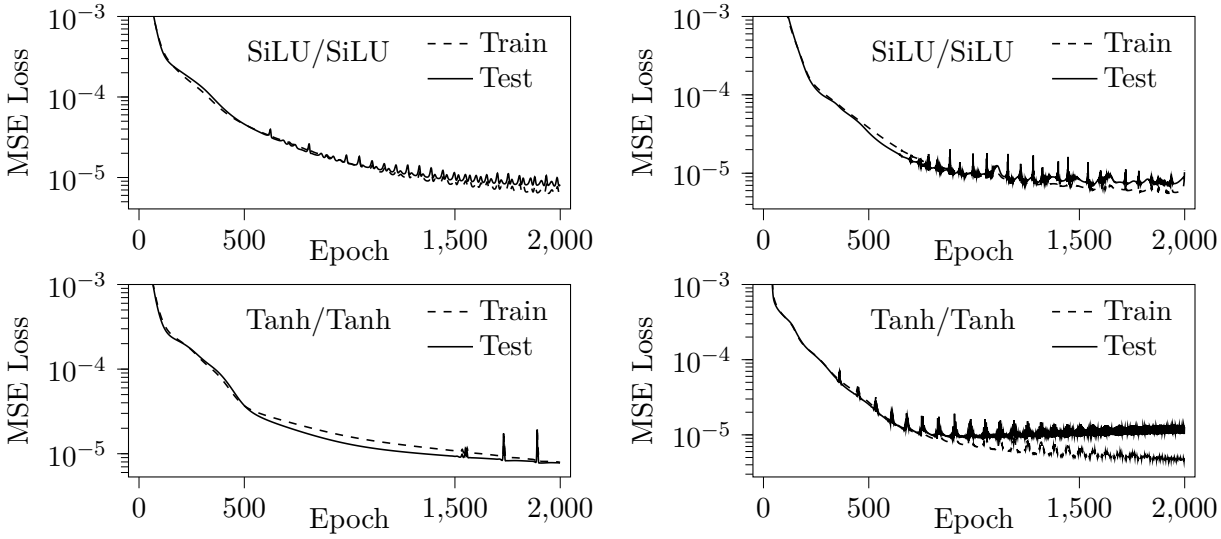

Figure B.8: Eight experiments with different combinations of activation functions for the model with two (left) and four (right) convolutional layers in the encoder. Shown are training- and validation errors over 2000 epochs.

To this end, the finding of hyperparameters for a convolutional autoencoder using both rarefaction levels as input data failed to produce comparable results to those obtained by the fully connected autoencoders using both rarefaction levels as separate datasets. The analysis stops here out of brevity but is far from an end. Changing the kernel size and especially the stride width, which yields non-overlapping kernel positions in all models, changing the loss function, to for example `pyTorch`'s BCEWithLogitsLoss, or even adding more layers and so forth are still not analyzed, but are proposed for further investigations. As a final model, the two-layer model trained without data augmentation is chosen. This model encompasses the smallest number of free parameters while achieving the lowest validation error.

Table B.9: Final model.

Layer	Channels	Activations	Batch size	Learning rate	Num. Epochs
2	8,16	ELU/SiLU	4	1×10^{-4}	2000

Bibliography

[1] Bhatnagar, Gross and Krook, *A model for collision processes in gases*, .

[2] J. Fan, *Rarefied gas dynamics: Advances and applications*, *Advances in Mechanics* **43** (03, 2013) 185–201.

[3] K. Lee and K. T. Carlberg, *Model reduction of dynamical systems on nonlinear manifolds using deep convolutional autoencoders*, .

[4] S. R. Bukka, R. Gupta, A. R. Magee and R. K. Jaiman, *Assessment of unsteady flow predictions using hybrid deep learning based reduced order models*, 2020.

[5] I. J. Goodfellow, Y. Bengio and A. Courville, *Deep Learning*. MIT Press, Cambridge, MA, USA, 2016.

[6] D. Rumelhart, G. Hinton and R. Williams, *Learning internal representations by error propagation*, .

[7] D. H. Ballard, *Modular learning in neural networks*, .

[8] S. Rifai, P. Vincent, X. Muller, X. Glorot and Y. Bengio, *Contractive auto-encoders: Explicit invariance during feature extraction*, .

[9] D. P. Kingma and M. Welling, *Auto-encoding variational bayes*, 2014.

[10] I. Tolstikhin, O. Bousquet, S. Gelly and B. Schoelkopf, *Wasserstein auto-encoders*, 2019.

[11] S. Hochreiter and J. Schmidhuber, *Long short-term memory*, *Neural Computation* **9** (1997) 1735–1780.

[12] A. Vaswani, N. Shazeer, N. Parmar, J. Uszkoreit, L. Jones, A. N. Gomez et al., *Attention is all you need*, 2017.

[13] A. Dosovitskiy, L. Beyer, A. Kolesnikov, D. Weissenborn, X. Zhai, T. Unterthiner et al., *An image is worth 16x16 words: Transformers for image recognition at scale*, 2021.

[14] J. Reiss, P. Schulze, J. Sesterhenn and V. Mehrmann, *The shifted proper orthogonal decomposition: A mode decomposition for multiple transport phenomena*, 2018.

[15] P. Krah, T. Engels, K. Schneider and J. Reiss, *Wavelet adaptive proper orthogonal decomposition for large scale flow data*, 2020.

[16] F. Bernard, A. Iollo and S. Riffaud, *Reduced-order model for the bgk equation based on pod and optimal transport*, .

[17] H. Eivazi, L. Guastoni, P. Schlatter, H. Azizpour and R. Vinuesa, *Recurrent neural networks and koopman-based frameworks for temporal predictions in a low-order model of turbulence*, 2021.

[18] J. Koellermeier, Y. Fan, M. Rominger and G. Samaey, "Moment models for kinetic equations." 2020.

[19] S. A. Schaaf, *Mechanics of Rarefied Gases*, *Handbuch der Physik* **3** (Jan., 1963) 591–624.

[20] G. Puppo, *Kinetic models of bgk type and their numerical integration*, 1902.08311.

[21] G. A. Sod, *Review. A Survey of Several Finite Difference Methods for Systems of Nonlinear Hyperbolic Conservation Laws*, *Journal of Computational Physics* **27** (Apr., 1978) 1–31.

[22] J. Reiss, *Skript zu cfd 1*, 1603.07285.

[23] S. L. Brunton and J. N. Kutz, *Data driven science and engineering.* 2019.

[24] Y. LeCun, L. Bottou, G. Orr and K. Müller, *Efficient backprop*, in *Neural Networks: Tricks of the Trade*, 2012.

[25] K. He, X. Zhang, S. Ren and J. Sun, *Delving deep into rectifiers: Surpassing human-level performance on imagenet classification*, 1502.01852.

[26] D. P. Kingma and J. Ba, *Adam: A method for stochastic optimization*, 1412.6980.

[27] V. Bushaev, "Stochastic gradient descent with momentum." https://towardsdatascience.com/stochastic-gradient-descent-with-momentum-a84097641a5d, Dec, 2017.

[28] T. Lane, *Transposed convolutions explained with ms excel!*, Nov, 2018.

[29] M. Divyanshu, *Transposed convolution demystified*, Mar, 2020.

[30] V. Dumoulin and F. Visin, *A guide to convolution arithmetic for deep learning*, 1603.07285.

[31] M. Ohlberger and S. Rave, *Reduced basis methods: Success, limitations and future challenges*, 1511.02021.

[32] F. Fan, J. Xiong, M. Li and G. Wang, *On interpretability of artificial neural networks: A survey*, 2021.

Acknowledgement

Hilfsmittel

.

Selbstständigkeitserklärung

Ich erkläre, dass ich die vorliegende Arbeit selbstständig und nur unter Verwendung der angegebenen Quellen und Hilfsmittel angefertigt habe.

Seitens des Verfassers bestehen keine Einwände, die vorliegende Bachelorarbeit für die öffentliche Benutzung im Universitätsarchiv zur Verfügung zu stellen.

Berlin, den 05. Juli 2021

Zachary Schellin